

**ANALYSIS OF BACKCALCULATED LAYER MODULI AND JOINT  
LOAD TRANSFER EFFICIENCY OF AIRFIELD RIGID  
PAVEMENT**

**By**

**APIDEJ SAKULNEYA**

**A Thesis submitted to the**

**School of Graduate Studies**

**Rutgers, the State University of New Jersey**

**In partial fulfillment of the requirements**

**for the degree of**

**Master of Science**

**Graduate Program in Civil and Environmental Engineering**

**Written under the direction of**

**Dr. Hao Wang**

**and approved by**

---

---

---

New Brunswick, New Jersey

October 2019

## **ABSTRACT OF THE THESIS**

### **ANALYSES OF BACKCALCULATED LAYER MODULI AND JOINT LOAD TRANSFER EFFICIENCY OF AIRFIELD RIGID PAVEMENT**

**by APIDEJ SAKULNEYA**

**Thesis Director: Dr. Hao Wang**

This study was aimed to analyze the sensitivity of the backcalculation of layer moduli and the joint load transfer efficiency of airfield rigid pavement.

The analyses were designed comprising two main methods. In the first part, the AREA method and the Graphical NUS-BACK solution were primary backcalculation methods. The input condition taken into the backcalculation was a field data of Heavy Weight Deflectometer (HWD) round-up project in the National Airport Pavement Test Facility (NAPT) in Atlantic City, NJ. Initially, the sensitivities of the deflection-based load transfer efficiency (LTE) were evaluated. Subsequently, the backcalculated layer moduli were compared with the lab test data. Those layer moduli were then applied as the input parameters for the overlay design using Federal Aviation Administration Rigid and Flexible Iterative Elastic Layered Design (FAARFIELD) to analyze their influences on the designed overlay thickness. In the second part, Finite Element Analysis Federal Aviation Administration (FEAFAA) was selected as a tool to investigate the stress-based joint load transfer efficiency under various input scenarios including variations in the temperature gradients of slab, landing gear configurations, traffic directions, and slab thicknesses.

The analyzed data from HWD test illustrated several findings. Firstly, the deflection-based LTE was found sensitive to several factors including the assessed position, the amount of load level, test direction, and the adjacent support of the evaluated slab. Secondly, the backcalculated elastic modulus obtained by the AREA method was closely matched to the lab test data whereas the NUS-BACK seemed to be overestimated. The backcalculated modulus of subgrade reaction from both methods was significantly greater than lab test data because they were assumed as a two-layered system in which the property of lower layer represented both the base and the subgrade layers. Thirdly, the overlay thickness calculated by different methods was clearly dissimilar to each other.

Moreover, the FEAFAA results demonstrated certain results. Firstly, the critical stress location for the slab loaded at the corner was more sensitive to different scenarios than those at the edge. Secondly, the combination of temperature gradient and the thickness of the slab predominantly influenced the critical tensile stress and the stress-based LTE of the slab. Thirdly, the value of ratio between the critical stress of 9-slab and the 1-slab pavement system ( $S_9/S_1$ ) varied differently to different scenarios. Therefore, the assumption in FAARFIELD that the 25 percent reduction on edge stress accounting for the load transfer may not be suitable under some circumstance.

## **ACKNOWLEDGMENTS**

I would like to express my deepest gratitude to my Thesis advisor, Dr. Hao Wang, who has supported me for the entire work. He always encouraged me and provided an appropriate direction for my research. It can be said that my research is fully complete owing to his endless help. Also, I would like to convey my regards to my thesis committee, Dr. Frank Moon, and Dr. Richard Ji for their encouragement and valuable comments.

Furthermore, my heart felt gratitude goes to my parents who, with their loves and kind consideration, provided just about everything for me while away having hardworking study. Without their superb benevolence my progressive life wouldn't come to this stage.

Last but not least, The Royal Thai Government by The Department of Highway is asked to accept my sincere gratitude in choosing and fully funding me for this study program in the USA, enabling me to live with ease and to gain such a great quality of advanced knowledge in the area. Without this great support my achievement as such would have been impossible.

## TABLE OF CONTENTS

<b>ABSTRACT OF THE THESIS.....</b>	<b>ii</b>
<b>ACKNOWLEDGMENTS.....</b>	<b>iv</b>
<b>TABLE OF CONTENTS.....</b>	<b>v</b>
<b>LIST OF FIGURES.....</b>	<b>ix</b>
<b>LIST OF TABLES.....</b>	<b>xiv</b>
<b>CHAPTER 1.....</b>	<b>1</b>
<b>INTRODUCTION</b>	
1.1    Problem of Statement.....	1
1.2    Objective and Study Scope.....	3
1.3    Organization of Thesis.....	3
<b>CHAPTER 2.....</b>	<b>5</b>
<b>LITERATURE REVIEW</b>	
2.1    Backcalculation of Rigid Pavement Modulus.....	6
2.1.1 Backcalculation Algorithms.....	7
2.1.2 Effect of Load Level .....	9
2.1.3 Effect of Bedrock Depth.....	10
2.1.4 Effect of Layer Thickness.....	11
2.1.5 Effect of Joint Type and Spacing .....	14
2.1.6 Effect of Temperature on Edge and Slab Curling.....	16
2.2    Joint Load Transfer Efficiency of Rigid Pavement.....	20
2.2.1 Definition of Load Transfer Efficiency.....	20

2.2.2	Variation in Load Transfer Efficiency.....	23
2.2.2	Effect of Slab Size on Pavement Performance and Load Transfer Efficiency.....	28
2.3	Airfield Rigid Pavement Response Analysis.....	30
2.3.1	Finite Element Modeling of Rigid Pavement.....	30
2.3.2	Cracking Failure in Airfield Rigid Pavement .....	32
2.4	FAA Rigid and Flexible Iterative Elastic Layered Design Software.....	38
<b>CHAPTER 3.....</b>		<b>42</b>
<b>FIELD DEFLECTION ANALYSIS AND MODULUS BACKCALCULATION</b>		
3.1	F/HWD Test Database from Round-up Project of FAA.....	42
3.1.1	Facility Layout and Pavement Structure of F/HWD Test.....	42
3.1.2	Test Plan of F/HWD Test.....	44
3.2	Deflection Analysis Using Field Data.....	47
3.2.1	Effect of Adjacent Support on Deflections .....	52
3.3	Backcalculation Analysis Methods.....	56
3.3.1	AREA Method for Rigid Pavements.....	57
3.3.2	Best-Fit Procedure and Graphical NUS-BACK Solution.....	60
3.3.3	Slab Size Correction Factors.....	62
3.4	Backcalculation Results.....	64
3.4.1	Comparison Between AREA Method and NUS-BACK Solution....	64
3.4.2	Comparison Between Back-calculated and Lab Test Results.....	66
3.4.3	Effect of Test Condition and Device.....	67
3.5	Overlay Design of FAARFIELD.....	78

3.5.1 Input Conditions.....	78
3.5.2 Overlay Design Results.....	80
<b>CHAPTER 4.....</b>	<b>85</b>
<b>JOINT LOAD TRANSFER ANALYSIS OF AIRFIELD RIGID PAVEMENT</b>	
4.1 Finite Element Modeling of Joint Load Transfer Efficiency.....	85
4.1.1 Finite Element Model Details .....	85
4.2 Mesh Sensitivity Analysis and Critical Stress Locations.....	92
4.2.1 Effect of Wheel Configuration.....	93
4.2.2 Critical Location for Tensile Stress at Bottom of Slab.....	93
4.2.3 Critical Location for Tensile Stress on Slab Surface.....	94
4.3 Critical Tensile Stress at Bottom of Slab and Stress-based LTE.....	96
4.3.1 Effect of Temperature Gradient and Slab Thickness on Critical Stress.....	97
4.3.2 Comparison of Critical Stresses Between Single Slab and Multiple Slabs.....	97
4.3.3 Stress-based Load Transfer Efficiency.....	98
4.4 Critical Tensile Stress on Slab Surface .....	105
4.4.1 Illustration of Stress Contour on Slab Surface.....	105
4.4.2 Effect of Temperature Gradient and Slab Thickness.....	106
4.4.3 Comparison of Critical Stresses Between Single Slab and Multiple Slabs.....	106
4.5 Comparison of Critical Tensile Stresses at Bottom and Surface of Slab.....	114

<b>CHAPTER 5.....</b>	<b>115</b>
<b>CONCLUSIONS AND RECOMMENDATIONS</b>	
5.1    Conclusions.....	115
5.2    Recommendations for Future Research.....	117
<b>REFERENCES.....</b>	<b>120</b>



## LIST OF FIGURES

FIGURE 2.1 Effect of Mistakenly Assumed Rigid Layer Depth on Backcalculated Deflection Under Loading Plate.....	12
FIGURE 2.2 Effect of Mistakenly Assumed Rigid Layer Depth on Backcalculated Deflection 72-inch Offset from Loading Plate.....	12
FIGURE 2.3 Effect of Mistakenly Assumed Rigid Layer Depth on Backcalculated Modulus of the Surface Layer.....	13
FIGURE 2.4 Effect of Mistakenly Assumed Rigid Layer Depth on Backcalculated Modulus of Base Layer.....	13
FIGURE 2.5 Effect of Slab Spacing on Deflection Basin in Doweled Condition.....	15
FIGURE 2.6 Effect of Slab Spacing on Deflection Basin in Undoweled Condition.....	15
FIGURE 2.7 Effect of Slab Spacing on Back-calculated Moduli.....	16
FIGURE 2.8 Daily Variation in Back-calculated k-value.....	17
FIGURE 2.9 Slab Curing Behaviors Along Joint due to Temperature Variation.....	18
FIGURE 2.10 Relationship Between Load and Deflection of Tested Slabs with Different Temperature Variations.....	19
FIGURE 2.11 Deflection vs Stress-based LTE for 12-inch Diameter Load Plate.....	22
FIGURE 2.12 Joint Load Transfer Efficiency.....	24
FIGURE 2.13 Relationship Between Air Temperature and Load Transfer Efficiency Along Transverse Joint.....	25

FIGURE 2.14 Relationship Between Air Temperature and Load Transfer Efficiency Along Longitudinal Joint.....	25
FIGURE 2.15 Cross-sectional of Tested Pavement.....	26
FIGURE 2.16 Deflection D0 at Joints and Corners.....	27
FIGURE 2.17 Comparison Between Ratio of High and Low values of LTD and Sum of Deflection.....	27
FIGURE 2.18 Average Pavement Condition Index of Investigated Slabs from 174 Airports in the United States and Japan.....	30
FIGURE 2.19 Sensitivity of Analyzed Elements of (a) Slab, (b) Foundation Layers to Response in FEAFAA.....	35
FIGURE 2.20 Normalized Sensitivity Indexes of Different Inputs vs Critical Responses for (a) Interior Loading and (b) Interior Loading with Temperature Loading.....	35
FIGURE 2.21 Normalized Sensitivity Indexes of Different Inputs vs Critical Responses for (a) Edge Loading and (b) Edge Loading with Temperature Loading.....	36
FIGURE 2.22 Normalized Sensitivity Indexes of Different Inputs vs Critical Responses for (a) Corner Loading and (b) Corner Loading with Temperature Loading.....	36
FIGURE 2.23 Effect of Temperature Gradient on Ratio of Top-to-bottom (a) Tensile and (b) Principal Stress for 2000 Scenarios.....	37
FIGURE 3.1 Facility Layout of Round-up Project.....	43
FIGURE 3.2 Tested Pavement Structure.....	44
FIGURE 3.3 Drop Locations.....	46
FIGURE 3.4 Loading and Reading Sensor Layout Diagram of FAA KUAB.....	46
FIGURE 3.5 Loading and Reading Sensor Layout Diagram of ERDC Dynatest... ..	47

FIGURE 3.6 Relationship Between Deflections and Load Levels on Different Load Locations.....	48
FIGURE 3.7 Relationship Between Deflection-based LTE and Load Levels.....	51
FIGURE 3.8 Actual Deflection at Location 2 Evaluated by FAA KUAB in Different Directions.....	54
FIGURE 3.9 Actual Deflection at Location 11 Evaluated by FAA KUAB in Different Directions.....	54
FIGURE 3.10 Actual Deflection at Location 2 Evaluated by ERDC DYNA in Different Directions.....	55
FIGURE 3.11 Actual Deflection at Location 2 Evaluated by ERDC DYNA in Different Directions.....	55
FIGURE 3.12 Sensor Layout for AREA36 Configuration.....	58
FIGURE 3.13 Graphical Chart for Radius of Relative Stiffness of Dense Liquid.....	63
FIGURE 3.14 Graphical Chart for Radius of Relative Stiffness of Elastic Solid.....	63
FIGURE 3.15 Graphical Solution for Deflector Factor.....	64
FIGURE 3.16 Relationship Between Modulus of Subgrade Reaction Calculated by AREA Method and NUS-BACK Solution with and Without Slab Size Correction Factor .....	76
FIGURE 3.17 Relationship Between Elastic Modulus of Concrete Slab Calculated by AREA Method and NUS-BACK Solution with and Without Slab Size Correction Factor .....	77
FIGURE 3.18 Backcalculated Modulus on Different Slabs.....	77
FIGURE 3.19 Relationship Between HMA Overlay Thickness and SCI.....	81

FIGURE 3.20 Relationship Between HMA Overlay Thickness and CDFU.....	82
FIGURE 3.21 Relationship Between PCC Overlay Thickness and SCI .....	82
FIGURE 3.22 Relationship Between PCC Overlay Thickness and CDFU.....	83
FIGURE 3.23 FAARFIELD Output When Minimum Thickness Has Been Reached.....	83
FIGURE 3.24 FAARFIELD output when design was terminated.....	84
FIGURE 4.1 Dimensions of Dual Wheel Landing Gear and Evaluated Critical Locations.	87
FIGURE 4.2 Dimensions of Dual Tandem Wheel Landing Gear and Evaluated Critical Locations.....	87
FIGURE 4.3 Landing Gear Layouts of Edge Loading in Single Slab Analysis.....	88
FIGURE 4.4 Landing Gear Layouts of Edge Loading in Multiple Slabs Analysis.....	88
FIGURE 4.5 Landing Gear Layouts of Corner Loading in Single Slab Analysis.....	89
FIGURE 4.6 Landing Gear Layouts of Corner Loading in Multiple Slabs Analysis.....	89
FIGURE 4.7 Airplane Selection Window Interface of FEAFAA.....	90
FIGURE 4.8 Pavement Structure Window Interface of FEAFAA.....	90
FIGURE 4.9 Joint Modeling Window Interface of FEAFAA.....	91
FIGURE 4.10 3D Mesh Generation Window Interface of FEAFAA.....	91
FIGURE 4.11 Relationship Between S9/S1 and Temperature Gradient.....	102
FIGURE 4.12 Relationship Between S9/S1 and Slab Thickness.....	102
FIGURE 4.13 Relationship of Stress-base LTE and Temperature Gradient of Slab.....	103
FIGURE 4.14 Relationship of Stress-base LTE and Slab Thickness.....	103
FIGURE 4.15 Relationship of Ratio of Free Edge and Summation of Loaded and Unloaded Stress vs Temperature Gradient of Slab.....	104

FIGURE 4.16 Relationship of Ratio of Free Edge and Summation of Loaded and Unloaded Stress vs Slab Thickness.....	104
FIGURE 4.17 Surface Stress Contour in Y-direction of Dual Wheel Moving in Y-direction Loaded at Corner of Single Slab.....	108
FIGURE 4.18 Surface Stress Contour in X-direction of Dual Tandem Wheel Moving in X-direction Loaded at Corner of Single Slab.....	109
FIGURE 4.19 Surface Stress Contour in Y-direction of Dual Wheel Moving in Y-direction Loaded at Corner of Multiple Slab.....	110
FIGURE 4.20 Surface Stress Contour in Y-direction of Dual Tandem Wheel Moving in X-direction Loaded at Corner of Multiple Slab .....	111
FIGURE 4.21 Relationship Between $S_9/S_1$ and slab thickness.....	113
FIGURE 4.22 Relationship Between $S_9/S_1$ and Temperature Gradient.....	113

## LIST OF TABLES

TABLE 2.1 Maximum Total Deflections, Transverse Stresses, and Load Transfer Index for Single Wheel Load.....	29
TABLE 2.2 Rigid Pavement Distresses Types for Computation of Structural Condition Index (SCI).....	40
TABLE 3.1 LTE and SD at different loads and locations.....	49
TABLE 3.2 Average and Standard Deviation of LTE and SD of Slab at Jointed Edge....	50
TABLE 3.3 Average and Standard Deviation of LTE and SD of Slab at Jointed Corner..	50
TABLE 3.4 Constant Coefficients for Deflection Coefficients.....	59
TABLE 3.5 Backcalculated result of the slab at location 2 without slab size correction by the AREA Method.....	69
TABLE 3.6 Backcalculated result of the slab at location 5 without slab size correction by the AREA Method.....	69
TABLE 3.7 Backcalculated result of the slab at location 8 without slab size correction by the AREA Method. ....	70
TABLE 3.8 Backcalculated result of the slab at location 11 without slab size correction by the AREA Method. ....	70
TABLE 3.9 Backcalculated result of the slab at location 2 with slab size correction by the AREA Method.....	71
TABLE 3.10 Backcalculated result of the slab at location 5 with slab size correction by the AREA Method.....	71

TABLE 3.11 Backcalculated result of the slab at location 8 with slab size correction by the AREA Method.....	72
TABLE 3.12 Backcalculated result of the slab at location 11 with slab size correction by the AREA Method. ....	72
TABLE 3.13 Backcalculated result of the slab at location 2 without slab size correction by the NUS-BACK.....	73
TABLE 3.14 Backcalculated result of the slab at location 5 without slab size correction by the NUS-BACK.....	73
TABLE 3.15 Backcalculated result of the slab at location 8 without slab size correction by the NUS-BACK.....	74
TABLE 3.16 Backcalculated result of the slab at location 11 without slab size correction by the NUS-BACK.....	74
TABLE 3.17 Backcalculated result of the slab at location 2 with slab size correction by the NUS-BACK.....	75
TABLE 3.18 Backcalculated result of the slab at location 5 with slab size correction by the NUS-BACK.....	75
TABLE 3.19 Backcalculated result of the slab at location 8 with slab size correction by the NUS-BACK.....	75
TABLE 3.20 Backcalculated result of the slab at location 11 with slab size correction by the NUS-BACK.....	76
TABLE 3.21 Comparison of Back-calculated Results and Lab Test Results.....	78
TABLE 3.22 Traffic Input Used in FAARFIELD.....	79

TABLE 3.23 Inputs of Layers Used in FAARFIELD.....	79
TABLE 4.1 Mesh Analysis for Tensile Stress at Bottom of Slab.....	95
TABLE 4.2 Mesh Analysis of Tensile Stress on Surface of Concrete Slab Along Diagonal Path.....	96
TABLE 4.3 Critical Tensile Stresses Below Slab from Edge Loading of Single Slab and 9-slab System .....	100
TABLE 4.4 Comparison of Stresses on Unloaded Slab and Loaded Slab on 9-slab System.....	101
TABLE 4.5 Critical Tensile Stresses on Surface of Slab from Corner Loading of Single Slab and 9-Slab System.....	112
TABLE 4.6 Critical Tensile Stress at Bottom and Surface of Slab.....	114



## **CHAPTER 1**

### **INTRODUCTION**

#### **1.1 Problem of Statement**

Transportation infrastructure has literally considered as one of the crucial foundations of national development in every country. It has contributed to the growth in economic and social benefits in many terms. Well maintained roadways reduce the vehicle operating costs, accident rates, and benefit people in rural communities (Burningham & Stankevich, 2005). Therefore, the operations to maintain and prolong roadways should be prioritized.

One way to extend terms of pavement life is overlaying paving materials on top of existing pavement. Proper overlay thickness design could maximize operational pavement life and lower the road administration costs and road user costs (Mikolaj, Remek, & Macula, 2017). Therefore, the overlay design procedure requires the accurate input parameters, which could be achieved by an evaluation of existing pavement condition and a well-understanding in the sensitivity of the pavement design parameters.

Theoretically, the Falling Weight Deflectometer (FWD) has been long used to measure the surface deflections of the pavement subject to the impulse load generated by the FWD machine by which the measured deflections were back-calculated to obtain the modulus of pavement layers (Stubstad, Jiang, & Lukanen, 2006). These back-calculated parameters were the input parameters required for the design of the overlay. Since a non-

destructive evaluation of the structural capacity and back-calculated modulus of the existing pavement has been extensively used, the variations resulted from various factors such as the test machines, tested directions, tested locations, and temperature gradients should be carefully considered as they might affect the back-calculated results. Therefore, the sensitivity of this evaluation method should be taken into account because the imprecision of the back-calculated pavement properties could mislead the overlay life.

Apart from the back-calculated moduli, the joint load transfer has also been one of the input parameters required for overlay design. It could be computed in two different ways either by the deflection ratio or the stress ratio between the loaded and unloaded slabs. The Federal Aviation Administration (FAA) specified a constant value of 25 percent reduction on free edge stress, which accounted for the load transfer between slabs in the airfield pavement design software (FAARFIELD). However, the response of the airfield rigid pavement was highly complex since it was influenced by various factors. For instance, Armaghani et al. (1987) found that temperature variation caused the slab to curl in different directions which introduced additional stresses to the concrete slab. Therefore, the curing in the concrete slab caused noticeable changes in the mechanical stress of the slab. Also, the load transfer capability of joint might not be consistent at different conditions. Thus, the consequences of using a constant value as a coded input in the airfield rigid pavement design were needed to be investigated.

## **1.2 Objective and Study Scope**

This research mainly focused on two issues. Firstly, the backcalculation of the airfield rigid pavement was evaluated. Secondly, the rigid slab responses including the joint load transfer under different aircraft loading conditions were investigated.

Numerous related literature review on the variations of the back-calculated elastic moduli of the airfield rigid pavement, and the definition and sensitivities of joint load transfer were provided.

In the first part, the Heavy Weight Deflectometer data from two devices-FAA KUAB and ERDC Dynatest- tested at the round-up project in the National Airport Pavement Test Facility in Atlantic City, New Jersey was selected as the field data used in the analysis of deflection and backcalculated moduli. Consequently, the backcalculated moduli were employed in the overlay design of rigid pavement handled by FAARFIELD.

The second part concentrated primarily on the analysis of stress responses owing to different types of aircraft landing gears. In addition, the above mentioned the comparisons between the critical stress on the single slab and multiple slab systems were explored at different scenarios using finite element analysis.

## **1.3 Organization of Thesis**

There were five chapters in this thesis as follows;

### **Chapter 1**

A brief description of background and scope of this thesis was provided.

## **Chapter 2**

A summarized literature review related on back-calculation methods and their variations in the rigid pavement were presented. Additionally, the definition and the influencing factors of the load transfer efficiency in jointed plain concrete pavement were interpreted. Furthermore, reviews on the airfield rigid pavement response analysis including the finite element analysis tool, the cracking failure mode, and the overlay design software (FAARFIELD) were demonstrated.

## **Chapter 3**

A sensitivity of non-destructive evaluation of the rigid pavement was evaluated basing on the HWD tested data provided by the FAA. Comparisons between the two backcalculation methods and the lab test data were provided. Consequently, those backcalculated layer moduli were used for the overlay design using FAARFIELD to validate their effects on the designed overlay thickness.

## **Chapter 4**

Comprehensive analysis on joint load transfer of airfield rigid pavement responses using different inputs of landing gear configuration, slab temperature gradient, and slab thickness were employed by the FEAFAA program. The pavement responses including the critical tensile stress at the bottom and on the surface of slab, the ratio between the critical tensile stress of multiple slabs and the critical tensile stress on the free edge of a single slab, and the stress-based load transfer efficiency were illustrated and discussed.

## **Chapter 5**

Conclusions on analysis findings and recommendations for further research were revealed and discussed.

## **CHAPTER 2**

### **LITERATURE REVIEW**

There were two significant components in this research; Analysis of backcalculated moduli and joint load transfer efficiency of airfield rigid pavement. The first part was mainly related to the utilization of the back-calculation method in order to calculate the elastic modulus of the rigid pavement while the second one was conducted to extensively investigate the sensitivities of joint load transfer of the airfield rigid pavement using the finite element analysis.

Even though the back-calculation methods have been used to back-calculate elastic modulus of pavement from FWD (Falling Weight Deflectometer)/HWD (Heavy Weight Deflectometer)-test for decades, there were some limitations in these methods. This review interpreted the details related to the non-destructive deflection tests. It also illustrated the affecting factors of back-calculated results, including the effect of temperature on edge and corner deflections, the effect of temperature on load transfer efficiency, and the sum of deflections. Also, the definition and variations of load transfer efficiency were described.

In the last part, the review on airfield rigid pavement response analysis and design method were provided including two FAA's software-FEAFAA and FAARFIELD.

## 2.1 Backcalculation of Rigid Pavement

According to Burningham and Stantevich (2005), a demand for pavement maintenance around the world was relatively high. Unfortunately, many countries have spent less than half of the appropriate spending on their roadways since it has been very challenging to deal with their constraint budget available.

Recently, pavement overlays on the top layer of the existing pavement structure has been an alternative way of extending pavement life. Nevertheless, the evaluation of the existing pavement's structural capacity was inevitably required for a proper overlay design.

Currently, nondestructive deflection test has been one of the most convenient tools to evaluate pavement structural capacity. There was a wide range of nondestructive deflection testing devices available such as. Falling Weight Deflectometer (FWD), Automatic distress survey, Traffic speed deflectometer, GPR, etc.

As widely recognized, the benefits of using FWD consisted of the preservation of integrity in existing layers. The outcomes from the non-destructive testing (NDT) could be applied in many aspects as follows (Thottempudi, 2010);

- The back-calculation of moduli of subgrade reaction and elastic moduli of both flexible and rigid pavements.
- The estimation of load transfer capability of the transverse and longitudinal joints in rigid pavements.
- The detection of the existing of air voids below the slab.
- The design of overlay thickness for pavement rehabilitation.

### 2.1.1 Backcalculation Algorithms

Various types of back-calculation methods were given including AREA, NUS-BACK, Best-Fit, ILLIBACK, BAKFAA, etc.. Their algorithms distinguished them from each other. The back-calculated results obtained from each method were often different because the pavement models, solution search procedures, and deflection matching criteria were dissimilar in each algorithm (Fwa & Setiadji, 2006). According to Ellis (2008), some available backcalculation methods and software could be described as follows.

AREA method has been one of the methods that develop to deal with the deflection basin obtained from FWD testing. It applied Westergaard's solution of the loading plate resting on dense liquid foundation for the analysis. AREA parameter was the normalized area of deflection which denied the influence from the load magnitude and it was a main parameter used in the backcalculation (Ioannides, 1990).

NUS-BACK was one of the methods that existed in both a computer program and a graphical solution. The closed-form solution was used, and the subgrade was considered either the dense liquid or elastic solid foundation. A computer version called NUS-BACK3, the method for solution in this program was the analysis of a three-layer system including the elastic solid subgrade model. In a graphical version, a rigid pavement was considered as a two-layer system. It simply required only two or more deflections to calculate the stiffness of the rigid pavement and subgrade.

Like the AREA method, Best-Fit method was also one of the methods that employed Westergaard's solution in the analysis for the interior loading (Khazanovich, McPeak, & Tayabji, 2000). However, the Best-Fit offered a well match between measured

and calculated deflection basins because its procedure matched deflections specifically point by point, which was similar to the NUS-BACK.

ILLIBACK was the earliest closed-form backcalculation method for the two-layer system rigid pavements developed by Ioannides and his team in 1989 (Huang, 1993). ILLIBACK was firstly provided in a DOS based computer software. A crucial point in ILLIBACK was that it concerned on the relationship between the radius of relative stiffness to a ratio of measured deflections. Once the radius of relative was determined, the layer moduli were then calculated.

BAKFAA was a software developed by the Federal Aviation Administration. Its purpose was provided for the backcalculation of layer moduli in airfield pavement. The BAKFAA was an iteration-based backcalculation program that operated by LEAF software. The computation in LEAF was done by iterating the minimum error between the generated deflections and actual deflections. Those generated deflections in the iteration process were given by the adjusted layer moduli in the pavement structure. Consequently, the modified moduli were the outputs in the backcalculation of BAKFAA.

Guo and Marsey (2012) suggested that the back-calculated elastic modulus of concrete slab was not equal to the elastic modulus obtained from the laboratory tests. They explained that the back-calculated modulus was not directly present the material property since it also included the structural model and the boundary conditions employed in the back-calculation. Therefore, the lab-tested results were not so good indicators that can be compared with the back-calculated values.

Besides, there were various methods in back-calculation of rigid pavement layer moduli. These methods were different from each other based on their theories, and



boundary conditions. For example, the AREA method considered the entire deflection basins in its calculation, whereas the based-fit procedure matched deflection by each point in their estimation. Therefore, the outcomes attained from different methods might be divergent.

Fwa and Setiadji (2006) studied the comparison of four back-calculation algorithms including two versions of ILLIBACK, NUSBACK, and LTPP best-fit method. they found numerous factors effecting the results of the algorithms mentioned. One element was the sensor configurations-the number of sensors and the locations of selected sensors. When the actual pavement system did not entirely behave as a perfect elastic system, the matching of computed and measured deflection basins did not provide the best outcomes in the back-calculation analysis.

The results showed that the critical difference between the ILLIBACK algorithms and the LTPP best-fit method was their deflection-matching requirement. The best-fit method illustrated a lower degree of errors than ILLIBACK since it had a less stringent point in matching of deflections.

### **2.1.2 Effect of Load Level**

Khazanovich et al. (2000) proved that the load magnitude did not influence the back-calculated results provided the load level was sufficient. Moreover, the study conducted by Kim and Park (2002) showed that the linear behavior of subgrade soils was terminated when the load level of greater than 12 kips was applied.

Chou and Lytton (1991) suggested that the variations in load level did not significantly affect the average deflection matching error. However, they also found that

the backcalculated layer modulus was differently affected by the load levels. The influences of load levels on the backcalculated modulus also depended on the individual pavement structure and the material type of the layer. For instance, the backcalculated modulus of the granular base increased as the load levels increased, while the backcalculated modulus of the sandy clay decreased as the load levels rose up.

### **2.1.3 Effect of Bedrock Depth**

Chou and Lytton (1991), in a comparative study on the accuracy and consistency of back-calculation results found that some input parameters required by the back-calculation algorithms including Poisson's ratios, layer thickness, load configuration, error tolerance, the maximum number of iterations, and the bedrock depth significantly affected the back-calculated results. They mentioned that when the assumption of the bedrock depth markedly deviated from the actual value, significant errors in matching the computed and actual deflections usually appeared. Moreover, they found that the error occurred in a thin slab (1-in.) was considerably higher than that shown in the thicker slab (5-in) since, the thinner layer was more sensitive to the input parameter.

Briggs and Nazarian (1989) studied the effects of unknown rigid subgrade layer on the back-calculation results. They found that the error input of rigid layer depth could negatively affect the value of the back-calculated pavement moduli when the assumed bedrock depth was equal to or more than the double amount of the actual bedrock depth.

The effects of the mistakenly assumed rigid layer depths on the back-calculation under the loading plate and at 72-inch offset from the loading plate were illustrated in Figure 2.1 and Figure 2.2 respectively. When the ratio of the actual depth and assumed

depth was lower than 0.5, the back-calculated deflection was likely to deviate from the actual deflection. Moreover, when the rigid depth ratio was lower than 0.5, the back-calculated moduli of the surface layer and base layer could be nearly overestimated by 300 percent and underestimated by 500 percent as depicted in Figure 2.3 and Figure 2.4 respectively.

#### **2.1.4 Effect of Layer Thickness**

Another study conducted by Maina et al. (1998) mentioned about the effect of the error input of layer thickness on the back-calculated layer moduli. It was concluded that the input slab thickness lower than the actual value would have a more significant effect on the back-calculated moduli than the input slab thickness higher than the actual value.

However, the error input of base layer thickness had less significant effects on the back-calculated moduli than those of slab thickness. Additionally, Maina claimed that the back-calculated moduli on the base layer were relatively insignificant by the errors in layer thickness.

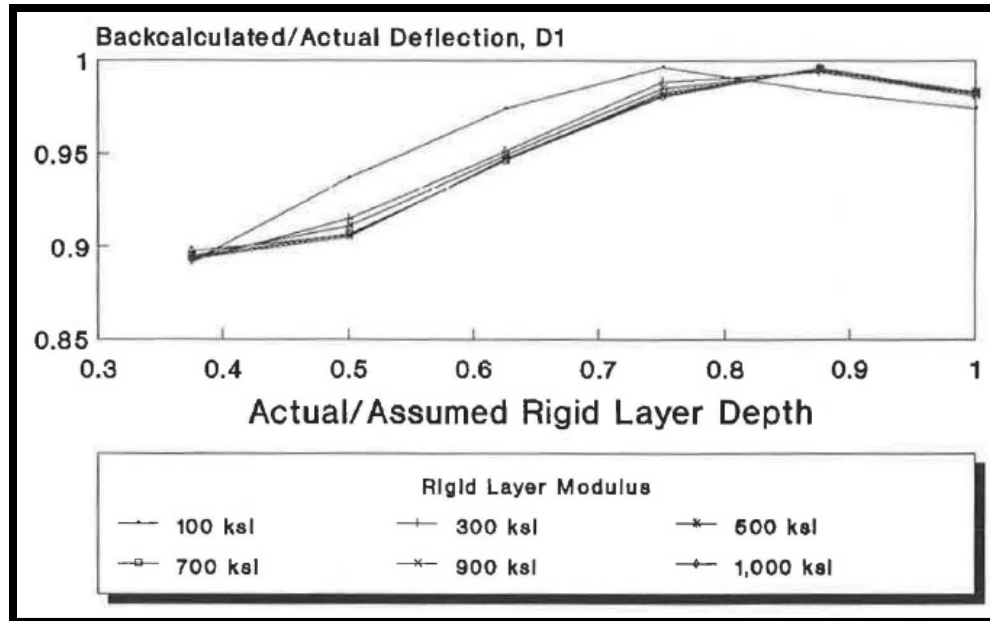


**FIGURE 2.1** Effect of mistakenly assumed rigid layer depths on back-calculated deflection under loading plate (Briggs & Nazarian, 1989).

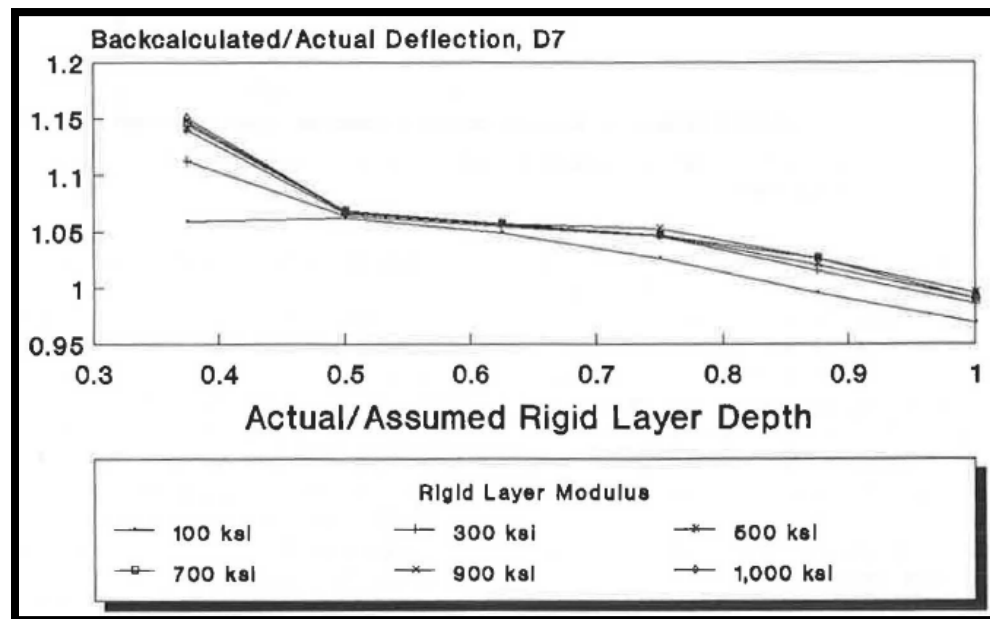


**FIGURE 2.2** Effect of mistakenly assumed rigid layer depths on back-calculated deflection 72-inch offset from loading plate (Briggs & Nazarian, 1989).

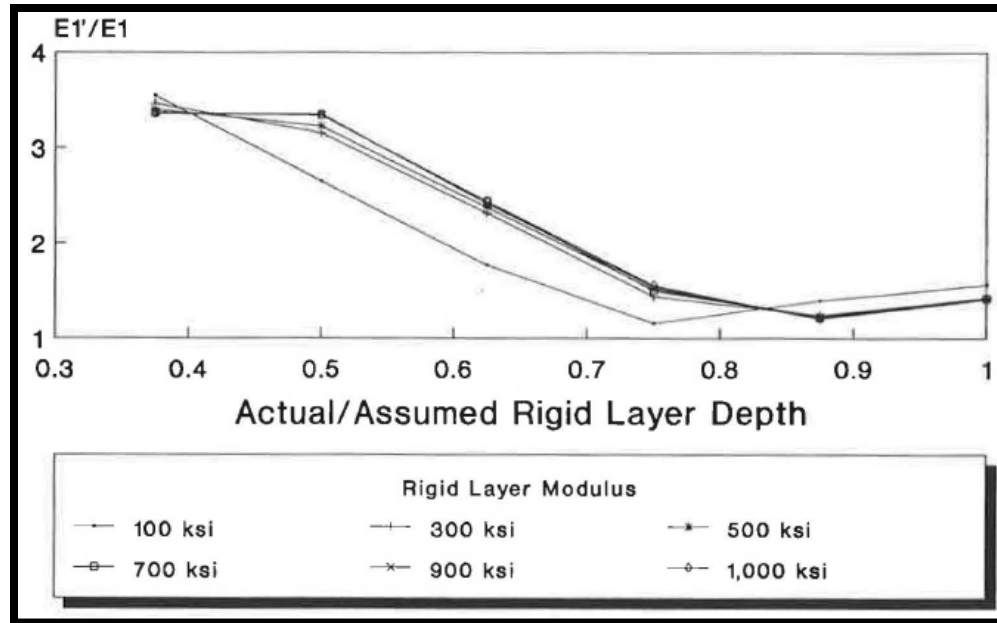


**FIGURE 2.3** Effect of mistakenly assumed rigid layer depths on the back-calculated modulus of surface layer (Briggs & Nazarian, 1989).

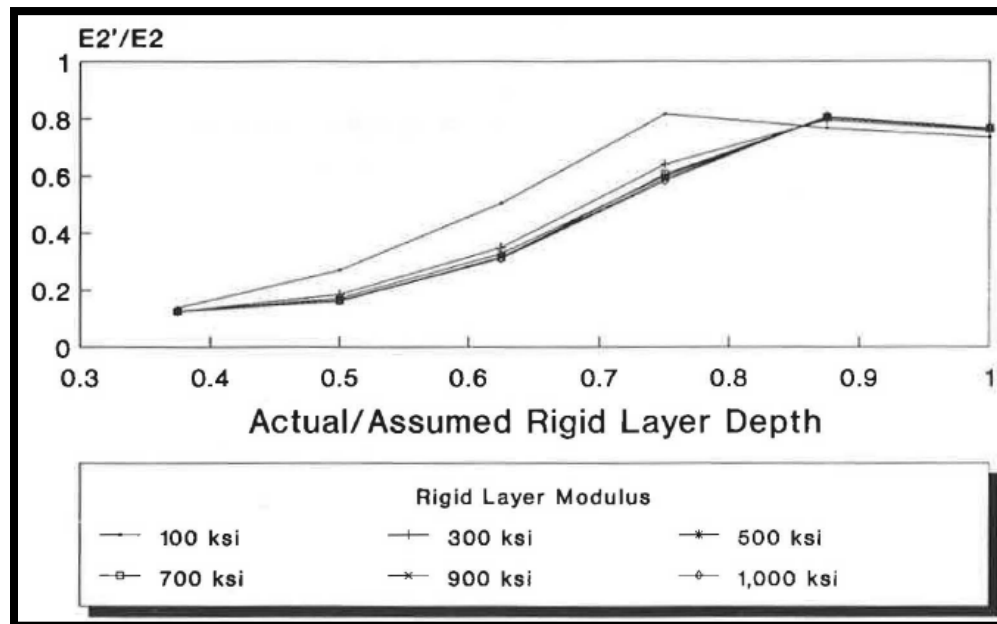


**FIGURE 2.4** Effect of mistakenly assumed rigid layer depths on the back-calculated modulus of base layer (Briggs & Nazarian, 1989).

### 2.1.5 Effect of Joint Type and Spacing

Shoukry et al. (1999) evaluated the performance of back-calculation in the rigid pavement using a finite element model and found that not only the spacing between transverse joints that affected the back-calculated results but also the type of joint that played a vital role in the back-calculated outcomes. In their study, the surface deflection basins measured by the FWD machine on doweled and undoweled slabs were compared with the deflection basins generated by finite element model. The results indicated that the slab spacing did not influence the surface deflections when the slabs were sufficiently doweled, as shown in Figure 2.5. The main reason was that the doweled bars were able to adequately transfer the stresses to the adjacent slabs.

However, when the concrete slabs were undoweled, the slab spacing turned out to be one of the significant factors that affected the FWD deflection basins, as shown in Figure 2.6. Also, the maximum deflection at the center of the slab with the undoweled condition was considerably lower than the measured deflection in the doweled condition. Moreover, there was less continuity of deflection from the center of the slab to the transverse joint in the undoweled slabs.

The difference between the first and the last sensor deflections increased when the slab length increased (Figure 2.6). Consequently, the back-calculated moduli obtained from different slab lengths of the un-doweled slab were significantly different from each other, as illustrated in Figure 2.7.

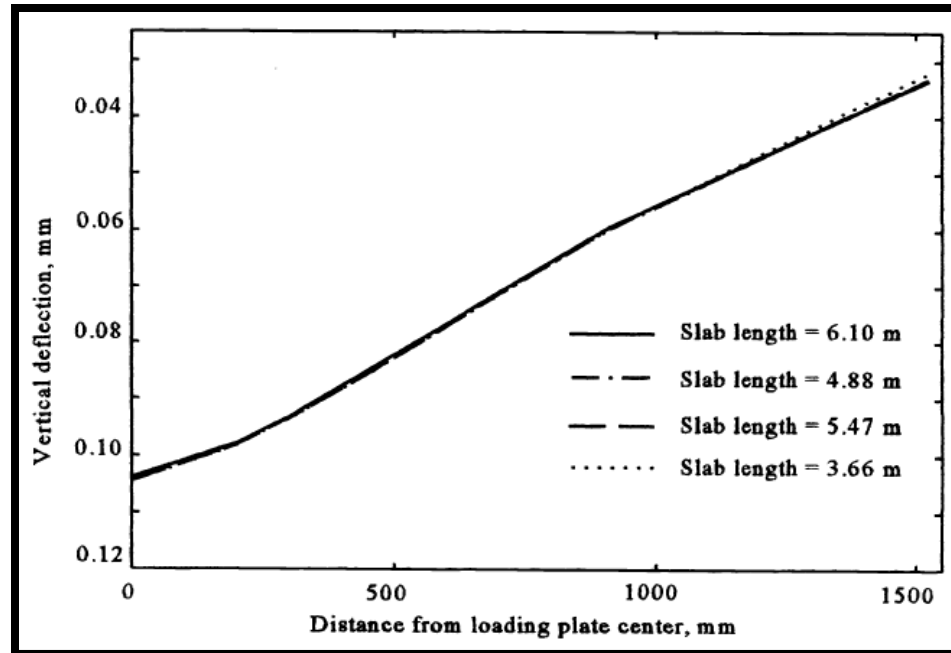


FIGURE 2.5 Effect of slab spacing on deflection basin in doweled condition (Shoukry, William, & Martinelli, 1999).

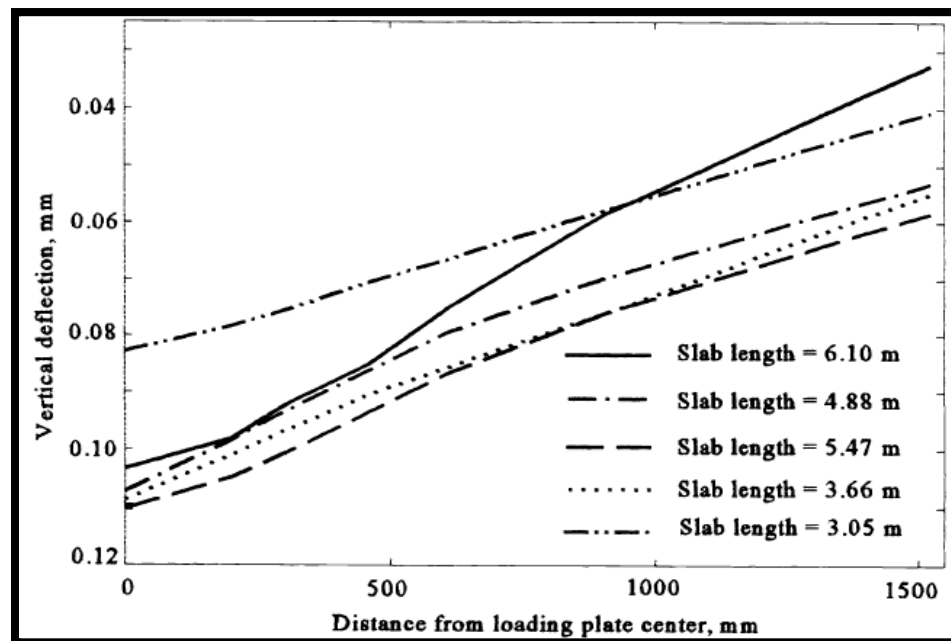
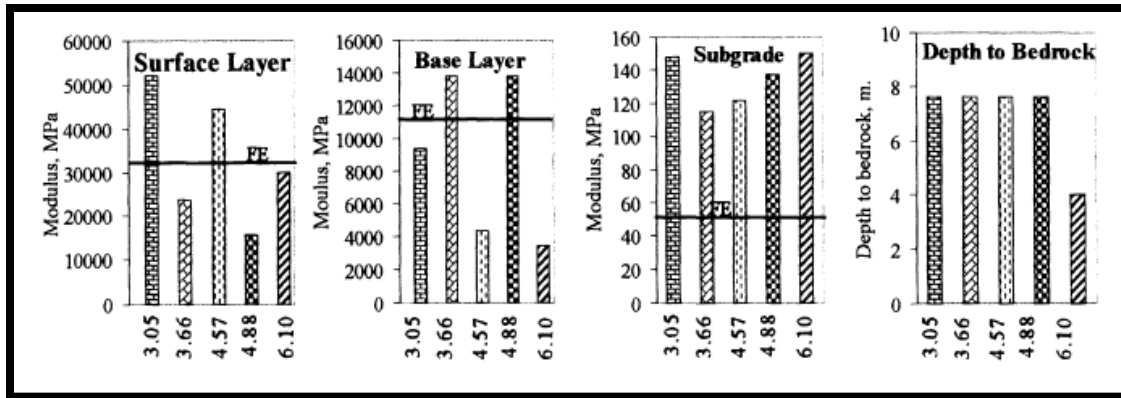


FIGURE 2.6 Effect of slab spacing on deflection basin in undoweled condition (Shoukry et al., 1999).



**FIGURE 2.7 Effect of slab spacing on back-calculated moduli (Shoukry et al., 1999).**

### 2.1.6 Effect of Temperature and Slab Curling

Khazanovich et al. (2000) mentioned that curling behaviors caused variation in back-calculated elastic modulus during the FWD testing instead of the differences caused by material properties alone. They claimed that the stiffness of subgrade in the edge of the section tested at the end of the summer season was generally weaker than the results tested at the end of the winter season. Furthermore, they found a high variation of the subgrade stiffness and the elastic modulus of the concrete slab over the day. The highest modulus of subgrade measured in the morning was three times higher than the lowest value measured in the afternoon on the same day, as shown in Figure 2.8. However, they mentioned that there was adequate friction at the center area of the slab while the slab was curling. Thus, the concrete slab might be in full contact with the base at the center area of the slab.



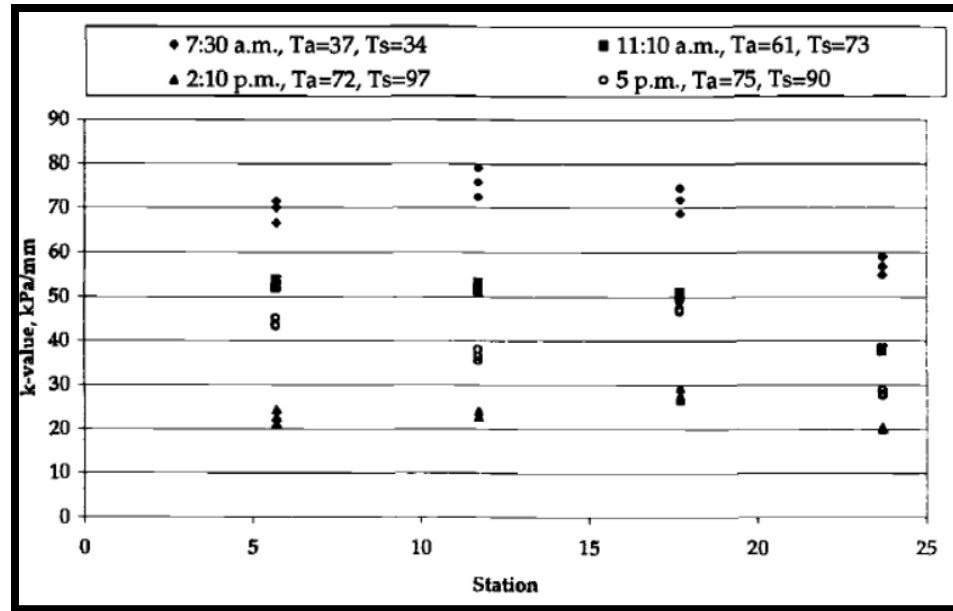


**FIGURE 2.8 Daily variation in back-calculated k-value (Khazanovich et al., 2000).**

Moreover, the temperature variation might introduce the horizontal and vertical displacements in the concrete slab since the differences in temperature caused curling behavior in the slab (Armaghani, Larsen, & Smith, 1987). The positive and negative temperature gradients caused a slab to curl in different ways, as shown in Figure 2.9. Therefore, shear and moment resistance along the edge and corner of the concrete slab were affected by the differences in temperature. The variation in temperature also affected the stiffness of subgrade because the contact areas between the slab and the subgrade were disturbed when the curling occurred.

As illustrated in Figure 2.10, the corner deflection was noticeably high when the surface temperature of the pavement was much lower than the temperature beneath the slab. This high deflection was owing to loss of subgrade support caused by the upward curling from temperature variation. On a contrary point of view, when a slab was curling downward by the positive temperature variation, the stiffness of the slab (a ratio between

the load and deflection from line 4) increased due to the gaining in a contact area of subgrade support.

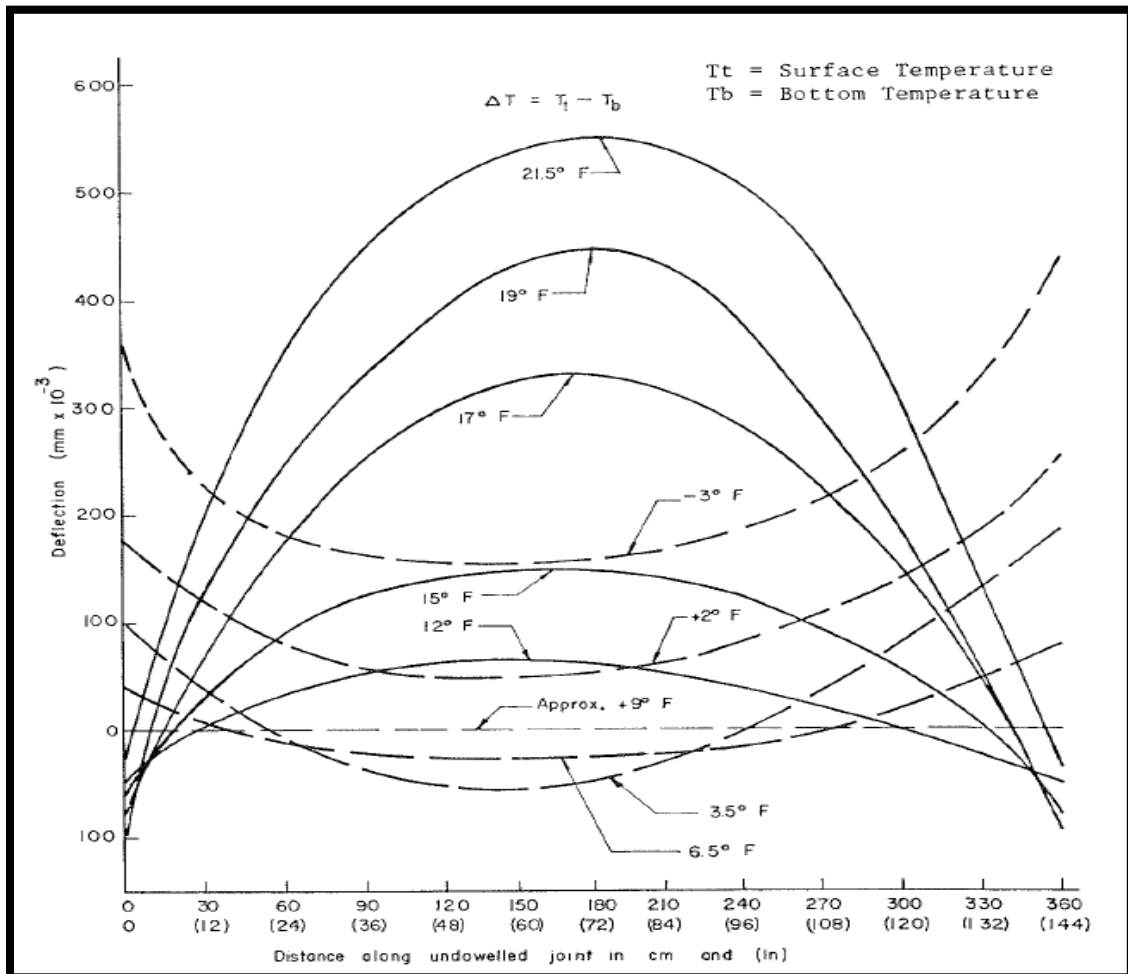


**FIGURE 2.9 Slab curling behaviors along a joint due to temperature variation (Armaghani et al., 1987).**

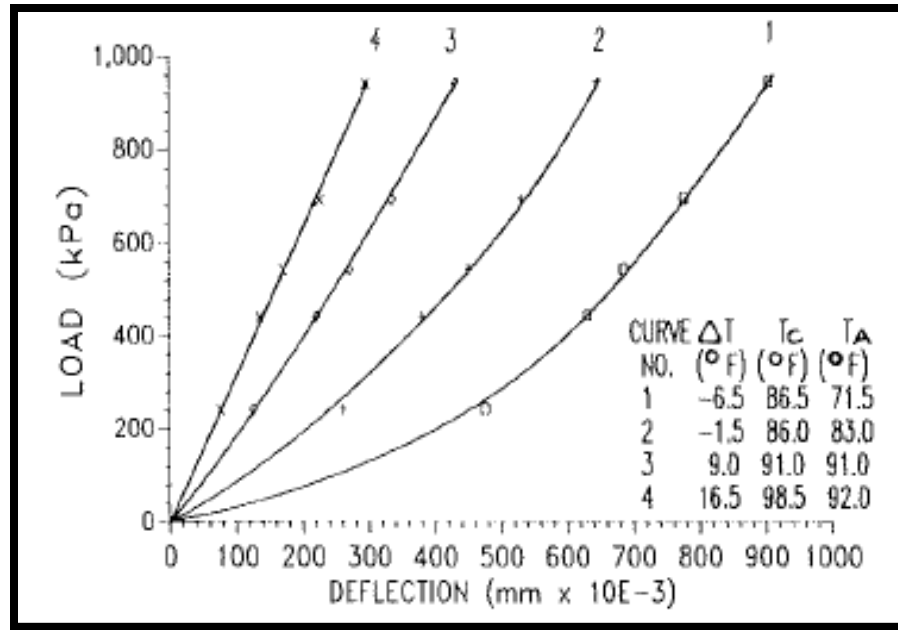


**FIGURE 2.10 Relationship between load and corner deflections of tested slabs with different temperature variations (Armaghani et al., 1987).**

Another comprehensive study conducted by Zhao et al. (2018), focused on the deflection of the slab caused by the temperature differences at the top and bottom of the concrete slab. The positive temperature gradient was assigned when the temperature on the top was higher than the temperature at the bottom. For the negative temperature gradient, it was vice versa from the positive temperature gradient. They found that the variation of temperature marginally disturbed the deflection basin at the center of the slab.

However, when the positive temperature gradient exceeded a critical value, the center slab deflection also increased. The main reason was the fluctuation of the deflections at the joint and the corner of the slab during the day. The maximum deflection at the transverse joint and the corner of a slab were profoundly influenced by the negative temperature gradients because the contact area between the slab and the base was reduced by the curling-up behavior introduced by the negative temperature gradient.

## 2.2 Load Transfer Efficiency in Rigid Pavement

American Association of State Highway Transportation Officials, AASHTO (1993) described joint performance of the concrete slab in terms of load transfer efficiency (LTE). However, there have been several called terms of load transfer efficiency. In some studies, load transfer efficiency (LTE) was also called as the joint load transfer equivalency (JTE), or load transfer capability (LTD).

### 2.2.1 Definition of Load Transfer Efficiency

Generally, when traffic loads were applied to one slab in multiple slab pavements, some portions of the loads were transferred to the adjacent unloaded slabs. Therefore, the deflections and stresses along the joints in multiple slab pavements were noticeably lower than those in the single slab pavement or a slab with a free edge. The lower values in the deflections and stresses could be referred to the influence of load transfer efficiency (LTE).

According to Khazanovich and Gotlif (2003), LTE could be determined based on either deflection or stress. For deflection-based analysis, LTE has been defined as the ratio between the deflection at the joint of the unloaded slab and the maximum deflection at the joint of the loaded slab as shown in Equation 2.1. Whereas for stress-based analysis, it has been defined as the fraction between the matching stress at the joint of the unloaded slab and the maximum stress at the joint of the loaded slab, as shown in Equation 2.2.

$$LTE = \frac{d_{unloaded}}{d_{loaded}} * 100\% \quad \dots\dots\dots \text{Eq. 2.1}$$

$$LTE = \frac{\sigma_{unloaded}}{\sigma_{loaded}} * 100\% \quad \dots\dots\dots \text{Eq. 2.2}$$

The Federal of Aviation Administration abbreviated FAA (Federal Aviation Administration, 2016) defined the LTE as the ratio of the edge stress of the unloaded slab and the maximum flexural stress on the free edge condition of the loaded slab. Moreover, according to the FAA's advisory circular (No.150/5320-6F), the efficiency of load transfer through the joint was sufficient to reduce the free edge flexural stress in concrete slab by 25 percent and coded in FAA's pavement design program (FAARFIELD). Sequentially, Guo (2003) found that for a concrete slab with no curling and warping conditions, the free edge bending stress of the loaded slab was equal to the summation of the loaded and unloaded stresses on the joint of JPCP. Therefore, regarding the FAA's advisory circular and the finding of Guo (2003), LTE could be defined as illustrated in equation 2.3.

$$LTE = \frac{\sigma_{unloaded}}{\sigma_{free\ edge}} = \frac{\sigma_{unloaded}}{\sigma_{loaded} + \sigma_{unloaded}} * 100\% \dots\dots\dots \text{Eq. 2.3}$$

Furthermore, FAA (2011) mentioned that the relationship between LTE determined from deflections and stresses was nonlinear implying that the conversion from deflection-based LTE to stress-based LTE might be required to investigate the influence of load transfer on the pavement structure. From the conversion chart in Figure 2.11, the stress-based LTE of 25 percent was equal to the deflection-based LTE ranging from 70 to 90 percent suggesting that the variations relied on the radius of relative stiffness.

Previously in their study, Hammons et al. (1995) concluded that the rigidly assigned value of 25 percent load transfer might be inappropriate. They found that in winter, LTE value was random and should not be defined as a single constant value. They also

mentioned that LTE was significantly affected by such various variables as slab thickness, joint spacing, temperature, the stiffness of subgrade, etc.

With regard to their experiments based on different types of joints and conditions, it was found that the probabilities of the mean values of LTE less than 25 percent were ranged from 60 to 100 percent literally indicating that the overestimation of LTE in rigid pavement design would cause a significant decrease in the pavement life due to the insufficient design thickness from the FAARFIELD.

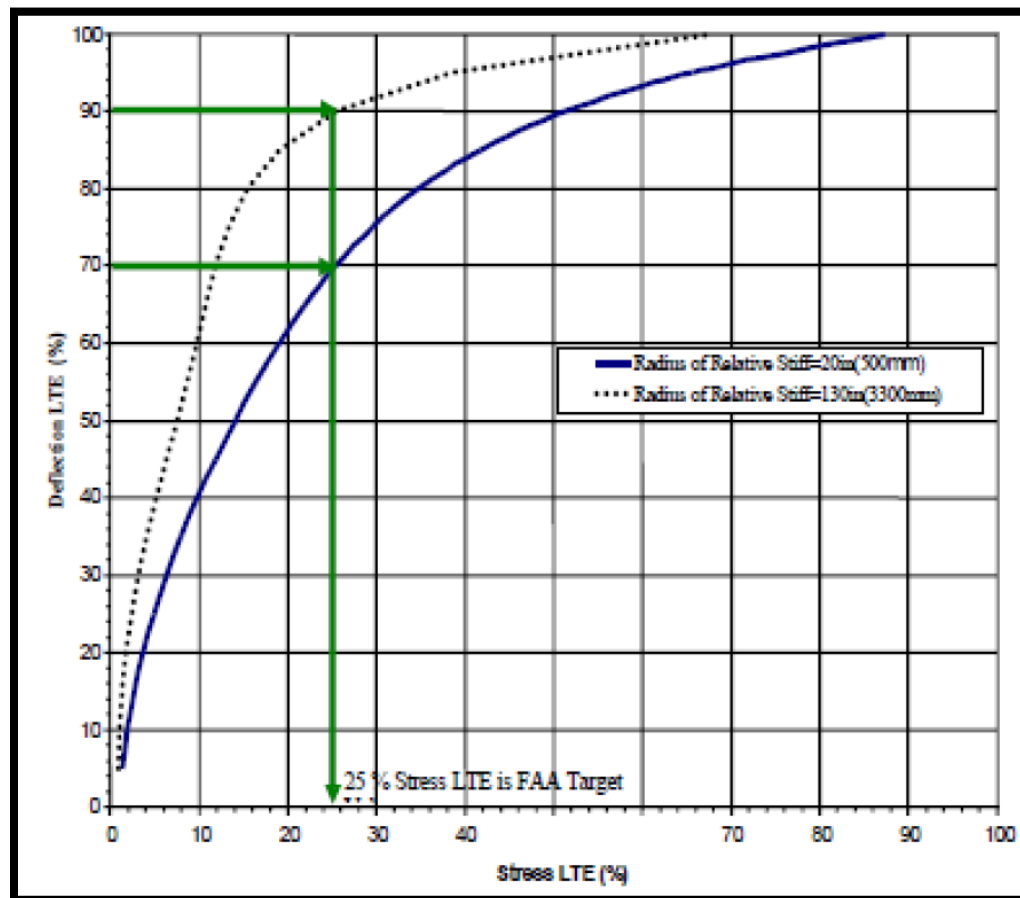


**FIGURE 2.11 Deflection vs stress-based LTE for 12-inch diameter load plate (Federal Aviation Administration, 2011).**

### 2.2.2 Variation in Load Transfer Efficiency

Foxworthy and Darter (1986) convinced in their study that the direction and location effects on the LTE evaluation should be concerned. They found that the LTE on the approach slab has deviated from the LTE on the leave slab. Also, the differences between the LTE evaluated on the approach slab and the leave slab along the longitudinal joint was considerably higher than the deviations along with the transverse joint due to the loading history because the aircraft gears frequently traveled on one slab side parallel to the longitudinal joint as shown in Figure 2.12. They explained that the deviations between the approach slab and the leave slab along the transverse joint were small because the traffic usually took place in bi-directional line. Therefore, the loading history on the approach slab and leave slab along the transverse joint were almost identical to each other. Furthermore, they found the remarkable reduction of the LTE on the corner of slab and summarized that it could be caused by either the loss of sub-base support at the corner or the scarcity of dowel bars near the corner.

Additionally, they mentioned that the LTE in the rigid pavement was profoundly influenced by the combination of curling effects and expansion and contraction effects caused by the changes in temperature. Figures 2.13 and 2.14 showed that the load transfer efficiency would actually increase as the air temperature rose up. The relationship between the LTE and the air temperature could be described by a reduction in joint opening caused by the contributions of the aggregate interlock and the deflection resistance along the concrete surface at the joint.

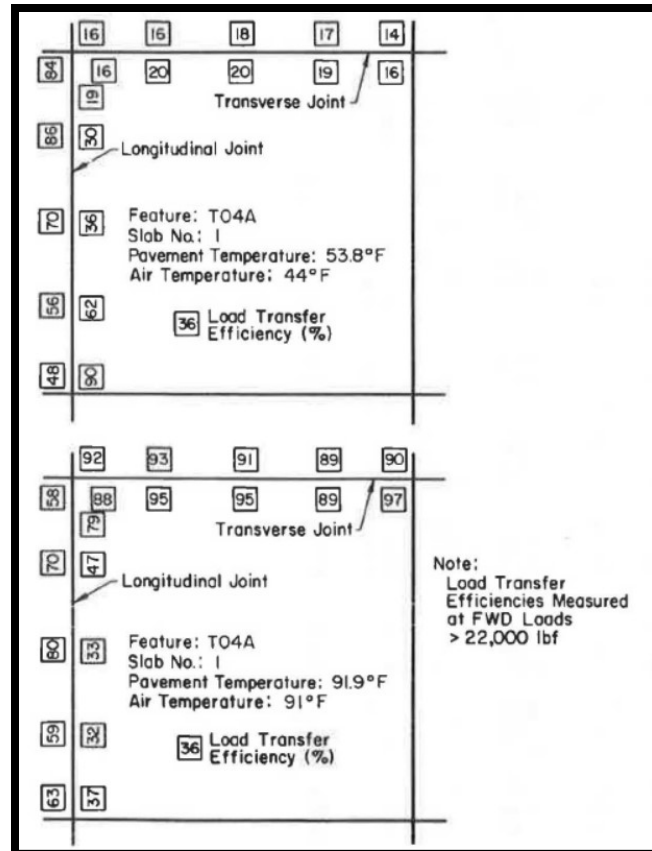


FIGURE 2.12 Joint load transfer efficiency (Foxworthy & Darter, 1986).

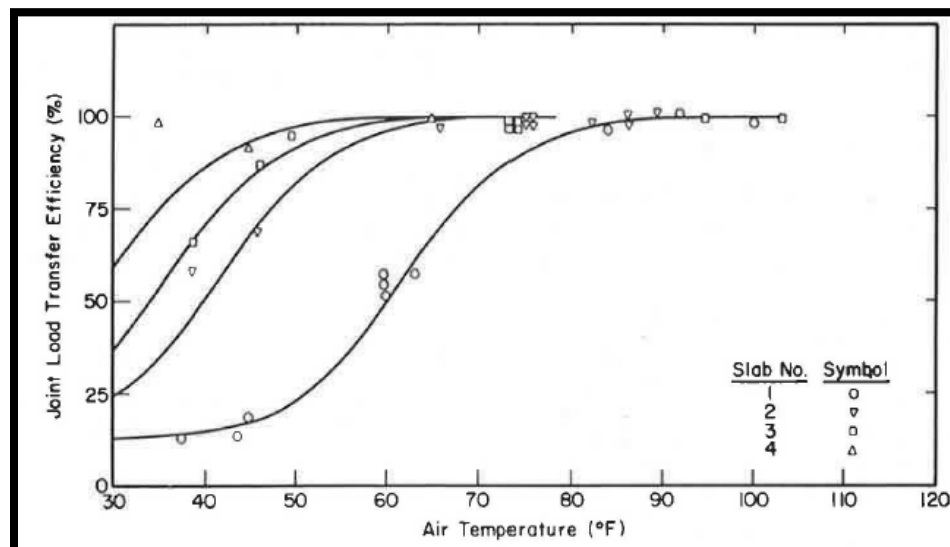
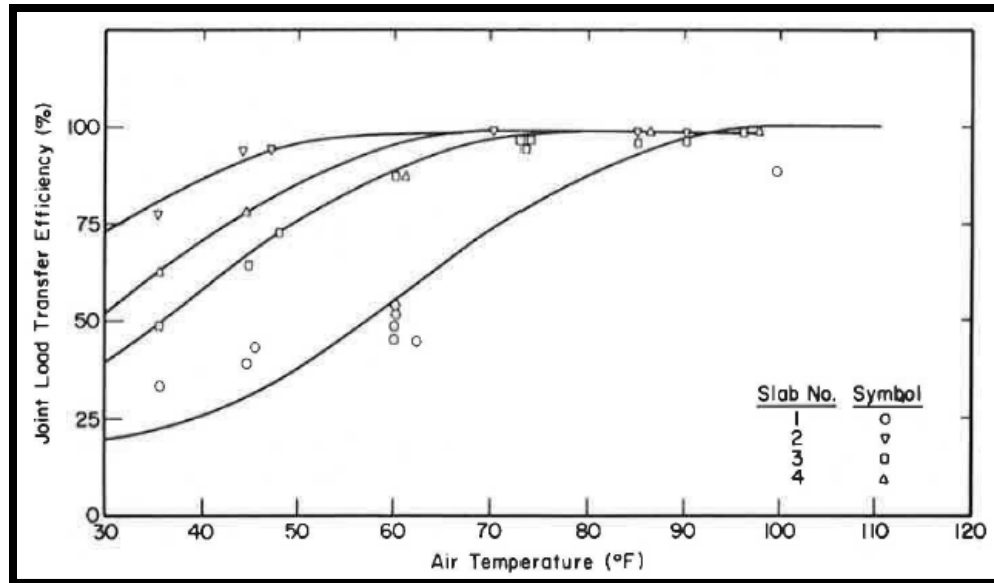


FIGURE 2.13 Relationship between air temperature and the load transfer efficiency along the transverse joint (Foxworthy & Darter, 1986).





**FIGURE 2.14 Relationship between air temperature and the load transfer efficiency along the longitudinal joint (Foxworthy & Darter, 1986).**

Guo and Marsey (2012) revealed that the load was almost linear to the deflection at the center location of the slab section as shown in Figure 2.15, but they were nonlinear to each other at edges and corners of the slab. This nonlinearity could be described by the upward curling of the concrete slab during October that led to the noticeable increase of deflections at joints and corners as shown in Figure 2.16.

Additionally, they deliberately mentioned that the LTD-ratio of unloaded and loaded deflections might be sensitive to traffic direction and not correctly reflected joint behaviors. Unlike the load transfer capability (LTD), the sum of the two deflections (SD) was likely to be constant for both traffic directions, and it could monitor the effect of temperature on the joint performance. In Figure 2.17, the left columns were the mean ratios of LTDs among the high and low sets of different tested directions while the right columns were the ratios of the SDs between the high and low sets. The chart clearly showed that

the ratios of SDs were almost consistent with the different traffic directions, while the LTDs between the high and low groups were substantially different.

Furthermore, as the season changed, the SD followed the trend of the changes in the slab caused by the curling characteristics of the slab, with no effects from the dummy and dowels. Also, the sum of different deflections on the loaded and unloaded sides could be used as an indicator of the relative degree of slab curling (Bianchini, 2013).

Sadeghi and Hesami (2018) used the FEM to observe the sensitivity of the LTE in jointed plain concrete pavements (JPCP). It was actually found that the LTE of the JPCP significantly increased when the elastic modulus and the thickness of the concrete slab and base layer increased. Besides, the coefficient of the friction between the concrete slabs had limited effect on LTE.

P501, H=28cm(11")	P501, H=24.8cm(9 3/4")	P501, H=22.9cm(9")
P306, H=15.6cm(6 1/8")	P306, H=14.9cm(5 7/8")	P306, H=15.2cm(6 ")
P154, H=21.3cm(8 3/8")	P154, H=21.9cm(8 5/8")	P154, H=16.8cm(6 5/8")
Sub-grade CBR=3-4	Sub-grade CBR=7-8	Sub-grade CBR=30-40
<b>LRS</b>	<b>MRS</b>	<b>HRS</b>

**FIGURE 2.15 Cross-sectional of tested pavement (Guo & Marsey, 2012)**

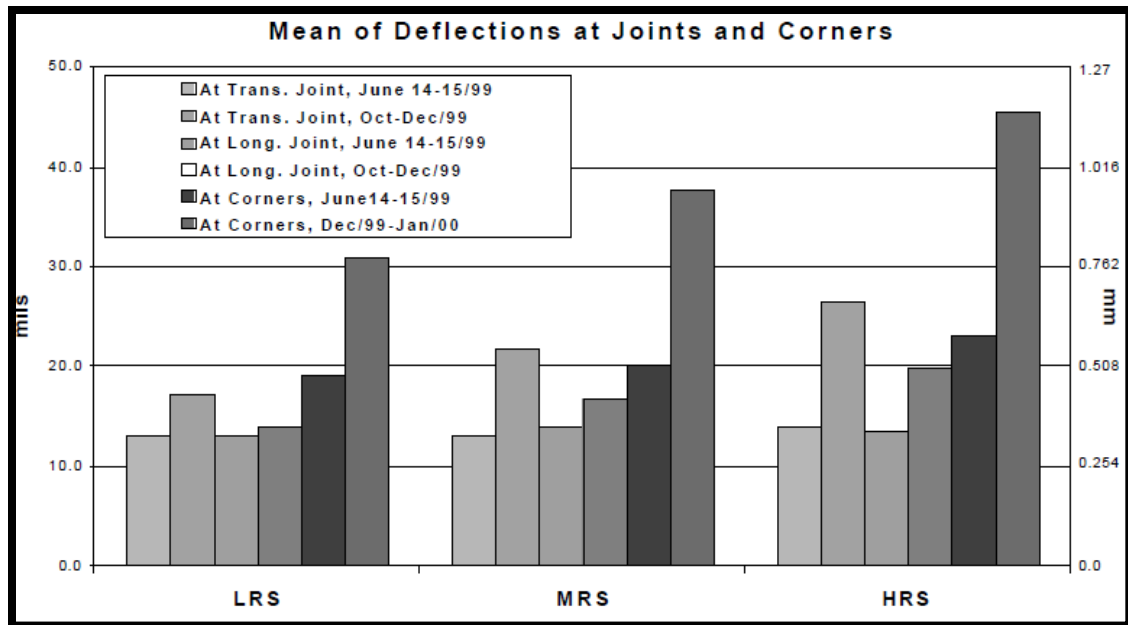


FIGURE 2.16 Deflection D0 at joints and corners (Guo & Marsey, 2012).

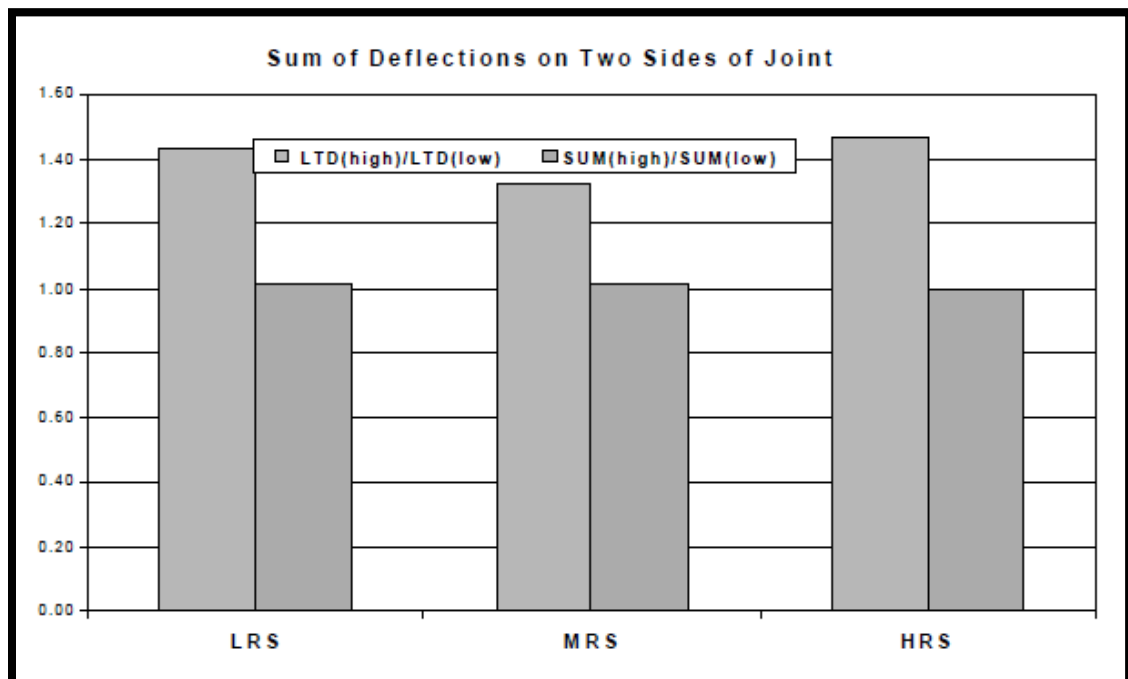


FIGURE 2.17 Comparison of properties of sum of deflections and load transfer coefficient (Guo & Marsey, 2012)

### **2.2.3 Effect of Slab Size on Pavement Performance and Load Transfer Efficiency**

Guo (2000) evaluated the effects of slab size on the performance of rigid pavement for the airfield. Theoretical analysis and the airport survey data were conducted in his research, and the analytical results showed that the maximum total stresses caused by combinations of aircraft loading with different temperature gradients in the larger slabs were higher than the maximum stresses found in the smaller slabs. Furthermore, the results showed that the slab width variations ranging from 15 to 25 feet did not significantly affect pavement performance when the analysis was considered only the load-induced responses. However, when the temperature variations were considered with slab size, the temperature stresses introduced in the larger slab were higher than those in the smaller slabs, as shown in Table 2.1. Moreover, the relationship between load transfer efficiency, the slab size and the slab temperature gradient were found. On one hand, the LTE increased only when the slab size increased with positive temperature gradient. On the other hand, the LTE decreased when the slab size increased with negative temperature gradient.

A statistical analysis of field survey data was also provided in the study. A survey of 288 million square feet of the pavement for the airfield facilities from 174 airports in the United States and Japan was taken. The slab sizes were classified into three groups and independently investigated for pavement condition index (PCI), which was the evaluation of pavement condition based on inspection and observation of the type, extent, and severity of pavement surface distresses. Then, a numerical indicator from the worst to the best ranging from 0 to 100 was provided to evaluate pavement condition. The results showed that the smaller slabs had higher pavement condition index than did the larger ones, as shown in Figure 2.18.

**TABLE 2.1 Maximum total deflections, transverse stresses, and load transfer index for a 50,000 lbs. single-wheel load (Guo, 2000).**

**A. Slab Width = 15 ft**

Response		$\delta_{l,max}$ (mils)			$\sigma_{l,max}$ (psi)			$LT'$		
$g_s$ °F/in		-1.5	0	1.5	-1.5	0	1.5	-1.5	0	1.5
$l$	$AGG/kl$									
39	5.1	2.9	13.6	21.0	315.4	355.9	471.6	0.67	0.76	1.00
50	7.3	0.9	15.7	27.3	283.2	319.6	388.5	0.66	0.75	0.91
83	24.3	11.3	31.5	55.9	289.7	307.5	316.2	0.68	0.72	0.74

**B. Slab Width = 20 ft**

Response		$\delta_{l,max}$ (mils)			$\sigma_{l,max}$ (psi)			$LT'$		
$g_s$ °F/in		-1.5	0	1.5	-1.5	0	1.5	-1.5	0	1.5
$l$	$AGG/kl$									
39	5.1	2.0	13.2	21.8	257.3	352.1	547.7	0.56	0.76	1.19
50	7.3	0.7	15.5	26.1	231.0	315.8	466.4	0.55	0.75	1.11
83	24.3	16.4	32.6	49.2	268.5	312.7	357.1	0.61	0.72	0.82

**C. Slab Width = 25 ft**

Response		$\delta_{l,max}$ (mils)			$\sigma_{l,max}$ (psi)			$LT'$		
$g_s$ °F/in		-1.5	0	1.5	-1.5	0	1.5	-1.5	0	1.5
$l$	$AGG/kl$									
39	5.1	0.6	13.0	24.2	197.2	352.2	591.7	0.43	0.77	1.29
50	7.3	-0.4	15.2	27.6	169.8	313.5	534.2	0.41	0.76	1.29
83	24.3	20.6	32.6	45.0	222.7	314.1	409.9	0.51	0.72	0.93

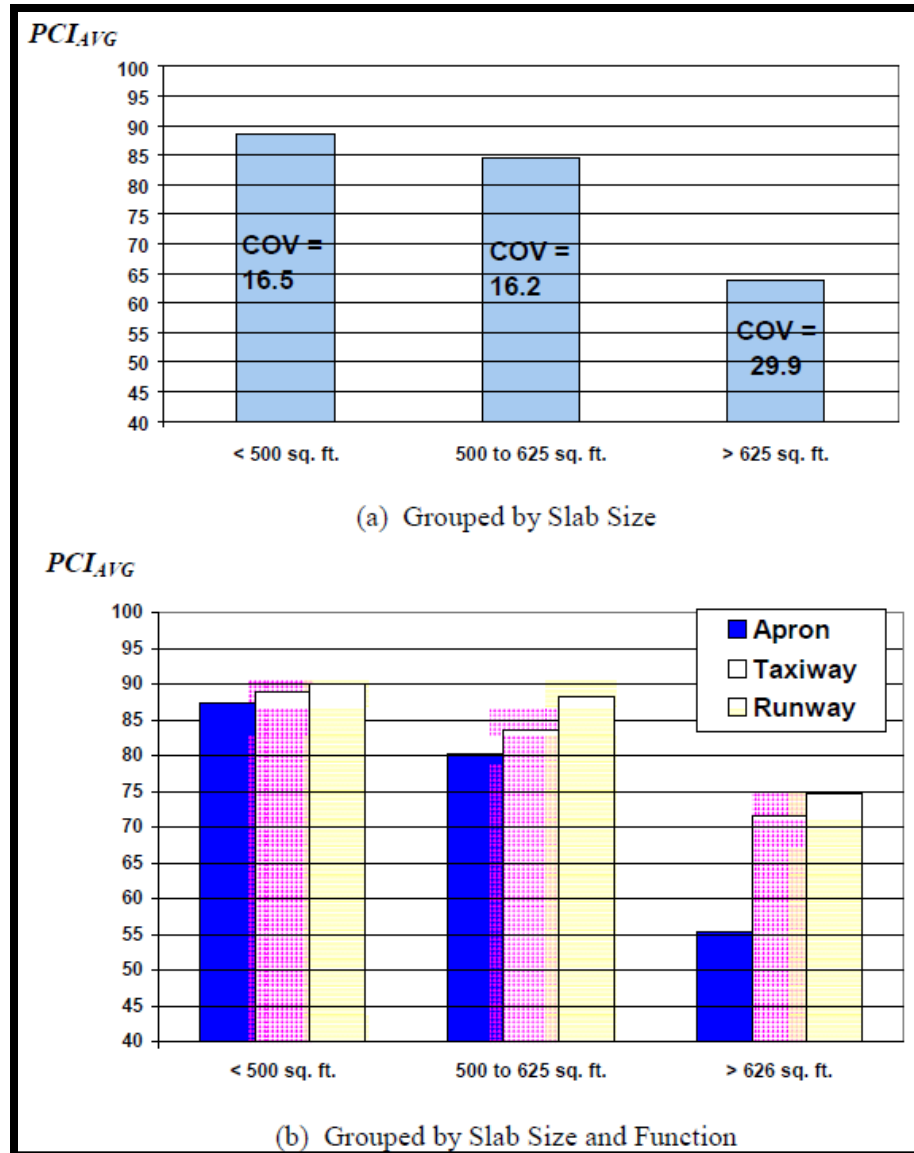


**FIGURE 2.18** Average pavement condition index of the investigated slabs from 174 airports in the United States and Japan (Guo, 2000).

## 2.3 Airfield Rigid Pavement Response Analysis

### 2.3.1 Finite Element Modeling of Rigid Pavement

For decades, several finite element analysis tools have been developed to monitor the structural response of rigid pavement systems. Some of those included ILLI-SLAB, FEAFAA, and EverFE. Some features of them were mentioned as follows.

ILLI-SLAB was one of the first finite element modeling software that used for the analysis of rigid pavement slabs, which provided by the University of Illinois. As ILLISLAB was firstly developed, 4-noded elements in a rectangular shape with twelve degree of freedom were coded in FORTRAN (Tabatabaie & Barenberg, 1978). In ILLISLAB, vertical spring elements (Winkler foundation) was used as the first foundation model. However, as the software was developed, new foundation model such as the elastic solid foundation was included. The analysis of rigid pavement layers in ILLI-SLAB was done by the classical medium-thick elastic plate theory. In this theory, the middle surface of the plate was abided the plane stress theory while the load would not introduce axial shear stress. One of the unique features of ILLI-SLAB was the ability to analyze any load configurations. The software transformed external loads to nodal loads by using an equivalent load vector. Also, it could compute stresses owing to the temperature gradients on the slab layer. Moreover, combinations of aggregate interlock, and dowels were considered as the mechanical load transfer factor in the ILLI-SLAB, which the aggregate interlock was expected to transfer shear stress, while the dowel bars were expected to transfer both flexural and shear stresses (Ioannides, Thompson, & Barenberg, 1985; Khazanovich & Gotlif, 2003; Smith, Peshkin, Darter, & Mueller, 1990).

FEAFAA was the stand-alone software developed by the FAA to compute the valid responses of rigid pavement on different types of aircraft landing gear loads. FEAFAA was able to analyze the multiple slab airfield rigid pavements using 3D finite element models (3D-FEM). In this program, the landing gear could be located at any point on the pavement surface since the pavement mesh model is the 3D editable uniform mesh size. Moreover, FEAFAA uses NIKE3D as the finite element processor which is the same

processor used in FAARFIELD. Following finite element analysis, the results of FEAFAA were shown in terms of stresses in three dimensions. However, FEAFAA did not contain a graphical processing unit. Thus, the FEM results needed to be viewed through such commercial software as Tecplot360.

EverFE was a three-dimensional finite element analysis tool for a rigid pavement that has been established to deal with the difficulty of model generation and result interpretation of the rigid pavement analysis. It featured graphical pre- and postprocessing skill to solve the difficulty in the generation of realistic 3D finite element models. Their features also accounted for the generation of realistic model problem including two rigid pavement slabs laying on a base layer and dense liquid foundation, and the combination of wheel and temperature loadings. Moreover, EverFE was able to model a joint shear transfer influenced by aggregate interlock and dowel shear transfer (Davids, Turkiyyah, & Mahoney, 1998). Thus, EverFE was fairly to be one of the 3D-FEM that could potentially be applied for research related to the rigid pavement.

### **2.3.2 Cracking Failure in Airfield Rigid Pavement**

Traditionally, the Federal Aviation Administration considered a cracking criterion of airfield rigid pavement as the bottom-up fatigue cracking only. This criterion was coded in the FAA Rigid and Flexible Iterative Elastic Layer Design or the FAARFIELD software.

However, this assumption might not adequately represent all of the failure patterns in the actual conditions of airfield rigid pavements. In some cases, it has been found that the top-down cracking failure mode was observed in the airfield rigid pavement. Thus, the



understanding of critical failure mode in numerous scenarios of airfield rigid pavement could be advantageous to the pavement engineer.

Evangelista and Roesler (2009) found that the top-down cracking possibly revealed under certain loading magnitudes and configurations. When the main gears or body-wing gears loaded on the same slab, it significantly impacted the top tensile stress, but it did not impact the bottom tensile stress. Moreover, they found that joint LTE was also another parameter that affected the critical top tensile stresses since the LTE affected the top tensile values more than the bottom tensile values.

In recent years, Rezaei-Tarahomi et al. (2017) provided sensitivity analysis of rigid pavement responses related to the top-down and bottom-up cracking mode. Various scenarios were considered based on the variations of the inputs in the NIKE3D-FAA and different combinations of loading locations of a Boeing 777-300ER, including the interior, corner, and edge loading on the slab.

The sensitivity of the number of analyzed elements was shown in Figure 2.19. It was found that the results were likely to be consistent when the number of elements was higher than 30 for the slab length of 25 feet on each side. Moreover, the normalized sensitivity evaluations of the interior, edge and corner loadings were shown in figure 2.20 to 2.22, in which the normalized sensitivity index (NSI) was defined as shown in Equation 2.4.

$$NSI = \frac{\Delta Y_j}{\Delta X_k} \frac{X_k}{Y_k} \dots \dots \dots \text{Eq.2.4}$$

Where

$X_k$  = Baseline value of input k  
 $\Delta X_k$  = Change in input k about the baseline

$$\begin{aligned}\Delta Y_j &= \text{Change in output J corresponding to } \Delta X_k \\ Y_k &= \text{Baseline value of output J}\end{aligned}$$

The findings could be summarized as follows:

- All stress responses were most sensitive to the slab thickness.
- Surface tensile stress was most sensitive to the base and sub-base thicknesses.
- Bottom tensile stress was most sensitive to the subgrade modulus.
- Surface tensile stress was more sensitive to the thermal coefficient than the temperature gradient, but the bottom tensile stress had an inverse relationship.
- Equivalent joint stiffness, base and sub-base modulus were less likely to affect the stress outputs.
- For the interior loading case, slab thickness and subgrade modulus were highly influencing all of the stress responses. Surface tensile stress was profoundly affected by the temperature coefficient and gradient whereas bottom tensile stress was significantly impacted by the subgrade modulus.
- For the edge loading case, top tensile stress was susceptible to all inputs while the bottom tensile was profoundly affected by the slab thickness and subgrade modulus. Nevertheless, they were both sensitive to the thermal coefficient and temperature gradient.
- For the corner loading case, when considered without thermal loading, the slab modulus and subgrade modulus both significantly affected the top and bottom stresses of the slab but when considered with thermal loading, the slab thickness had the highest normalized sensitivity index.

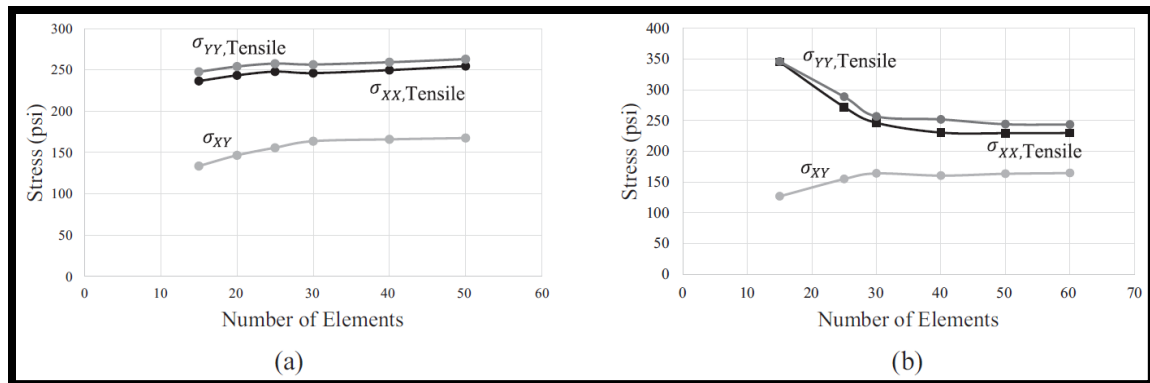


**FIGURE 2.19 Sensitivity of the analyzed elements of (a) slabs (b) foundation layers to the response in the FEAFAA (Rezaei-Tarahomi et al., 2017).**

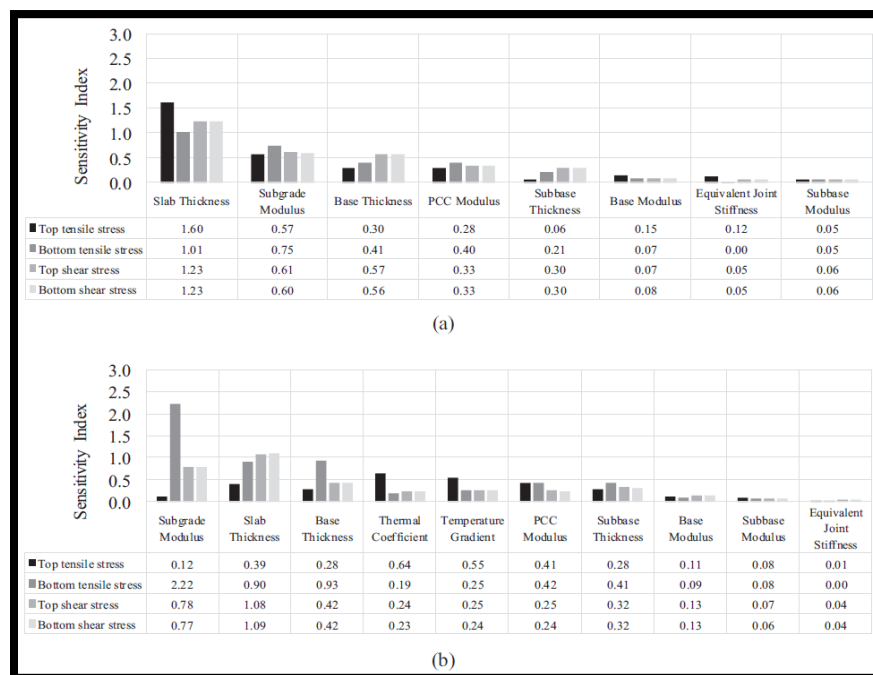


**FIGURE 2.20 Normalized sensitivity indexes of different inputs vs. critical responses for (a) the interior loading and (b) interior loading with temperature loading (Rezaei-Tarahomi et al., 2017).**

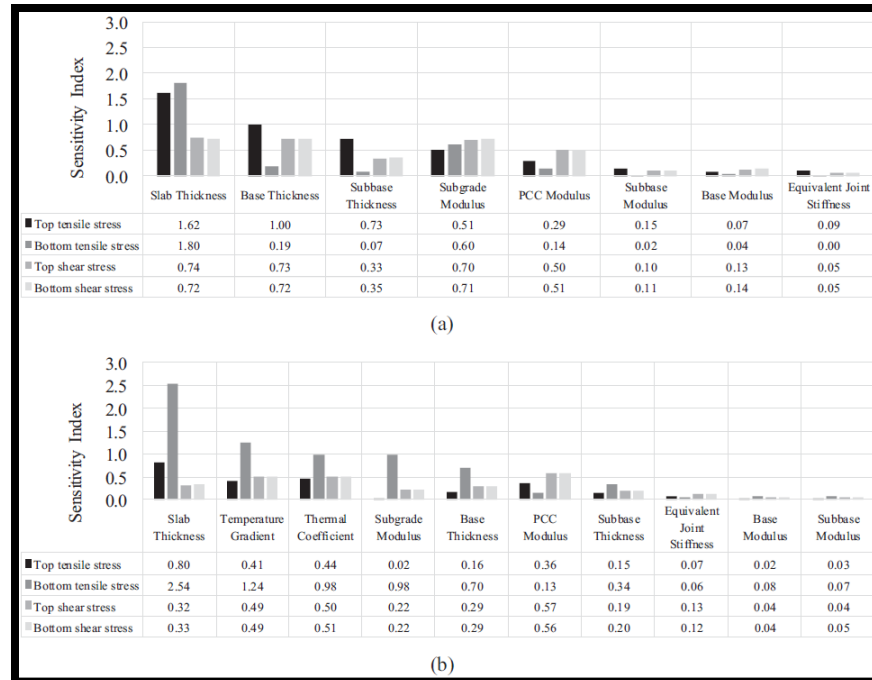


**FIGURE 2.21** The normalized sensitivity indexes of different inputs vs. critical responses for (a) the edge loading and (b) edge loading with temperature loading (Rezaei-Tarahomi et al., 2017).

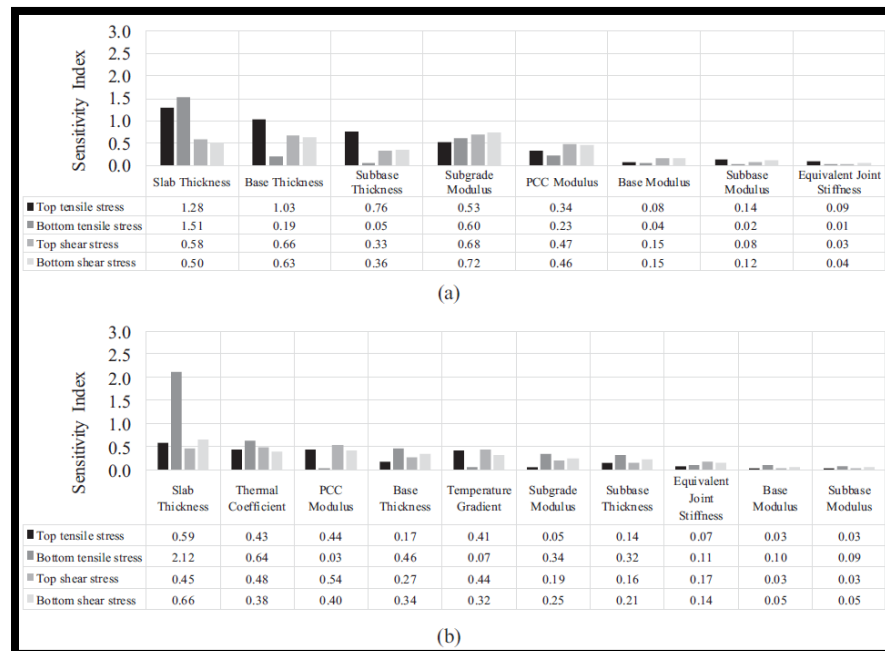


**FIGURE 2.22** The normalized sensitivity indexes of different inputs vs. critical responses for (a) the corner loading and (b) corner loading with temperature loading (Rezaei-Tarahomi et al., 2017).

Kaya et al. (In Press) conducted research related to the cracking failure characteristics of airfield rigid pavement with 2,000 different scenarios. The critical tensile stress at the slab surface and bottom were considered by selecting the higher maximum tensile stress in both X and Y directions. Then, the selected critical tensile stresses were compared with the maximum principal stresses.

While the majority of the critical failure mode occurred at the bottom location of the slab, there were a noticeable number of cases that critical failure happened at the top surface of the slab. Numerically, it was found that approximately 65% of all scenarios showing the bottom stresses were higher than the top stresses, whereas the rest 35% of all scenarios indicating the top stresses were greater than the bottom ones. However, as the temperature gradient became negative, the failure mode was likely to shift from bottom-up cracking to top-down cracking as seen in Figure 2.23. Therefore, the cracking failure mode should be carefully checked when the temperature gradient in a concrete slab were taking into account.

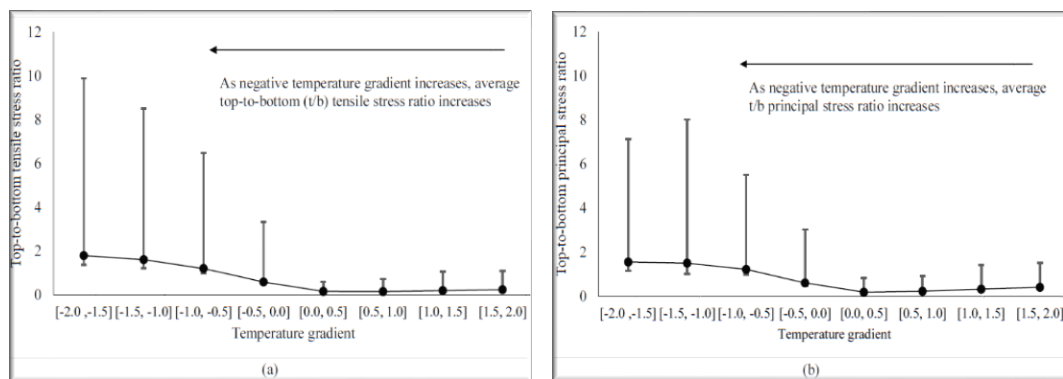


**FIGURE 2.23 Effect of temperature gradient on the ratio of top-to-bottom (a) tensile and (b) principal stress for 2000 scenarios (Kaya et al., In Press).**

## **2.4. FAA Rigid and Flexible Iterative Elastic Layered Design Software (FAARFIELD)**

FAARFIELD was the pavement design software based on mechanistic-empirical design procedures. The empirical failure models in FAARFIELD were derived from the full-scale traffic test at the National Airport Pavement Test Facility (NAPTF) in Atlantic City, NJ, USA (Federal Aviation Administration, 2011).

The input data in FAARFIELD were mechanistically analyzed by the two subprograms. The first program is LEAF-Layer Elastic Analysis FAA, which was mainly used in flexible pavement design. The second program was NIKE3D-FAA. It was the three-dimensional finite element analysis software chiefly applicable to rigid pavement design and the overlay design on the existing rigid pavement.

For rigid pavement design in FAARFIELD, several crucial design criteria were provided as follows. The bottom-up cracking of the concrete slab was the only mode considered in the design procedure. The pavement structural life was determined by the cracking that controlled by the maximum horizontal stress at the bottom edge of the concrete slab under edge loading assumption. The design stress was assumed as 75 percent of the critical edge stress computed by a three-dimensional finite element model because the FAA (2009) assumed that the free edge flexural stress of slab was sufficiently lowered by 25 percent owing to the amount of load transfer between slabs. The structural fatigue life of rigid pavement was represented by cumulative damage factor (CDF), which was the ratio of applied load repetitions to capacity of load repetitions to failure as shown in equation 2.5. The design process in the software iterated the design layer thickness until the CDF met a value of 1.0 which was the design criteria in FAARFIELD. As a result, the

FAARFIELD in practice became a reliable solution to the thickness requirement on the design of pavement structural life under the input traffic and existing soil conditions.

Furthermore, FAARFIELD supported the overlay design function of four different types of overlay including hot mix asphalt overlay of existing flexible pavement, concrete overlay of existing flexible pavement, hot mix asphalt overlay of existing rigid pavement, and concrete overlay of existing rigid pavement. In sum, this literature review mentioned above was mainly focused on the overlays of the existing concrete pavement in order to be congruent with the purpose of this study.

The key of overlay design on the rigid pavement was the consideration of deterioration of overlays and the existing concrete. The structural capacity of the existing pavement has been defined by structural condition index (SCI). According to FAA (2009), SCI was the accumulation of structural components from pavement condition index (PCI) which was the numerical rating of the condition of airfield pavement based on visual evaluation. The PCI score ranged from 0 to 100, with a higher score representing better pavement condition. With regard to the rigid pavement, there were 15 types of distresses that influenced the PCI score. Nevertheless, only six types of distresses were related to the computation of SCI. These six distresses were shown in Table 2.2. The SCI could be computed as shown in Equation 2.6.

The iterative processes for a trial thickness of the overlay were taken based on the failure model developed by Rollings (1988). The latest equation of the failure model for the overlay design was provided in the FAA's advisory circular, AC 150/5320-16, as shown in equation 2.7 and 2.8 (Garg, Guo, & McQueen, 2004). In equation 2.7, the pavement life function was considered by the ratio between concrete flexural strength ( $R$ )

and the working stress in the design ( $\sigma$ ). In the iterations of the overlay thickness, the condition in term of SCI at the end of the pavement life was assigned to  $SCI = 80$ , which meant half of the slabs was cracked. Therefore, the iterations in FAARFIELD iterated a new overlay thickness until the terminal design life met the required SCI.

However, when SCI was equal to 100, it meant no visible distress. Thus, the cumulative damage factor used (CDFU) was conducted to evaluate pavement's structural condition of the existing pavement accurately. The CDFU described the portion of life that had been used by the existing pavement until overlay, which could be computed as shown in Equation 2.9. This value was based on the forecast traffic and structure properties. If the actual traffic were noticeably excessive than the estimated traffic, then the CDFU would be set to 100 percent for the conservative design.

$$CDF = \frac{(Annual\ departure) * (life\ in\ years)}{\left(\frac{pass}{coverage\ ratio}\right) * (coverage\ to\ failure)} = \frac{Applied\ Coverages}{Coverage\ to\ failure} \dots\dots\dots Eq. 2.5$$

**TABLE 2.2 Rigid Pavement Distresses types for the Computational of Structural Condition Index (SCI) (Federal Aviation Administration, 2009).**

Distress	Severity Level
Corner Break	Low, Medium, High
Longitudinal/Transverse/Diagonal Cracking	Low, Medium, High
Shattered Slab	Low, Medium, High
Shrinkage Cracks (cracking partial width of slab) <sup>a</sup>	Low
Spalling–Joint	Low, Medium, High
Spalling–Corner	Low, Medium, High

$$SCI = 100 - a * \sum_{0 \leq i \leq m} f(Ti, Sj, Dij) \dots\dots\dots Eq. 2.6$$

Where

a	=	adjustment factor (ASTM D 5340)
m	=	total number of structural distress types
n	=	total number of severity levels for the distress
T	=	reduction factor for the type of distress
S	=	level of severity



D = existing density

$$SCI = \frac{\frac{R_F}{\sigma} - 0.2967 - F_S * (0.3881 + F_{SC} * 0.000039 * SCI) * \log_{10} COV}{0.002269} \dots \text{Eq. 2.7}$$

$$F_{SC} = \frac{0.392 - 0.3881 * F_S}{0.0039 * F_S} \dots \text{Eq. 2.8}$$

Where

$\sigma$  = working stress in the design  
 $R$  = flexural strength  
 $COV$  = coverage of the load  
 $F_{SC}$  = compensation factor to maintain  $SCI = 100$  for any  $R/\sigma$   
 $F_S$  = compensation factor

$$CDFU = \frac{L_U}{0.75 L_D} * 100 \text{ When } L_U < 0.75 L_D \dots \text{Eq. 2.9}$$

$$= 100 \text{ When } L_U > 0.75 L_D$$

Where

$L_U$  = number of operation years existing pavement until the overlay  
 $L_D$  = total design life of the existing pavement

FAA (2016) updated the new advisory circular (AC 150/5320-6F) with the latest version of FAARFIELD. Brill and Kawa (2017) found that the FAARFIELD 1.41 had provided more appropriate design thickness than the previous version since the earlier version, FAARFIELD 1.305, was too conservative. In rigid pavement designs, the improvement was achieved due to some modifications of FAARFIELD 1.41 as follows;

- Replacement of the improved mesh with several debugs.
- Change in design procedure (the maximum bending stress on the edge loading was reduced by 25 percent).
- Modification of the modulus determination procedure to the aggregate layer modulus assignment.

## **CHAPTER 3**

### **FIELD DEFLECTION ANALYSIS AND MODULUS BACKCALCULATION**

#### **3.1 F/HWD Test Database from round-up project of FAA**

In 2009, the Federal Aviation Administration (FAA) created the F/HWD round-up project in the National Airport Pavement Test Facility (NAPTF) in Atlantic City, NJ (Federal Aviation Administration, 2011). The FAA aimed to compare the collected F/HWD data from different test machines. They also targeted to compare back-calculated pavement material properties from different test machines. Therefore, there was an adequate number of tested data from this round-up project in the assessment of the sensitivity of using F/HWD testing.

##### **3.1.1 Facility Layout and Pavement Structure of F/HWD Test**

Construction of the round-up project started at the end of 2009. In the test layout, there were one section of rigid pavement and one section of flexible roadway. On the rigid pavement section, there were four slabs of 15 feet wide and 15 feet long while on the flexible pavement, the section was 60 feet long and 15 feet wide. The rigid and flexible pavements were built from one end to another end over a high strength subgrade of a CBR ranging from 25 to 30 percent as shown in Figure 3.1.

The slab structure was transversely reinforced by 1-1/4" doweled bars. The 20-inch doweled bar spacing was on the non-center area while the 15-inch doweled bar spacing was on the center area. A 16-inch height of P-501 PCC pavement was supported by 6-inch

of P-306 econocrete laying on the medium strength subgrade as illustrated in Figure 3.2. Additionally, temperature sensors were installed within the concrete pavement measured at three different depths at 0.5, 4.5, and 8 inches.

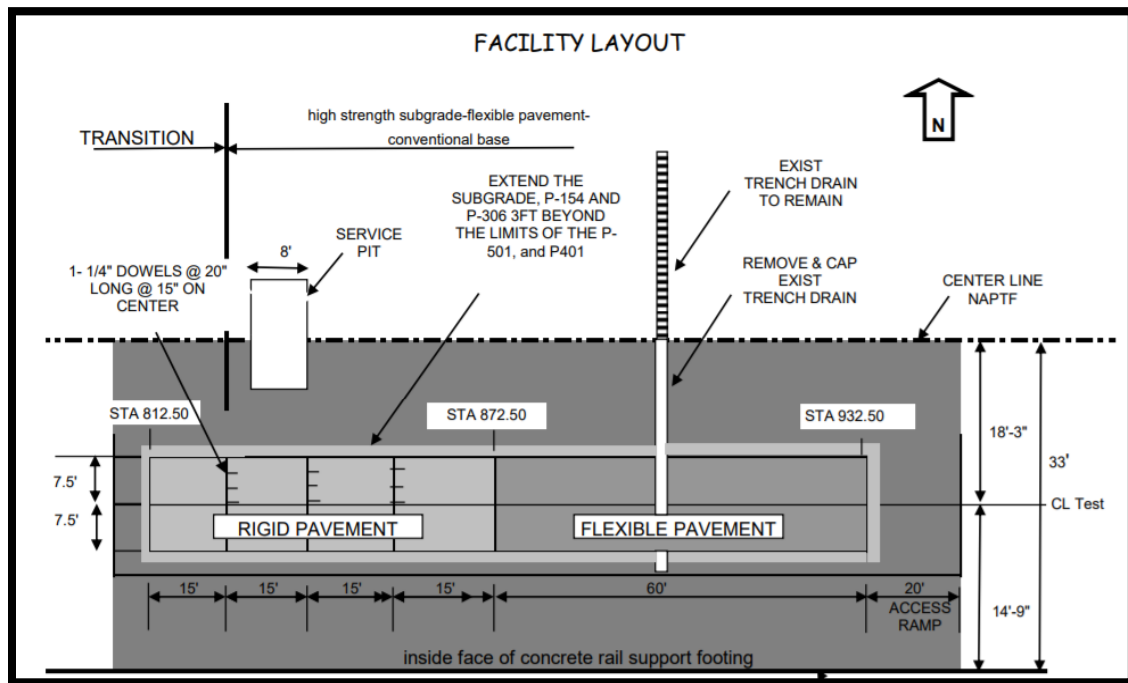


**FIGURE 3.1 the facility layout of the round-up project (NAPTF, 2010)**

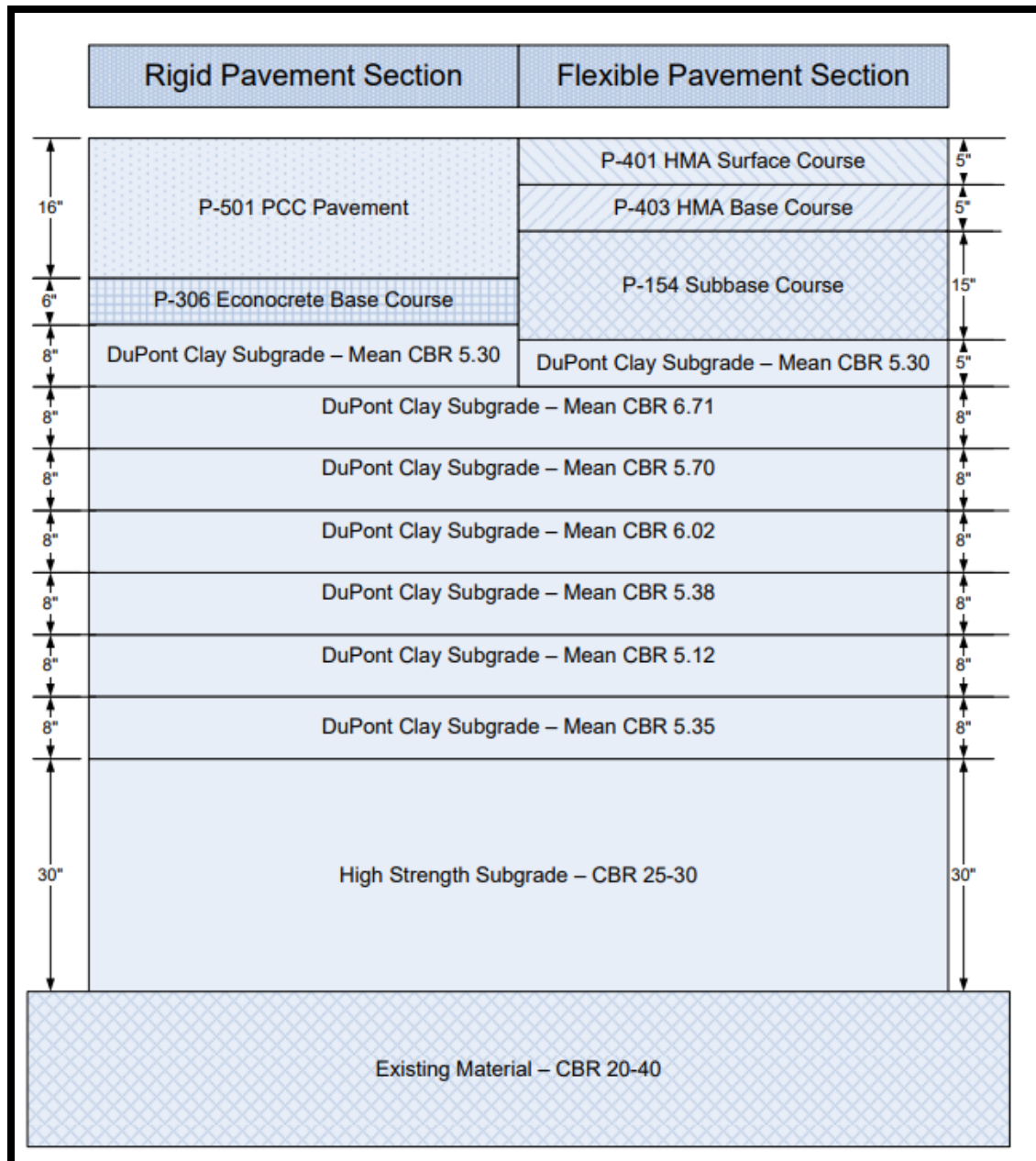


**FIGURE 3.2 Tested pavement structure (NAPTF, 2010)**

### 3.1.2 Test Plan of F/HWD Test

There were 33 test locations in this project where twenty-four out of which were tested on the rigid pavement. The drop locations were measured directly at the center of slabs, corner of slabs, the edge of the slabs as shown in Figure 3.3. The evaluated

deflections were tested by three load levels. Regarding the HWD testing, test drops were 12k, 24k, and 36k pounds. In this research, two different types of testing machine were purposely selected. The first type and the second types were the FAA KUAB and ERDC Dynatest, respectively. For the FAA KUAB, there were eight sensors. The negative offset sensor was located in front of the loading plate along the path of the vehicle and the remaining sensors were located from the center of loading plate to the rear track of the vehicle with 12-inch spacing from each sensor as illustrated in Figure 3.4. In relation to the ERDC Dynatest, there were seven sensors. One sensor was located at the center of the loading plate, and six sensors were located in front of the loading plate as shown in Figure 3.5.

There were some remarks in the round-up project that should be noticed. The first point was that the test period of this round-up project began in October 2010 and completed in April 2011. According to FAA record, it was found that the FAA KUAB testing conducted in October 2010 while the ERDC Dynatest tested in April 2011. Having done that, there appeared a deviation in terms of test temperature to which one should concern. The surface temperature of the tested section on the FAA KUAB tested date ranged between 69 to 72 °F whereas the surface temperature of the measured section on the ERDC Dynatest tested time ranged from 55.3 to 56.4 °F.

The second point was the test direction. F/HWD tests were conducted in two directions from west to east and from east to west. So, the effect of test directions was available in this analysis.

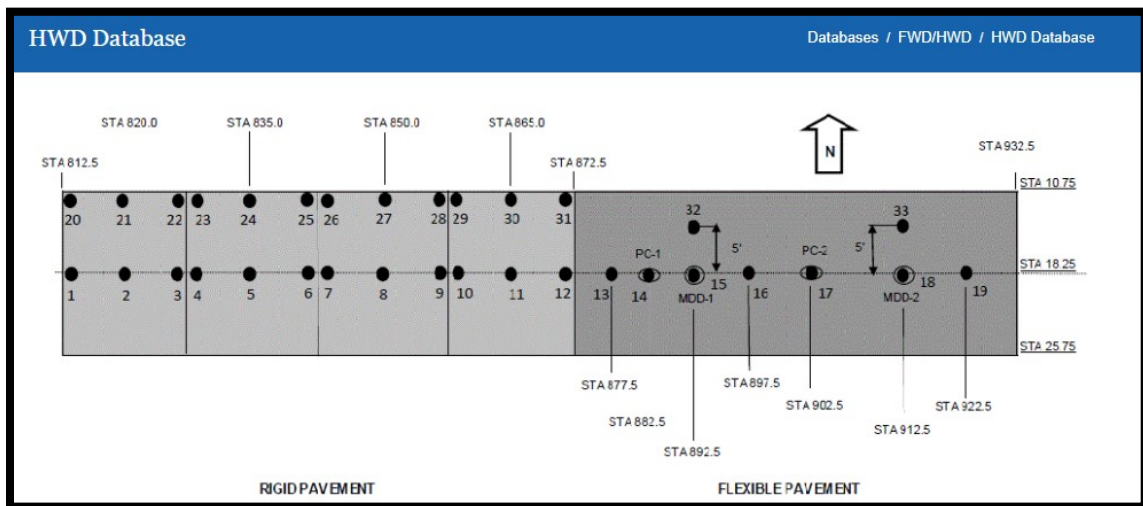
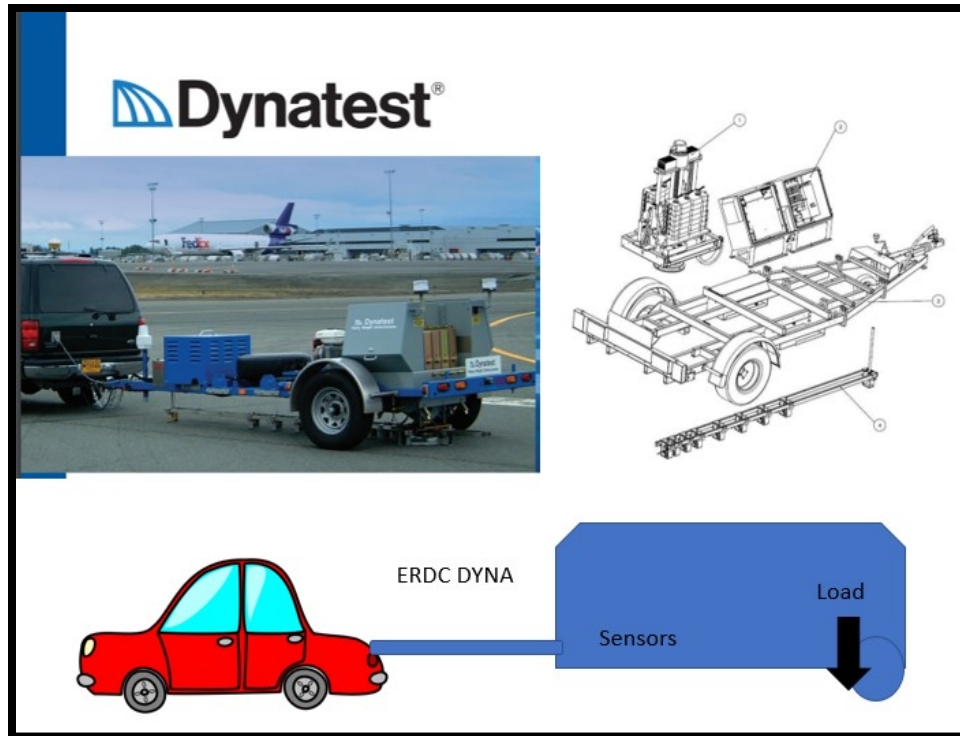


FIGURE 3.3 Drop locations (NAPTF, 2010).



FIGURE 3.4 Loading point and reading sensors layout diagram of FAA KUAB (Modified from (Douglas, Roesler, & White, 2009)).



**FIGURE 3.5 Loading point and reading sensors layout diagram of ERDC Dynatest (Modified from [www.dynatest.com](http://www.dynatest.com)).**

### 3.2 Deflection Analysis Using Field Data

In this section, the HWD data collected from FAA KUAB device were purposefully selected as the input to the study of the joint load transfer properties.

The relationship between deflections and load levels on different load locations of the concrete slab was shown in Figure 3.6. Firstly, it could be seen that the deflection on the corner of the slab (Loc.20) was highest followed by deflections on the free edge of the west side (Loc.1) and the free edge of the north side (Loc.21) of the slab respectively. Secondly, the deflection on the center of the slab (Loc.2) was the lowest followed by deflections on the center of the joint (Loc.3) and the corner of the joint (Loc.22) respectively. Lastly, the deflections from all locations were directly proportional to load levels.

For the deflection-based load transfer analysis, deflection data were collected from FAA KUAB tested data with one main reason as, unlike the ERDC Dyna, it provided the negative offset sensor data for monitoring the deflection of the unloaded slab. The ratio of deflection between the unloaded and loaded side of the slab—LTE—and a sum of deflection—SD-- was shown in Table 3.1. The averages and standard deviations of the LTE and SD of slab at jointed edge and jointed corner were provided in Table 3.2 and Table 3.3, respectively. Several findings were discovered as follows;

Firstly, the LTE and the SD increased as the load level increased. However, the standard deviations of the LTE were less sensitive to the amount of load while the standard variation of the sum of deflection changed directly as the load level increased.

Secondly, as the deflection-based LTE graphically shown in Figure 3.7, it could be illustrated that the LTE was lowest on the free edge corner of the slab followed by the free edge center, the jointed edge corner and the jointed edge center of the slab.

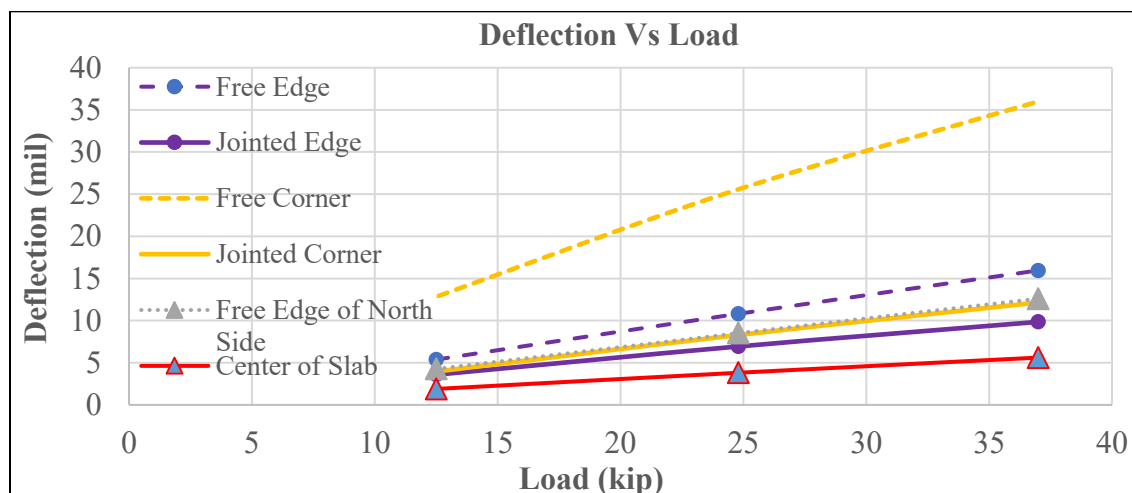


**FIGURE 3.6 Relationship between deflections and load levels on different load locations.**



**TABLE 3.1 LTE and SD at different loads and locations.**

Measured data				Offset, inches			LTE, %	Surface Temp. (°F)	Air Temp. (°F)	SD, mil
Location		Direction	Load (kips)	-12	0	12				
Middle of Joint	3	W-E	12.5	2.19	3.58	2.98	61	68	80	5.77
		W-E	24.8	4.63	6.93	5.83	67	68	80	11.56
		W-E	37.0	6.95	9.85	8.35	71	68	80	16.8
	4	E-W	12.6	2.35	3.72	3.07	63	71	79	6.07
		E-W	24.6	4.65	6.96	5.83	67	71	79	11.61
		E-W	37.0	6.89	9.88	8.35	70	71	79	16.77
	6	W-E	12.5	2.1	4.17	3.4	50	69	81	6.27
		W-E	24.8	4.29	7.86	6.5	55	69	81	12.15
		W-E	37.0	6.37	10.97	9.18	58	69	81	17.34
	7	E-W	12.6	2.13	3.59	2.98	59	70	79	5.72
		E-W	24.5	4.36	6.81	5.7	64	70	79	11.17
		E-W	37.0	6.58	9.79	8.27	67	70	79	16.37
	9	W-E	12.5	2.01	3.53	2.93	57	71	81	5.54
		W-E	24.8	4.12	6.62	5.55	62	71	81	10.74
		W-E	37.0	6.16	9.36	7.97	66	71	81	15.52
	10	E-W	12.6	2.07	3.2	2.67	65	71	79	5.27
		E-W	24.5	4.15	6.16	5.18	67	71	79	10.31
		E-W	37.0	6.12	8.77	7.5	70	71	79	14.89
Corner of Joint	22	W-E	12.6	3.99	7.25	6.13	55	61	65	11.24
		W-E	24.5	8.2	13.68	11.8	60	61	65	21.88
		W-E	37.0	12.16	18.96	16.45	64	61	65	31.12
	23	E-W	12.6	3.32	10.08	8.39	33	64	74	13.4
		E-W	24.5	7.46	17.64	14.88	42	64	74	25.1
		E-W	37.0	11.43	23.62	20.12	48	64	74	35.05
	25	W-E	12.6	3.79	8.93	7.57	42	62	66	12.72
		W-E	24.5	7.93	16.69	14.43	48	62	66	24.62
		W-E	37.0	11.63	22.92	19.67	51	62	66	34.55
	26	E-W	12.6	3.23	8.01	6.66	40	65	74	11.24
		E-W	24.5	6.93	14.86	12.57	47	65	74	21.79
		E-W	37.0	10.51	20.52	17.46	51	65	74	31.03
	28	W-E	12.6	2.65	7.88	6.57	34	62	67	10.53
		W-E	24.5	5.94	13.55	11.63	44	62	67	19.49
		W-E	37.0	9.35	18.45	15.85	51	62	67	27.8
	29	E-W	12.6	3.47	5.92	4.98	59	65	74	9.39
		E-W	24.5	6.99	11.13	9.55	63	65	74	18.12
		E-W	37.0	10.41	15.65	13.63	67	65	74	26.06

**TABLE 3.2 Average and standard deviation of LTE and SD of slab at jointed edge.**

Load (kip.)	LTE, %		SD, mil	
	Average	Stdv.	Average	Stdv.
12.5	59	5	5.77	0.36
24.8	64	5	11.26	0.66
37.0	67	5	16.28	0.91

**TABLE 3.3 Average and standard deviation of LTE and SD of slab at jointed corner.**

Load (kip.)	LTE, %		SD, mil	
	Average	Stdv.	Average	Stdv.
12.5	44	11	11.42	1.46
24.8	51	9	21.83	2.75
37.0	55	8	30.94	3.57

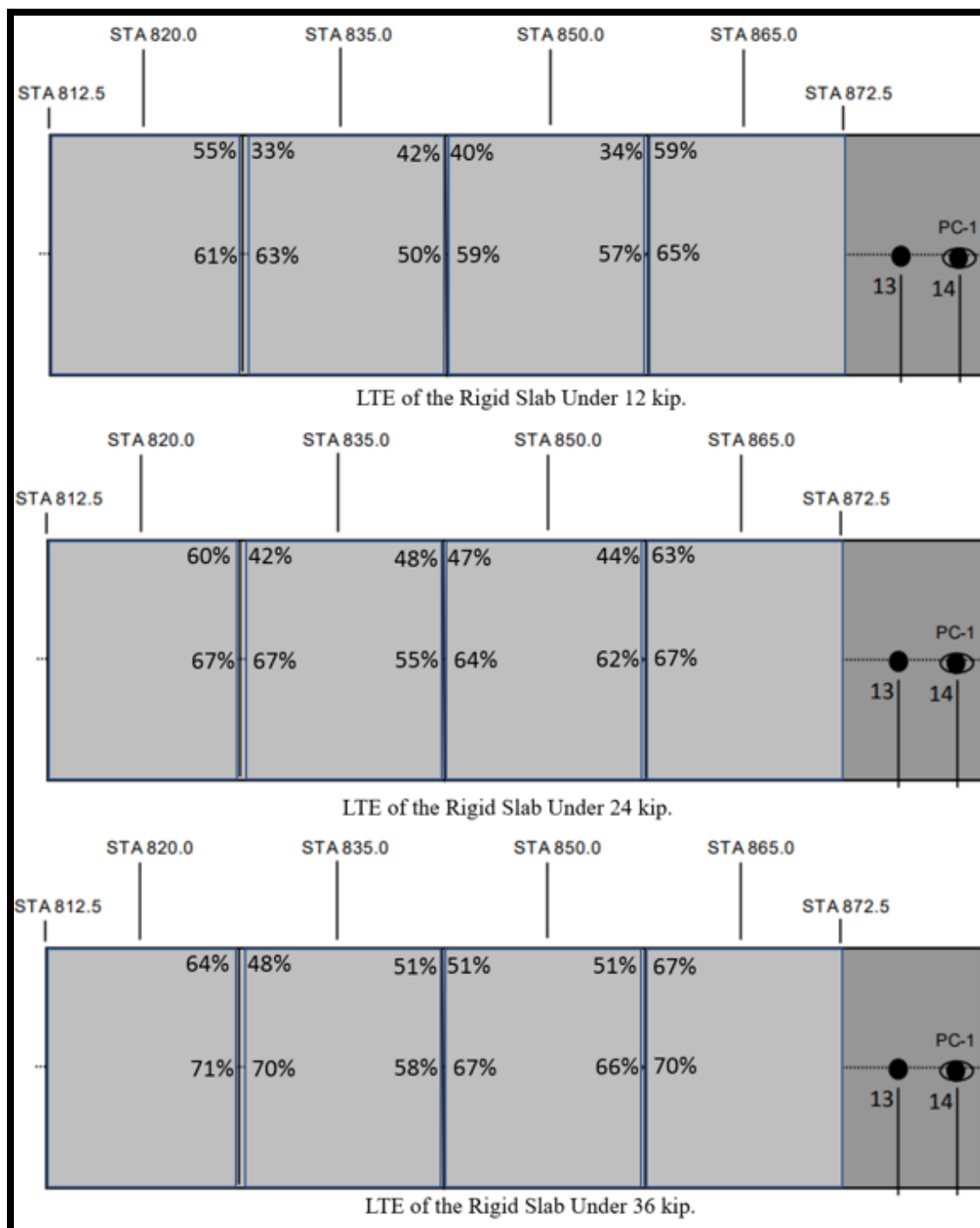


**FIGURE 3.7 Relationship between deflection-based LTE and load levels.**

### 3.2.1 Effect of Adjacent Support on Deflections

While the elastic modulus in the slab at location 5 and 8 -the two slab that located between the slab 2 and the slab 11- were marginally distinctive, the evaluated slab at position 2 and 11 showed a high variation in the outcomes due to the following factors. The first factor was the location of the tested slab. Seemingly, position 2 was located on the edge of the runway. On the west side of the slab at position 2, it was the shoulder of the pavement while on the east side there was the adjacent slab, slab 5. Therefore, there was a considerable variation in the radius of relative stiffness. It could be concluded that the radius of relative stiffness was high when the evaluated point was close to the shoulder whereas it was low when the monitored location was closed to the adjacent slab. The possible reason for this pattern was that there could be an additional stiffness provided by the adjoining slab.

The second factor was test-direction and the sensor configurations of the test machine. The actual deflection at location 2 evaluated by FAA KUAB in different directions was shown in Figure 3.8. Due to the sensor layout of FAA KUAB, the reading sensors were located behind the loading plate in a moving direction. Thus, the negative offset showed a deflection evaluating from the west to the east while the positive offset showed deflection assessing from the east to the west. At zero offset, it clearly showed that the two-deflection evaluated from both sides were almost identical. Also, the deflection basin assessed from the east to the west was steeper than that measured from the west to the east. In other words, the radius of relative stiffness evaluated from the east to the west was lower than that assessed from the west to the east.

Furthermore, the actual deflection at location 11 evaluated by FAA KUAB machine in different directions was shown in Figure 3.9. At zero offset, it was observed that the deflections estimated from both directions were nearly the same. However, the adjacent pavement condition of the slab at location 11 was not as the same condition as the slab at location 2. Visually, the east side and the west side of the slab at location 11 were the flexible pavement and the rigid pavement respectively. Therefore, the higher modulus of subgrade on the west side was expected because the concrete slab was stiffer than the flexible pavement. Fortunately, the deflection basin evaluated from the west to the east at location 11 was steeper than the deflection basin estimated from east to west as expected (Figure 3.9).

Additionally, the results obtained from ERDC Dynatest machine showed a similar relationship to the FAAKUAB's results. The actual deflection tested at location 2 and 11 were shown in Figure 3.10 and 3.11 respectively. It was noted that the deflection sensors of the ERDC were placed in front of the loading plate in a moving direction. Due to the different sensor layout compared with the FAAKUAB, it was reasonable to see the modulus of subgrade reaction of EWE2 and EEW11 were higher than that of EEW2 and EWE11 respectively.

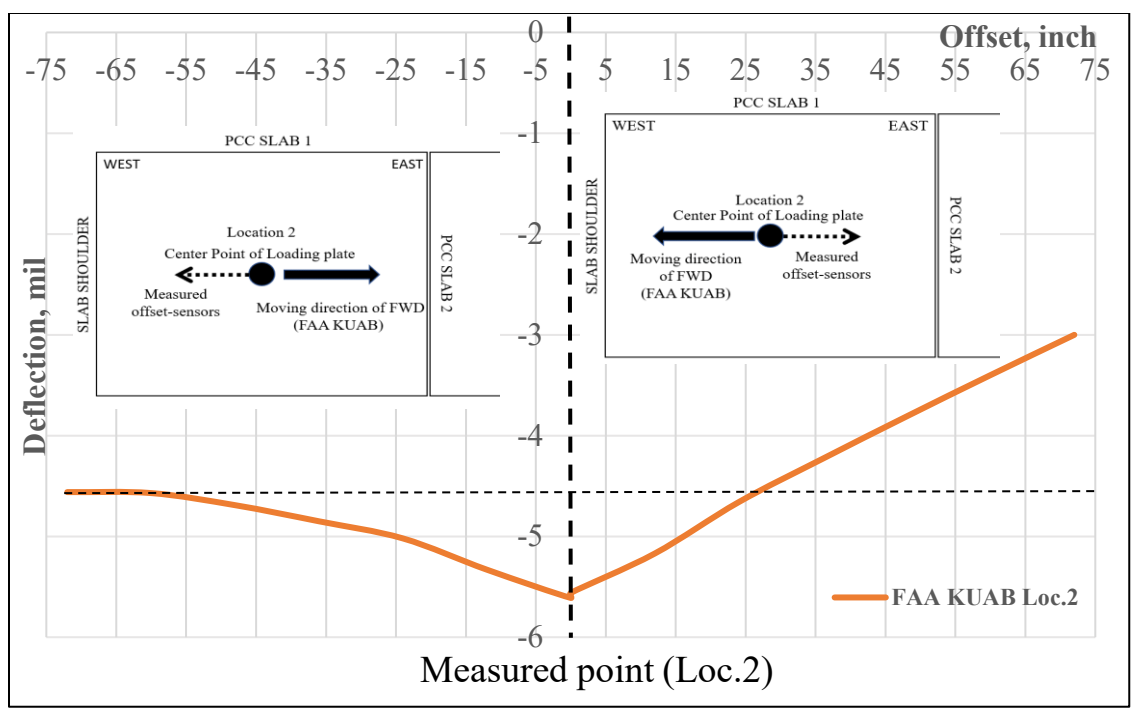


**FIGURE 3.8 Actual deflection at location 2 evaluated by FAA KUAB in different directions.**

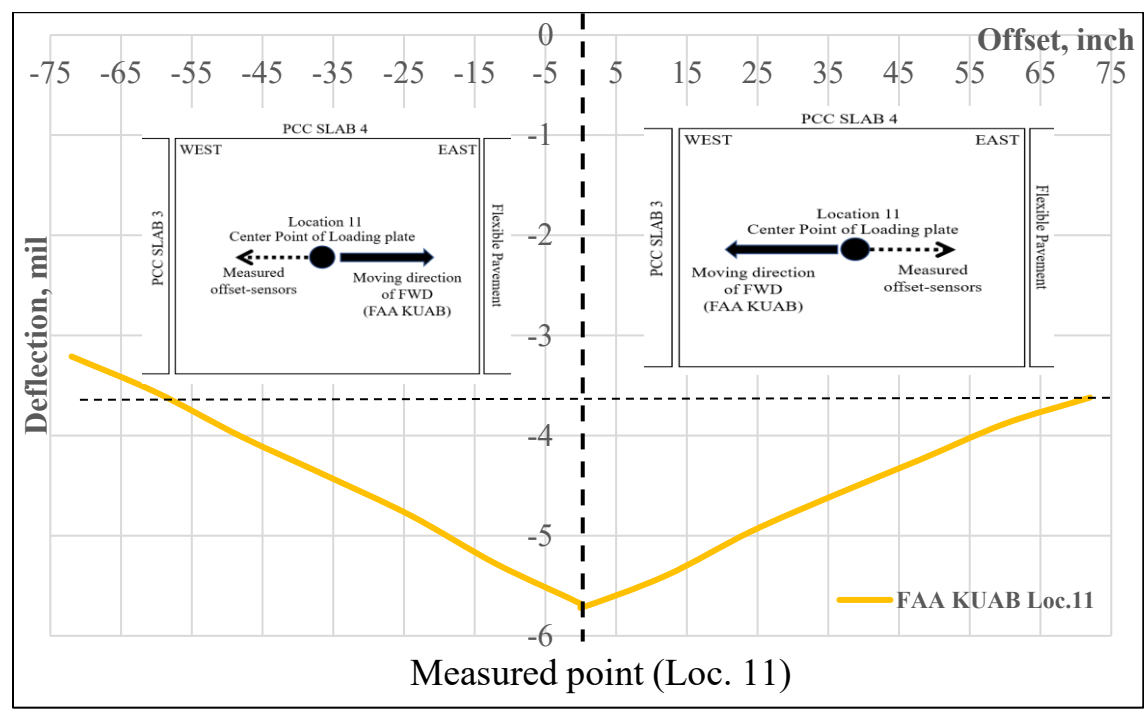


**FIGURE 3.9 Actual deflection at location 11 evaluated by FAA KUAB in different directions.**

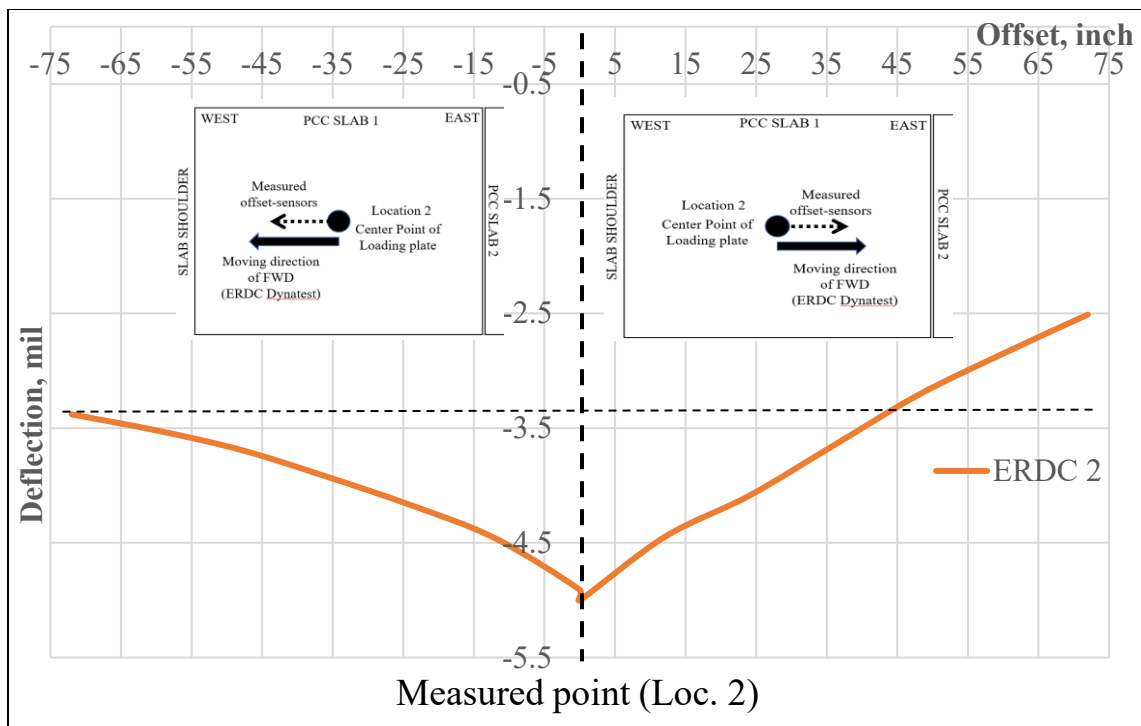


**FIGURE 3.10 Actual deflection at location 2 evaluated by ERDC DYNA test machine in different directions.**

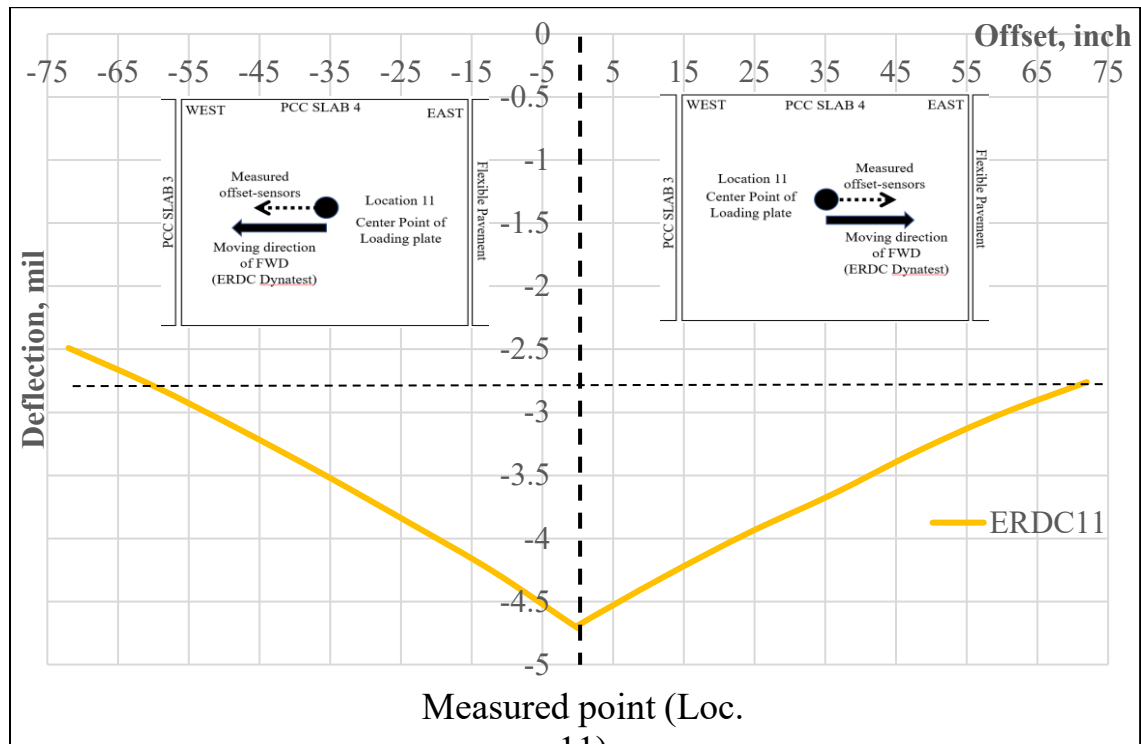


**FIGURE 3.11 Actual deflection at location 11 evaluated by ERDC DYNA test machine in different directions.**

### 3.3 Backcalculation Analysis Methods

The procedures in the back-calculation method on flexible pavement and rigid pavement were entirely dissimilar. As far as the flexible pavement was concerned, it is related to a higher degree of complexity due to its viscoelastic behavior (Ellis, 2008). The problem was that the viscoelastic materials possibly either acted as elastic solid or as a viscous liquid due to the changes in temperature. Consequently, the solution to back-calculate the parameters in the flexible pavement was more complicated than that of the rigid pavement.

Unlike the flexible pavement, the rigid pavement required a less computational process. For decades, various methods for back-calculating of the elastic modulus of Portland cement concrete and modulus of subgrade reaction of the rigid pavement have been quite available. Obviously, the two most famous methods have been known as the AREA method and the Best-fit method fundamentally based on Westergaard's solution to the interior loading of the infinite plate. In Westergaard's theory, a linearly elastic, homogeneous, and isotropic plate resting on a dense liquid foundation was assumed to be uniformly loaded over a circular area without considering temperature curling and moisture warping which could be analyzed with a closed-form solution. Therefore, the implementation of the back-calculation method in the rigid pavement was generally less complicated than that in flexible pavement.

For the sake of these research findings, the AREA Method and the best-fit-based method were preferably employed as the two main approaches for the back-calculation. Their procedures were provided as follows;



### 3.3.1 AREA Method for Rigid Pavements

This method was developed by Ioannides (1990). It was the back-calculation method that simplified the outcome by a relationship between AREA and the radius of relative stiffness based on Westergaard's theory of slab--a rigid plate placing at the top of the half-space of a rigid pavement supported by an assumed dense liquid or elastic solid foundation. Even though there were some such limitations for the AREA method as the uncertainty of back-calculation results due to the consideration on the deflection of a specific point instead of the entire deflection (Liu, Ling, Yang, Yuan, & Zhang, 2017), this method was more convenient than others because the computational software was not necessarily required. In general, there were three typical layouts for the sensor arrangement of FWD for the AREA method, AREA36, AREAS60, and AREA72. Due to the limitation of input data, the AREA36 was applied in this research as it required only four sensors while others needed seven ones to do so. The configuration of 4 sensor locations was shown in Figure 3.12.

Based on the AREA Method, the elastic modulus and the modulus of subgrade reaction could be obtained using Equation 3.1 to 3.6 and Table 3.4. AREA36 was calculated using Equation 3.1. The term  $dx$  was the vertical deflection monitored at  $x$  inches gap from the center of the load plate.

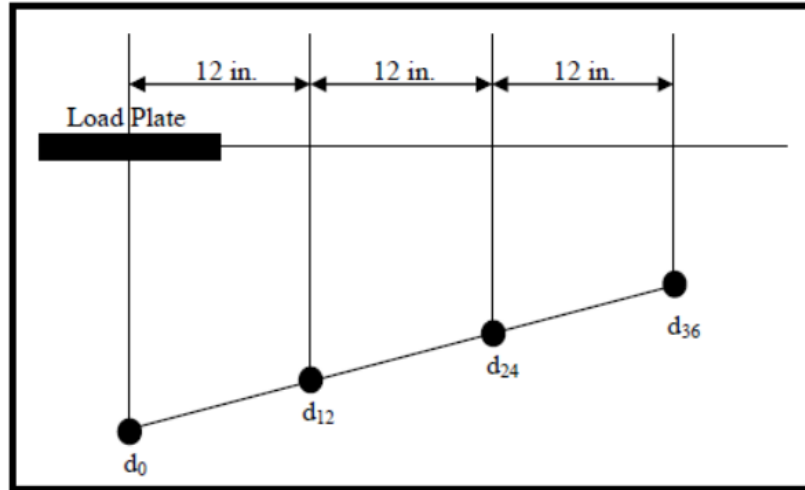


FIGURE 3.12 Sensor layout for AREA36 configuration (Ellis, 2008).

$$AREA36 = 6 * \left( 1 + 2 * \frac{d_{12}}{d_0} + 2 * \frac{d_{24}}{d_0} + \frac{d_{36}}{d_0} \right) \dots\dots\dots \text{Eq.3.1}$$

Then, the radius of relative stiffness could be calculated by Equation 3.2. For AREA36, the  $k_1$ ,  $k_2$ ,  $k_3$ , and  $1/k_4$  were equal to 36, 1812.597, 2.559, and 4.387 respectively.

$$l = \left( \frac{\ln\left(\frac{k_1 - AREA}{k_2}\right)}{-k_3} \right)^{\frac{1}{k_4}} \dots\dots\dots \text{Eq.3.2}$$

After that, a non-dimensional deflection coefficient ( $d_r^*$ ) was calculated by Equation 3.3

$$d_r^* = a * e^{-b * e^{-cl}} \dots\dots\dots \text{Eq.3.3}$$

Where:  $d_r^*$  = non-dimensional deflection coefficient  
 $a, b, c$  = constant coefficients from Table 1  
 $l$  = radius of relative stiffness

**TABLE 3.4 Constant Coefficients for Deflection Coefficients (Ellis, 2008).**

$d_x^*$	a	b	c
$d_0^*$	0.12450	0.14707	0.07565
$d_8^*$	0.12323	0.46911	0.07209
$d_{12}^*$	0.12188	0.79432	0.07074
$d_{18}^*$	0.11933	1.38363	0.06909
$d_{24}^*$	0.11634	2.06115	0.06775
$d_{36}^*$	0.10960	3.62187	0.06568
$d_{48}^*$	0.10241	5.41549	0.06402
$d_{60}^*$	0.09521	7.41241	0.06255
$d_{72}^*$	0.08822	9.59399	0.06118

The dynamic stiffness of subgrade was then obtained from Equation 3.4. Then, the elastic modulus of the concrete pavement was calculated by Equation 3.5. However, AASHTO (1993) suggested that the modulus of subgrade should be the static  $k$  value. Therefore, the dynamic stiffness of subgrade could be converted by dividing by two as shown in Equation 3.6(AASHTO, 1993).

$$k = (P * d_x^*) / (d_x * l^2) \dots \dots \dots \text{Eq. 3.4}$$

$$E_{pcc} = (12 * l^4 * (1 - \mu^2) * k) / h^3 \dots \dots \dots \text{Eq. 3.5}$$

$$k_s = k_d / 2 \dots \dots \dots \text{Eq. 3.6}$$

Where:	$k$	=	stiffness of subgrade (psi/in.)
	$P$	=	applied load (lbs.)
	$d_x^*$	=	on-dimensional deflection coefficient for deflection at distance $r$ from load
	$d_x$	=	measured deflection at distance $r$ from the load (in.)
	$l$	=	radius of relative stiffness (in.)
	$E_{pcc}$	=	elastic modulus of the pavement concrete slab (psi)
	$\mu$	=	poisson's ratio of concrete
	$h$	=	slab thickness (in.)

### 3.3.2 Best-Fit Procedure and Graphical NUS-BACK Solution

Similar to AREA method, the Best-Fit procedure employed Westergaard's solution to to the back-calculation of the elastic modulus by assuming a horizontally infinite plate on a dense liquid foundation. However, the critical difference between this method and the AREA method was that this method matched deflections point-by-point while the AREA method matched the theoretical deflection with the entire basin. Therefore, the Best-Fit method presented a better match between the calculated and measured basin (Ellis, 2008). Nevertheless, this method was limited due to the over combinations of variables in the equation including the radius of relative stiffness, the modulus of subgrade, and the elastic modulus of concrete slab as shown in Equation 3.7. Therefore, the Best-Fit method seemed to perform well only running with the software.

$$w(r) = \left(\frac{p}{k}\right) * f(r, l_k) \dots \dots \dots \text{Eq. 3.7}$$

Where:	w	=	vertical deflection
	r	=	radial distance from center load
	p	=	applied pressure
	k	=	coefficient of subgrade reaction
	$l_k$	=	radius of relative stiffness

However, there was another best-fit-based procedure namely NUS-BACK that existed in the form of a computer program and a graphical solution. The computer program was called NUS-BACK3. It could solve both the 3-layer system and 2-layer rigid pavement system whereas the graphical solution could deal with only 2-layer rigid pavement system. Since the graphical NUS-BACK solution did not require computer

software, it was chosen as one back-calculating approach in this research. There were several steps for the graphical solution as follows;

First, the ratio of the two deflections from the measured F/HWD data ( $D_{m_i} / D_{m_j}$ ) was computed. Then, the graphical charts, which provided the radius of relative stiffness ( $l$ ) for dense liquid foundation and elastic solid foundation, were shown in Figure 3.13 and Figure 3.14 respectively. Next, the deflector factor at distance  $r$  ( $F_K$  or  $F_E$ ) was obtained from the graphical chart in Figure 3.15. Lastly, all of the parameters derived from the graphical charts were applied to Equations 3.8 to 3.10 for dense liquid subgrades and Equations 3.11 to 3.13 for elastic solid subgrades.

$$D_{m1} = \left(\frac{P}{k\pi a^2}\right) * F_K(l_k, r_1) \dots \dots \dots \text{Eq. 3.8}$$

$$D_{m2} = \left(\frac{P}{k\pi a^2}\right) * F_K(l_k, r_2) \dots \dots \dots \text{Eq. 3.9}$$

$$l_k = \left(\frac{E_{PCC} h_{PCC}}{12K(1-\mu_{PCC}^2)}\right)^{\frac{1}{4}} \dots \dots \dots \text{Eq. 3.10}$$

$$D_{m1} = \left(\frac{P(1-\mu_S^2)}{E_S l_E}\right) * F_E(l_E, r_1) \dots \dots \dots \text{Eq. 3.11}$$

$$D_{m2} = \left(\frac{P(1-\mu_S^2)}{E_S l_E}\right) * F_E(l_E, r_2) \dots \dots \dots \text{Eq. 3.12}$$

$$l_E = \left(\frac{E_{PCC} h_{PCC}^3 (1-\mu_S^2)}{6E_S (1-\mu_{PCC}^2)}\right)^{1/3} \dots \dots \dots \text{Eq. 3.13}$$

Where:	$D_{m1,2}$	=	measured deflections
	$P$	=	applied load
	$K$	=	modulus of subgrade reaction
	$a$	=	radius of loaded area
	$E_S$	=	subgrade elastic modulus
	$\mu_S$	=	poisson's ratio of the subgrade
	$E_{PCC}$	=	elastic modulus of the pavement slab
	$h_{PCC}$	=	slab thickness
	$r_{1,2}$	=	horizontal distances of points 1 and 2 from the center of loaded area
	$l_{1,2}$	=	radii of relative stiffness

### 3.3.3 Slab Size Correction Factors

It was crucial to consider the influence of the slab size because the slab properties were backcalculated from different locations. Therefore, the measured deflections needed to be utilized. The slab size correction criteria were generally conducted when an effective slab dimension exceeded triple value of the radius of relative stiffness (Crovetti, 2006). The adjusted radius of relative stiffness and dynamic modulus of subgrade reaction were calculated using Equation 3.14 to 3.18.

$$L_{eff} = \sqrt{L_s * L_w} \dots \dots \dots \text{Eq. 3.14}$$

$$CF_{lk-est} = 1 - 0.89434e^{(-0.61662(\frac{L_{eff}}{l_{k-est}})^{1.04831})} \dots \dots \dots \text{Eq. 3.15}$$

$$CF_{Di} = 1 - 1.15085e^{(-0.71878(\frac{L_{eff}}{l_{k-est}})^{0.80151})} \dots \dots \dots \text{Eq. 3.16}$$

$$l_{k-adj} = CF_{lk-est} * l_{k-est} \dots \dots \dots \text{Eq. 3.17}$$

$$k_{adj} = \frac{k_{est}}{CF_{lk-est}^2 * CF_{Di}} \dots \dots \dots \text{Eq. 3.18}$$

Where:	$L_{eff}$	=	effective length of slab dimensions, inches
	$L_s$	=	slab length, inches
	$L_w$	=	slab width, inches
	$CF_{lk-est}$	=	correction factor for estimated dense-liquid radius relative stiffness
	$CF_{Di}$	=	correction factor for utilized maximum interior
	$l_{k-adj}$	=	adjusted radius of relative stiffness
	$k_{adj}$	=	adjusted modulus of subgrade reaction
	$l_{k-est}$	=	non-adjusted radius of relative stiffness
	$k_{est}$	=	non-adjusted modulus of subgrade reaction

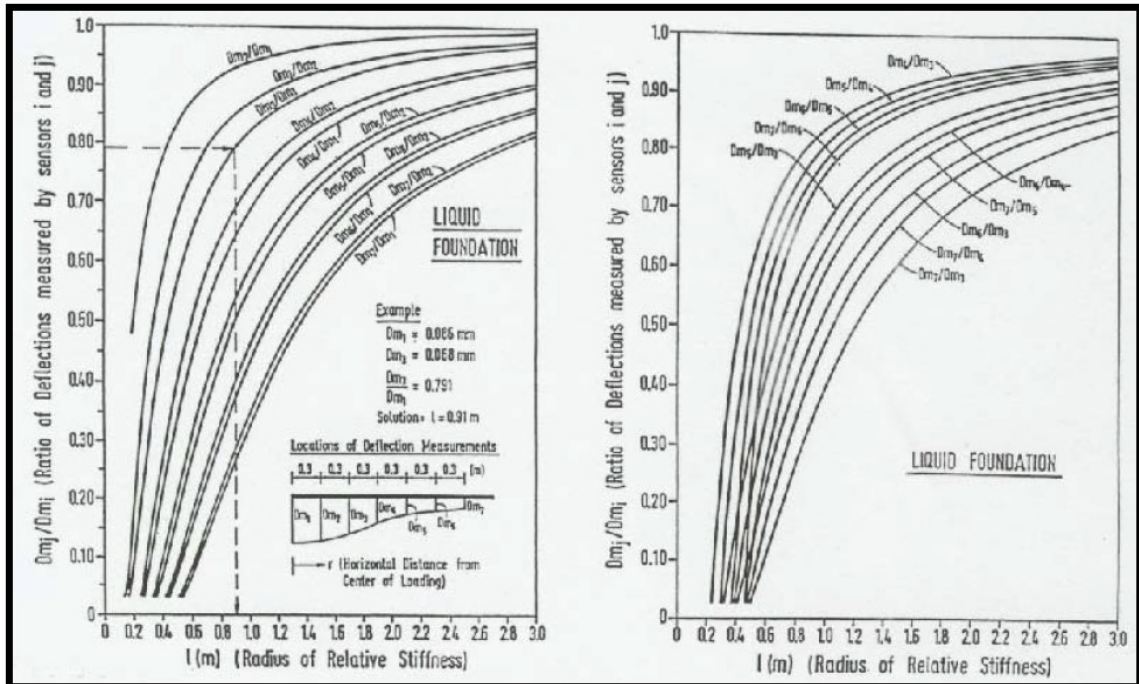


FIGURE 3.13 Graphical chart for radius of relative stiffness of dense liquid (Ellis, 2008).

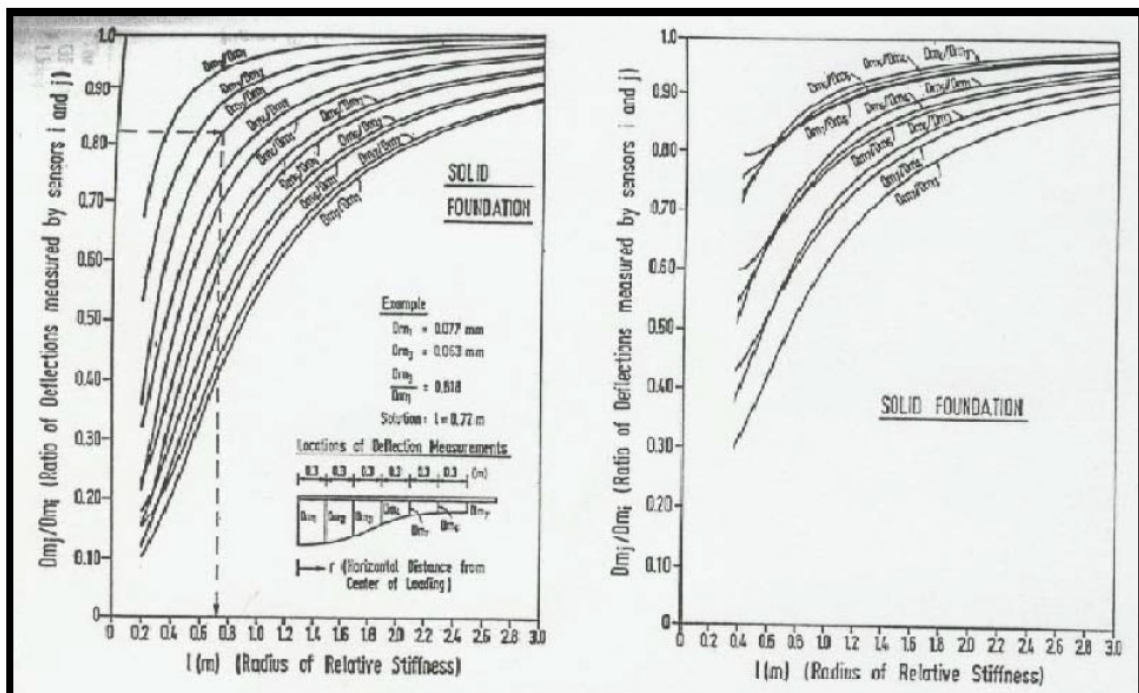


FIGURE 3.14 Graphical chart for radius of relative stiffness of elastic solid (Ellis, 2008).

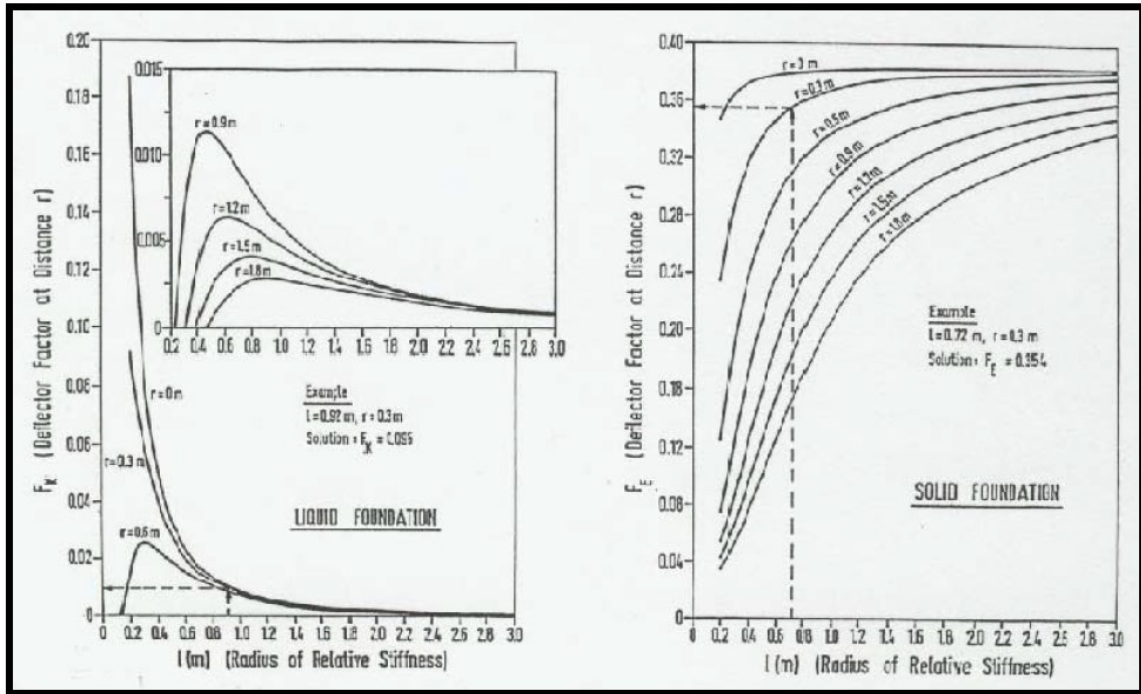


FIGURE 3.15 Graphical solutions for deflector factor (Ellis, 2008).

### 3.4 Backcalculation Results

#### 3.4.1 Comparison Between AREA Method and NUS-BACK Solution

From AREA method, the back-calculated results of the four connected slabs were shown in the following tables. The elastic modulus and the modulus of subgrade reaction of the slab at location 2, 5, 8, and 11 were shown from Table 3.5 to 3.8 respectively. When considering the slab size correction factor, the elastic modulus and the modulus of subgrade reaction of the adjusted slab at location 2, 5, 8, and 11 were shown from Table 3.9 to 3.12 respectively.

From NUS-BACK method, the elastic modulus and the modulus of subgrade reaction of the slab at location 2, 5, 8, and 11 obtained by NUS-BACK graphical solution were illustrated in Table 3.13 to 3.16 respectively. When considering the slab size



correction factor, the elastic modulus and the modulus of subgrade reaction of the adjusted slab at location 2, 5, 8, and 11 were shown from Table 3.17 to 3.20 respectively.

The boxplot of the results of the modulus of subgrade reaction with and without slab correction factor calculated by the AREA Method and the NUS-BACK Solution was presented in Figure 3.16. It was found that the results obtained by AREA method were more varying than the NUS-BACK (Figure 3.16). When the slab correction factors were not taken into account, the average modulus of subgrade reactions from the four tested slabs calculated by the AREA method was slightly higher than the NUS-BACK method with the figures between 216.16 and 201.91 pci. However, when considering the modulus of subgrade reaction with the slab correction factor, the outcomes showed the opposite trend. The average modulus of subgrade reactions obtained by NUS-BACK solution was 286.86 pci while the results obtained by AREA method were only 277.94 pci.

The boxplot of the elastic modulus of concrete slab with and without slab correction factors obtained by the AREA Method and the NUS-BACK Solution was illustrated in Figure 3.17. Unlike the variation in the results of the modulus of subgrade reaction, the elastic modulus of the concrete slab backcalculated by the AREA method was less varying than that of the NUS-BACK solution. From the box plot, it showed that the slab correction factors did not significantly affect the back-calculated moduli. The results backcalculated by the AREA method were ranging between 4340 ksi and 5540 ksi from the first and the third quartile while the back-calculated moduli obtained by the NUS-BACK were ranging between 6160 ksi and 8530 ksi.

### 3.4.2 Comparison Between Back-calculated and Lab Test Results

Lab test results from the FAA are selected as the reference values in which the bending strength of the P501 and compressive strength of P306 were converted to elastic modulus by Equation 3.19 and 3.20 respectively. If the unit weight were known, the elastic modulus would also be obtained from equation 3.21. Moreover, the resilient modulus of the subgrade layer was converted to the modulus of subgrade reaction by Equation 3.22.

The back-calculated moduli layers with slab size correction factors of the AREA method and NUS-BACK were compared with the FAA lab test results as shown in Table 3.21. It could be argued that the average slab modulus calculated by the AREA method was closely tied to the modulus from lab test while the average slab modulus obtained by the NUS-BACK graphical method was significantly higher than that of the lab test result. Moreover, modulus of subgrade reaction obtained by a plate load test and the lab test result calculated by Equation 3.16, was 111 pci and 108 pci, respectively. These value were considerably lower than the back-calculated modulus of subgrade reaction from both AREA and NUS-BACK methods. However, it would not be surprising that the k-values obtained by the AREA method and NUS-BACK were greater than those of the lab test result since the backcalculated k-values of the AREA method and NUS-BACK were the composite modulus of subgrade reaction from both the base (Econocrete P306) and the subgrade layer.

$$F_r = 43.5 * E * 10^{-6} + 488.5, (\text{psi}), (\text{ERES Consultants, 1987}) \dots\dots\dots \text{Eq. 3.19}$$

$$E = 57000 \times \sqrt{(F_c')}, (\text{psi}), (\text{American Concrete Institute, 2014}) \dots\dots\dots \text{Eq. 3.20}$$

$$E = 33000K_1w_c^{1.5} \times \sqrt{(F_c')}, (\text{ksi}), (\text{AASHTO, 2017}) \dots\dots\dots \text{Eq. 3.21}$$

$$E_{SG} = 20.15 * K^{1.284}, (\text{Federal Aviation Administration, 2016}) \dots\dots\dots \text{Eq. 3.22}$$

### 3.4.3 Effect of Test Condition and Device

According to the backcalculated results from Table 3.6 to 3.21, the effects of test location, test direction, and sensor configuration of the F/HWD devices on backcalculated modulus could be observed as follows.

Firstly, there was a high variation on the backcalculated slab modulus at location 2. The computed moduli at location 2 were ranged from 8160 ksi to 15900 ksi, while the computed slab moduli at other locations were much less varied than the results from location 2. The main factor that caused a high variation at location 2 was a distinct pavement condition at location 2. It could be seen that the west side of the slab at location 2 was connected with the shoulder pavement made of P-401 HMA surface laid on 5 feet lift of dense grade aggregate that placed on the excavated high strength subgrade, while the east side was jointed with the rigid pavement. In contrast, the other test locations were jointed on both sides with either rigid pavement or flexible pavement that had considerable stiffer pavement structure than a shoulder pavement. Therefore, the obtained moduli at location 5, 8, and 11 were more consistent than the moduli at location 2.

Secondly, the backcalculated modulus was influenced by the test direction. It could be found that the backcalculated modulus at all location was changed as the F/HWD machine moved in opposite direction. Moreover, it was observed that those changes influenced by the interrelationship between the test direction and the sensor configuration of the device. It should be noticed that the deflection basins that used for the backcalculation could be disturbed as the test direction changed because each test machine had their specific sensor configuration layout. Once the test direction changed, the sensor configuration also changed. For example, the deflection sensors of the FAA KUAB were

generally located behind the loading plate in moving path but the deflection sensor of the ERDC Dynatest were placed in front of the loading plate in moving path. When the FAA KUAB moved from the west to the east at location 2, the measured deflection basin would be the deflection basin on the west of location 2. However, when the FAA KUAB moved from the east to the west at location 2, the evaluated deflection basin would be the deflection basin on the east of location 2. Therefore, the deflection basin used in the backcalculation from different test directions would be different. Thus, the backcalculated modulus from different test directions would be inconsistent.

Thirdly, the sensor configuration of test machine could impact the backcalculated modulus. As mentioned above that the sensor configuration of FAA KUAB and ERDC Dynatest were placed differently. Then, the evaluated deflection basin from different test machines used for the backcalculation would be dissimilar. For example, when the test direction changed from W-E to E-W, the slab modulus (AREA Method) at location 2, 5, 8 observed by the FAA KUAB decreased, while the slab modulus (AREA Method) observed by the ERDC Dynatest increased. Moreover, as the test direction changed from W-E to E-W, the slab moduli evaluated by FAA KUAB at location 11 increased, while the slab moduli measured by ERDC Dynatest decreased.

Lastly, the backcalculated results obtained from the two HWD devices at each location except location 2 were comparable to each other (Figure 3.18), if they were compared to each other in opposite test direction. This confirmed that the outputs were highly affected by the test directions and the sensor configurations of the HWD devices.

**TABLE 3.5 Backcalculated result of slab at location 2 without slab size correction by AREA Method.**

Test Machine	Tested Direction	Location	Load, kip	D0", mil	D12", mil	D24", mil	D36", mil	AREA	l, radius of relative stiffness	l ave,est	Kd, psi/in	Ks, psi/in	Epcc, ksi
FAA KUAB	W-E	2	12.5	1.89	1.78	1.7	1.62	33.238	59.172	60.519	223	111	8.55E+03
FAA KUAB	W-E	2	24.8	3.81	3.63	3.43	3.29	33.417	61.904				
FAA KUAB	W-E	2	37.0	5.61	5.33	5.02	4.85	33.326	60.480				
FAA KUAB	E-W	2	12.6	1.91	1.79	1.61	1.47	31.979	45.548	43.173	436	218	4.34E+03
FAA KUAB	E-W	2	24.6	3.83	3.47	3.15	2.84	31.191	39.977				
FAA KUAB	E-W	2	37.0	5.56	5.17	4.66	4.23	31.781	43.994				
ERDC	W-E	2	11.2	1.62	1.45	1.33	1.2	31.037	39.056	38.140	581	291	3.52E+03
ERDC	W-E	2	23.7	3.39	3	2.74	2.48	30.708	37.226				
ERDC	W-E	2	34.7	5	4.45	4.09	3.65	30.876	38.137				
ERDC	E-W	2	11.1	1.59	1.43	1.33	1.24	31.509	42.045	43.359	457	228	4.62E+03
ERDC	E-W	2	23.5	3.39	3.05	2.86	2.69	31.681	43.259				
ERDC	E-W	2	34.7	4.91	4.46	4.17	3.92	31.882	44.772				

**TABLE 3.6 Backcalculated result of slab at location 5 without slab size correction by AREA Method.**

Test Machine	Tested Direction	Location	Load, kip	D0", mil	D12", mil	D24", mil	D36", mil	AREA	l, radius of relative stiffness	l ave,est	Kd, psi/in	Ks, psi/in	Epcc, ksi
FAA KUAB	W-E	5	12.5	1.92	1.81	1.65	1.53	32.406	49.337	49.043	336	168	5.56E+03
FAA KUAB	W-E	5	24.8	3.84	3.57	3.29	3.04	32.188	47.315				
FAA KUAB	W-E	5	37.0	5.64	5.32	4.89	4.51	32.521	50.478				
FAA KUAB	E-W	5	12.6	1.96	1.81	1.66	1.53	31.929	45.141	46.316	371	185	4.89E+03
FAA KUAB	E-W	5	24.5	3.85	3.57	3.28	3	32.026	45.933				
FAA KUAB	E-W	5	37.0	5.68	5.3	4.88	4.49	32.250	47.874				
ERDC	W-E	5	11.2	1.5	1.39	1.27	1.17	31.960	45.394	46.074	429	214	5.53E+03
ERDC	W-E	5	23.2	3.19	2.96	2.72	2.49	32.050	46.134				
ERDC	W-E	5	34.2	4.65	4.32	3.98	3.64	32.116	46.693				
ERDC	E-W	5	11.0	1.47	1.38	1.22	1.16	31.959	45.387	48.664	390	195	6.27E+03
ERDC	E-W	5	23.3	3.17	2.97	2.76	2.55	32.517	50.438				
ERDC	E-W	5	34.6	4.65	4.36	4.04	3.73	32.490	50.165				

**TABLE 3.7 Backcalculated result of slab at location 8 without slab size correction by AREA Method.**

Test Machine	Tested Direction	Location	Load, kip	D0", mil	D12", mil	D24", mil	D36", mil	AREA	l, radius of relative stiffness	l ave,est	Kd, psi/in	Ks, psi/in	Epcc, ksi
FAA KUAB	W-E	8	12.5	1.86	1.72	1.57	1.46	31.935	45.197	45.900	389	194	4.94E+03
FAA KUAB	W-E	8	24.8	3.8	3.55	3.21	2.94	31.989	45.633				
FAA KUAB	W-E	8	37.0	5.56	5.21	4.73	4.34	32.137	46.870				
FAA KUAB	E-W	8	12.6	1.9	1.75	1.6	1.46	31.768	43.902	45.029	402	201	4.73E+03
FAA KUAB	E-W	8	24.7	3.8	3.54	3.19	2.9	31.832	44.382				
FAA KUAB	E-W	8	37.0	5.58	5.22	4.76	4.34	32.129	46.804				
ERDC	W-E	8	11.2	1.48	1.33	1.21	1.1	31.054	39.156	38.065	622	311	3.74E+03
ERDC	W-E	8	23.7	3.24	2.87	2.61	2.37	30.685	37.106				
ERDC	W-E	8	34.7	4.72	4.21	3.83	3.46	30.839	37.933				
ERDC	E-W	8	11.0	1.5	1.37	1.2	1.16	31.200	40.035	39.511	563	281	3.93E+03
ERDC	E-W	8	23.3	3.28	2.92	2.68	2.46	30.988	38.770				
ERDC	E-W	8	34.5	4.8	4.29	3.96	3.62	31.150	39.729				

**TABLE 3.8 Backcalculated result of slab at location 11 without slab size correction by AREA Method.**

Test Machine	Tested Direction	Location	Load, kip	D0", mil	D12", mil	D24", mil	D36", mil	AREA	l, radius of relative stiffness	l ave,est	Kd, psi/in	Ks, psi/in	Epcc, ksi
FAA KUAB	W-E	11	12.5	1.93	1.8	1.64	1.51	32.083	46.410	45.014	394	197	4.63E+03
FAA KUAB	W-E	11	24.8	3.89	3.6	3.25	2.96	31.697	43.370				
FAA KUAB	W-E	11	37.0	5.68	5.28	4.8	4.4	31.944	45.262				
FAA KUAB	E-W	11	12.6	1.95	1.81	1.69	1.58	32.400	49.276	49.584	324	162	5.61E+03
FAA KUAB	E-W	11	24.7	3.87	3.61	3.34	3.09	32.341	48.715				
FAA KUAB	E-W	11	37.0	5.72	5.4	4.96	4.59	32.549	50.762				
ERDC	W-E	11	11.2	1.46	1.35	1.25	1.15	32.096	46.520	45.168	452	226	5.39E+03
ERDC	W-E	11	23.6	3.19	2.93	2.7	2.49	31.862	44.618				
ERDC	W-E	11	34.6	4.69	4.31	3.96	3.65	31.829	44.365				
ERDC	E-W	11	11.1	1.45	1.33	1.21	1.1	31.572	42.481	40.736	550	275	4.33E+03
ERDC	E-W	11	23.4	3.19	2.89	2.62	2.37	31.185	39.942				
ERDC	E-W	11	34.6	4.71	4.26	3.87	3.49	31.159	39.785				

**TABLE 3.9 Backcalculated result of slab at location 2 with slab size correction by AREA Method.**

Test Machine	Tested Direction	Location	Load, kip	l ave,est	Size Correction Factor			Non adjusted		Adjusted		Adjusted
					CF lk,est	CF di	lk,adjust	Kd, psi/in	Ks, psi/in	Kd, psi/in	Ks, psi/in	Epc, ksi
FAA KUAB	W-E	2	12.5	60.519	0.87059	0.79	52.69	223	111	370	185	8.16E+03
FAA KUAB	W-E	2	24.8									
FAA KUAB	W-E	2	37.0									
FAA KUAB	E-W	2	12.6	43.173	0.94308	0.88	40.72	436	218	557	279	4.39E+03
FAA KUAB	E-W	2	24.6									
FAA KUAB	E-W	2	37.0									
ERDC	W-E	2	11.2	38.140	0.96116	0.90	36.66	581	291	695	348	3.60E+03
ERDC	W-E	2	23.7									
ERDC	W-E	2	34.7									
ERDC	E-W	2	11.1	43.359	0.94237	0.88	40.86	457	228	585	293	4.67E+03
ERDC	E-W	2	23.5									
ERDC	E-W	2	34.7									

**TABLE 3.10 Backcalculated result of slab at location 5 with slab size correction by AREA Method.**

Test Machine	Tested Direction	Location	Load, kip	l ave,est	Size Correction Factor			Non adjusted		Adjusted		Adjusted
					CF lk,est	CF di	lk,adjust	Kd, psi/in	Ks, psi/in	Kd, psi/in	Ks, psi/in	Epc, ksi
FAA KUAB	W-E	5	12.5	49.043	0.91966	0.85	45.10	336	168	467	233	5.53E+03
FAA KUAB	W-E	5	24.8									
FAA KUAB	W-E	5	37.0									
FAA KUAB	E-W	5	12.6	46.316	0.93078	0.86	43.11	371	185	496	248	4.90E+03
FAA KUAB	E-W	5	24.5									
FAA KUAB	E-W	5	37.0									
ERDC	W-E	5	11.2	46.074	0.93175	0.86	42.93	429	214	571	285	5.55E+03
ERDC	W-E	5	23.2									
ERDC	W-E	5	34.2									
ERDC	E-W	5	11.0	48.664	0.92123	0.85	44.83	390	195	540	270	6.24E+03
ERDC	E-W	5	23.3									
ERDC	E-W	5	34.6									

**TABLE 3.11 Backcalculated result of slab at location 8 with slab size correction by AREA Method.**

Test Machine	Tested Direction	Location	Load, kip	l ave,est	Size Correction Factor			Non adjusted		Adjusted		Adjusted
					CF lk,est	CF di	lk,adjust	Kd, psi/in	Ks, psi/in	Kd, psi/in	Ks, psi/in	Epcc, ksi
FAA KUAB	W-E	8	12.5	45.900	0.93244	0.87	42.80	389	194	517	258	4.96E+03
FAA KUAB	W-E	8	24.8									
FAA KUAB	W-E	8	37.0									
FAA KUAB	E-W	8	12.6	45.029	0.93589	0.87	42.14	402	201	528	264	4.77E+03
FAA KUAB	E-W	8	24.7									
FAA KUAB	E-W	8	37.0									
ERDC	W-E	8	11.2	38.065	0.96141	0.91	36.60	622	311	743	372	3.82E+03
ERDC	W-E	8	23.7									
ERDC	W-E	8	34.7									
ERDC	E-W	8	11.0	39.511	0.95647	0.90	37.79	563	281	685	342	4.00E+03
ERDC	E-W	8	23.3									
ERDC	E-W	8	34.5									

**TABLE 3.12 Backcalculated result of slab at location 11 with slab size correction by AREA Method.**

Test Machine	Tested Direction	Location	Load, kip	l ave,est	Size Correction Factor			Non adjusted		Adjusted		Adjusted
					CF lk,est	CF di	lk,adjust	Kd, psi/in	Ks, psi/in	Kd, psi/in	Ks, psi/in	Epcc, ksi
FAA KUAB	W-E	11	12.5	45.014	0.93595	0.87	42.13	394	197	516	258	4.66E+03
FAA KUAB	W-E	11	24.8									
FAA KUAB	W-E	11	37.0									
FAA KUAB	E-W	11	12.6	49.584	0.91742	0.85	45.49	324	162	455	227	5.57E+03
FAA KUAB	E-W	11	24.7									
FAA KUAB	E-W	11	37.0									
ERDC	W-E	11	11.2	45.168	0.93534	0.87	42.25	452	226	594	297	5.42E+03
ERDC	W-E	11	23.6									
ERDC	W-E	11	34.6									
ERDC	E-W	11	11.1	40.736	0.95212	0.89	38.79	550	275	680	340	4.41E+03
ERDC	E-W	11	23.4									
ERDC	E-W	11	34.6									



**TABLE 3.13 Backcalculated result of slab at location 2 without slab size correction by NUS-BACK.**

Measured data				dm3/dm1				dm4/dm2				Average Kd, psi/ in.	Average Ks, psi/in.	l,radius of relative stiffness, m	l,radius of relative stiffness, in.	Epcc, ksi
Test	Direction	Location	Load (kip)	Ave D24"/ D0"	l,radius of relative stiffness, m	Fk,r1	K,ave	Ave D36"/D 12"	l,radius of relative stiffness, m	Fk,r4	K,ave					
FAA KUAB	W-E	2	12.5	0.898	1.518	0.003	205	0.909	2.199	0.003	223	214	107	1.859	73.173	1.75E+04
FAA KUAB	W-E	2	24.8													
FAA KUAB	W-E	2	37.0													
FAA KUAB	E-W	2	12.6	0.835	1.036	0.009	531	0.819	1.307	0.004	325	428	214	1.171	46.121	5.54E+03
FAA KUAB	E-W	2	24.6													
FAA KUAB	E-W	2	37.0													
ERDC	W-E	2	11.2	0.816	0.959	0.010	621	0.825	1.338	0.004	344	482	241	1.148	45.216	5.77E+03
ERDC	W-E	2	23.7													
ERDC	W-E	2	34.7													
ERDC	E-W	2	11.1	0.843	1.079	0.008	535	0.876	1.754	0.003	247	391	195	1.416	55.763	1.08E+04
ERDC	E-W	2	23.5													
ERDC	E-W	2	34.7													

**TABLE 3.14 Backcalculated result of slab at location 5 without slab size correction by NUS-BACK.**

Measured data				dm3/dm1				dm4/dm2				Average Kd, psi/ in.	Average Ks, psi/in.	l,radius of relative stiffness, m	l,radius of relative stiffness, in.	Epcc, ksi
Test	Direction	Location	Load (kip)	Ave D24"/ D0"	l,radius of relative stiffness, m	Fk,r1	K,ave	Ave D36"/D 12"	l,radius of relative stiffness, m	Fk,r4	K,ave					
FAA KUAB	W-E	5	12.5	0.861	1.187	0.007	424	0.848	1.495	0.003	259	342	171	1.341	52.793	7.61E+03
FAA KUAB	W-E	5	24.8													
FAA KUAB	W-E	5	37.0													
FAA KUAB	E-W	5	12.6	0.853	1.133	0.008	456	0.844	1.465	0.004	266	361	181	1.299	51.149	7.08E+03
FAA KUAB	E-W	5	24.5													
FAA KUAB	E-W	5	37.0													
ERDC	W-E	5	11.2	0.852	1.128	0.008	526	0.842	1.448	0.004	310	418	209	1.288	50.692	7.91E+03
ERDC	W-E	5	23.2													
ERDC	W-E	5	34.2													
ERDC	E-W	5	11.0	0.856	1.157	0.008	507	0.852	1.522	0.003	289	398	199	1.339	52.723	8.81E+03
ERDC	E-W	5	23.3													
ERDC	E-W	5	34.6													

**TABLE 3.15 Backcalculated result of slab at location 8 without slab size correction by NUS-BACK.**

Measured data				dm3/dm1				dm4/dm2				Average Kd, psi/ in.	Average Ks, psi/in.	l,radius of relative stiffness, m	l,radius of relative stiffness, in.	Epcc, ksi
Test	Direction	Location	Load (kip)	Ave D24"/ D0"	l,radius of relative stiffness, m	Fk,r1	K,ave	Ave D36"/D 12"	l,radius of relative stiffness, m	Fk,r4	K,ave					
FAA KUAB	W-E	8	12.5	0.847	1.097	0.008	495	0.837	1.412	0.004	288	391	196	1.255	49.393	6.67E+03
FAA KUAB	W-E	8	24.8													
FAA KUAB	W-E	8	37.0													
FAA KUAB	E-W	8	12.6	0.845	1.088	0.008	498	0.828	1.358	0.004	305	401	201	1.223	48.166	6.19E+03
FAA KUAB	E-W	8	24.7													
FAA KUAB	E-W	8	37.0													
ERDC	W-E	8	11.2	0.812	0.945	0.010	676	0.825	1.338	0.004	365	521	260	1.141	44.934	6.08E+03
ERDC	W-E	8	23.7													
ERDC	W-E	8	34.7													
ERDC	E-W	8	11.0	0.814	0.953	0.010	650	0.844	1.466	0.004	308	479	240	1.209	47.615	7.05E+03
ERDC	E-W	8	23.3													
ERDC	E-W	8	34.5													

**TABLE 3.16 Backcalculated result of slab at location 11 without slab size correction by NUS-BACK.**

Measured data				dm3/dm1				dm4/dm2				Average Kd, psi/ in.	Average Ks, psi/in.	l,radius of relative stiffness, m	l,radius of relative stiffness, in.	Epcc, ksi
Test	Direction	Location	Load (kip)	Ave D24"/ D0"	l,radius of relative stiffness, m	Fk,r1	K,ave	Ave D36"/D 12"	l,radius of relative stiffness, m	Fk,r4	K,ave					
FAA KUAB	W-E	11	12.5	0.843	1.081	0.008	492	0.831	1.378	0.004	292	392	196	1.229	48.399	6.16E+03
FAA KUAB	W-E	11	24.8													
FAA KUAB	W-E	11	37.0													
FAA KUAB	E-W	11	12.6	0.866	1.219	0.007	398	0.860	1.590	0.003	239	318	159	1.405	55.303	8.53E+03
FAA KUAB	E-W	11	24.7													
FAA KUAB	E-W	11	37.0													
ERDC	W-E	11	11.2	0.849	1.111	0.008	547	0.850	1.505	0.003	301	424	212	1.308	51.508	8.55E+03
ERDC	W-E	11	23.6													
ERDC	W-E	11	34.6													
ERDC	E-W	11	11.1	0.826	0.998	0.009	632	0.822	1.322	0.004	367	500	250	1.160	45.678	6.23E+03
ERDC	E-W	11	23.4													
ERDC	E-W	11	34.6													

**TABLE 3.17** Backcalculated result of slab at location 2 with slab size correction by NUS-BACK.

Measured data				Average Ks, psi/in.	I,radius of relative stiffness, in.	Epcc, ksi	CF lk,est	CF di	lk,adjust	Ks,adj	Adjusted Epcc, ksi
Test	Direction	Location	Load (kip)								
FAA KUAB	W-E	2	12.5	107	73.173	1.75E+04	0.81657	0.73772	59.750	217	1.59E+04
FAA KUAB	W-E	2	24.8								
FAA KUAB	W-E	2	37.0								
FAA KUAB	E-W	2	12.6	214	46.121	5.54E+03	0.93156	0.86471	42.965	285	5.56E+03
FAA KUAB	E-W	2	24.6								
FAA KUAB	E-W	2	37.0								
ERDC	W-E	2	11.2	241	45.216	5.77E+03	0.93515	0.86927	42.284	317	5.81E+03
ERDC	W-E	2	23.7								
ERDC	W-E	2	34.7								
ERDC	E-W	2	11.1	195	55.763	1.08E+04	0.89117	0.81698	49.694	301	1.05E+04
ERDC	E-W	2	23.5								
ERDC	E-W	2	34.7								

**TABLE 3.18 Backcalculated result of slab at location 5 with slab size correction by NUS-BACK.**

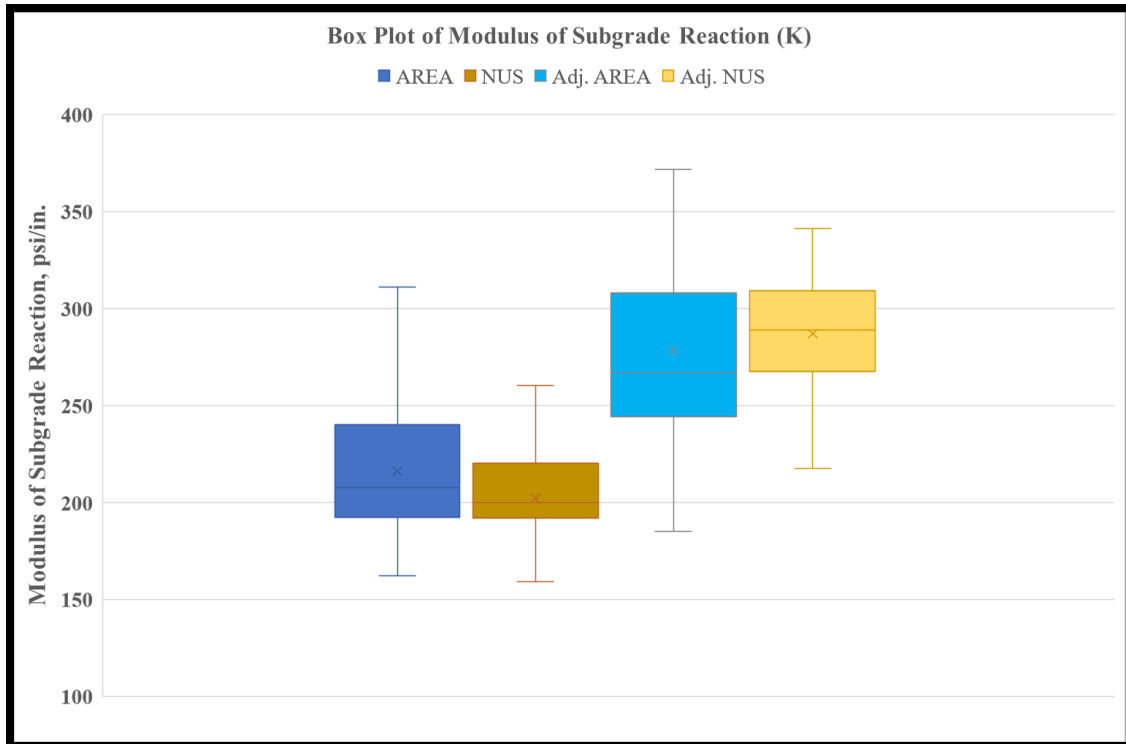
Measured data				Average Ks, psi/in.	Lradius of relative stiffness, in.	Eecc, ksi	CF lk,est	CF di	lk,adjust	Ks,adj	Adjusted Eecc, ksi
Test	Direction	Location	Load (kip)								
FAA KUAB	W-E	5	12.5	171	52.793	7.61E+03	0.9039	0.83147	47.720	252	7.47E+03
FAA KUAB	W-E	5	24.8								
FAA KUAB	W-E	5	37.0								
FAA KUAB	E-W	5	12.6	181	51.149	7.08E+03	0.91086	0.83958	46.590	259	7.00E+03
FAA KUAB	E-W	5	24.5								
FAA KUAB	E-W	5	37.0								
ERDC	W-E	5	11.2	209	50.692	7.91E+03	0.91279	0.84185	46.271	298	7.83E+03
ERDC	W-E	5	23.2								
ERDC	W-E	5	34.2								
ERDC	E-W	5	11.0	199	52.723	8.81E+03	0.9042	0.83181	47.672	293	8.66E+03
ERDC	E-W	5	23.3								
ERDC	E-W	5	34.6								

**TABLE 3.19** Backcalculated result of slab at location 8 with slab size correction by NUS-BACK.

Measured data				Average Ks, psi/in.	Lradius of relative stiffness, in.	Eecc, ksi	CF lk,est	CF di	lk,adjust	Ks,adj	Adjusted Eecc, ksi
Test	Direction	Location	Load (kip)								
FAA KUAB	W-E	8	12.5	196	49.393	6.67E+03	0.91821	0.84831	45.353	274	6.63E+03
FAA KUAB	W-E	8	24.8								
FAA KUAB	W-E	8	37.0								
FAA KUAB	E-W	8	12.6	201	48.166	6.19E+03	0.92328	0.85445	44.470	275	6.17E+03
FAA KUAB	E-W	8	24.7								
FAA KUAB	E-W	8	37.0								
ERDC	W-E	8	11.2	260	44.934	6.08E+03	0.93626	0.87069	42.070	341	6.12E+03
ERDC	W-E	8	23.7								
ERDC	W-E	8	34.7								
ERDC	E-W	8	11.0	240	47.615	7.05E+03	0.92553	0.85721	44.069	326	7.05E+03
ERDC	E-W	8	23.3								
ERDC	E-W	8	34.5								

**TABLE 3.20 Backcalculated result of slab at location 11 with slab size correction by NUS-BACK.**

Measured data				Average Ks, psi/in.	L, radius of relative stiffness, in.	E <sub>pcc</sub> , ksi	CF I <sub>k,est</sub>	CF d <sub>i</sub>	I <sub>k,adjust</sub>	K <sub>s,adj</sub>	Adjusted E <sub>pcc</sub> , ksi
Test	Direction	Location	Load (kip)								
FAA KUAB	W-E	11	12.5	196	48.399	6.16E+03	0.92232	0.85328	44.639	270	6.14E+03
FAA KUAB	W-E	11	24.8								
FAA KUAB	W-E	11	37.0								
FAA KUAB	E-W	11	12.6	159	55.303	8.53E+03	0.89315	0.81921	49.394	244	8.30E+03
FAA KUAB	E-W	11	24.7								
FAA KUAB	E-W	11	37.0								
ERDC	W-E	11	11.2	212	51.508	8.55E+03	0.90935	0.83781	46.839	306	8.44E+03
ERDC	W-E	11	23.6								
ERDC	W-E	11	34.6								
ERDC	E-W	11	11.1	250	45.678	6.23E+03	0.93333	0.86694	42.633	331	6.26E+03
ERDC	E-W	11	23.4								
ERDC	E-W	11	34.6								

**FIGURE 3.16 Relationship between modulus of subgrade reaction calculated by AREA Method and NUS-BACK Solution with and without slab size correction factor.**

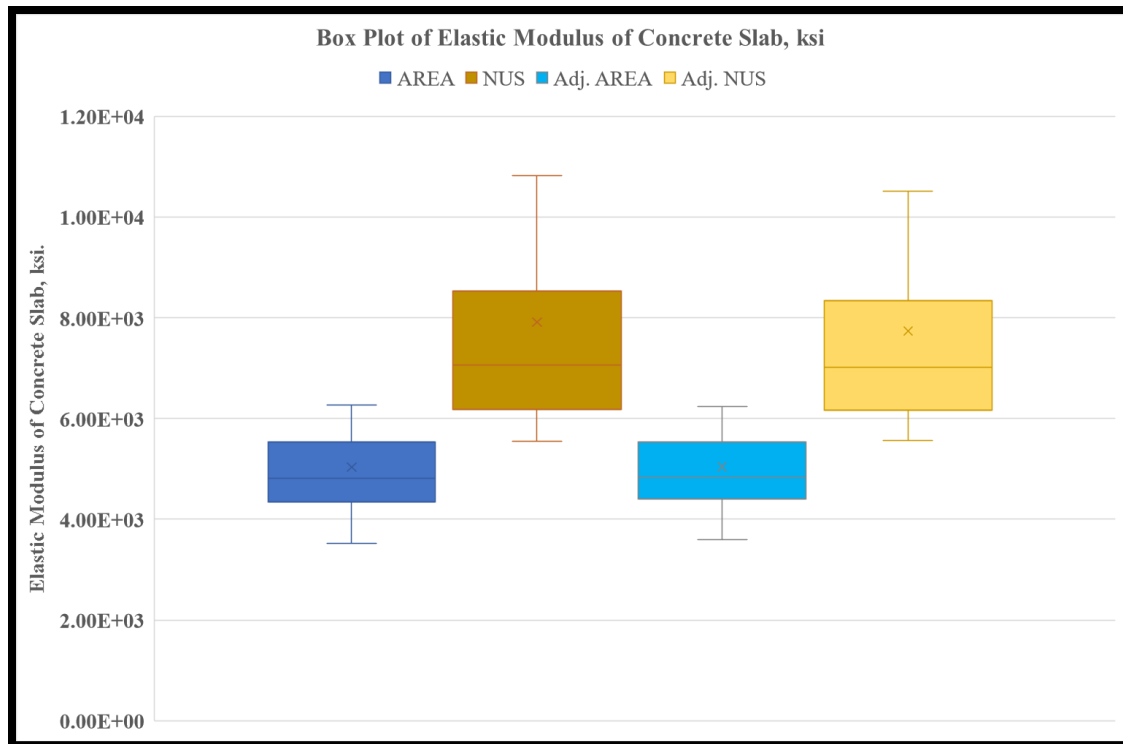


**FIGURE 3.17 Relationship between elastic modulus of concrete slab calculated by AREA Method and NUS-BACK Solution with and without slab size correction factor.**

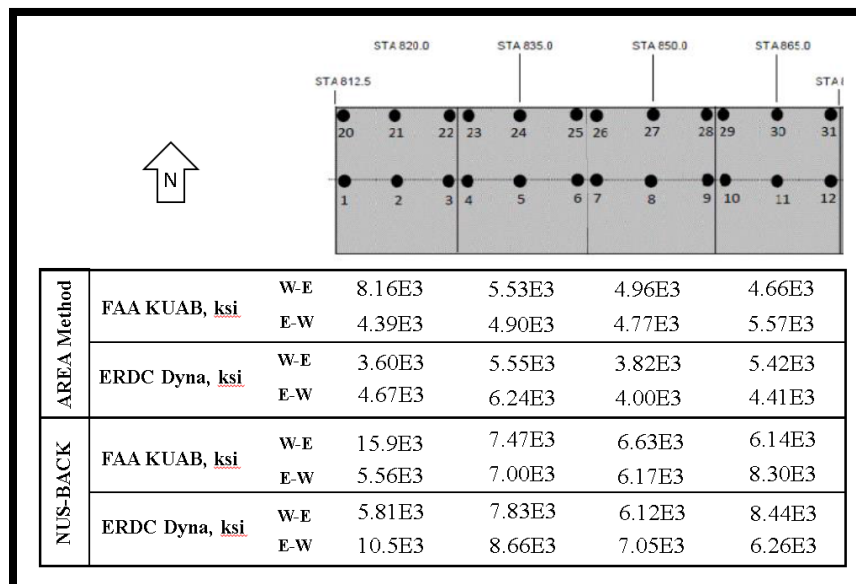


**FIGURE 3.18 Backcalculated modulus on different slabs.**

**TABLE 3.21 Comparison of back-calculated results and lab test results.**

Layer Modulus	Plate Loading Test, pci	Lab test result			AREA Method			Nus-Back Method		
		Strength, psi	Elastic Modulus, ksi	k, pci	Elastic Modulus, ksi	k, pci	St. dev.	Elastic Modulus, psi	k, pci	St. dev.
Concrete P501	-	$F_f = 707$ (Flexural strength)	5.03E+03	-	5.04E+03	-	1.06E+03	7.74E+03	-	2.45E+03
Econocrete P306	-	$F_c' = 525$ (Compressive strength)	1.31E+03	-	-	278	50	-	287	33
Subgrade	111	-	8.21	108	-			-		

### 3.5 Overlay Design of FAARFIELD

#### 3.5.1 Input Conditions

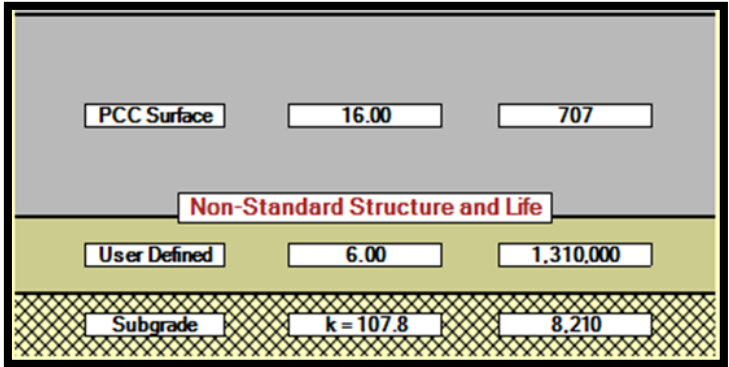
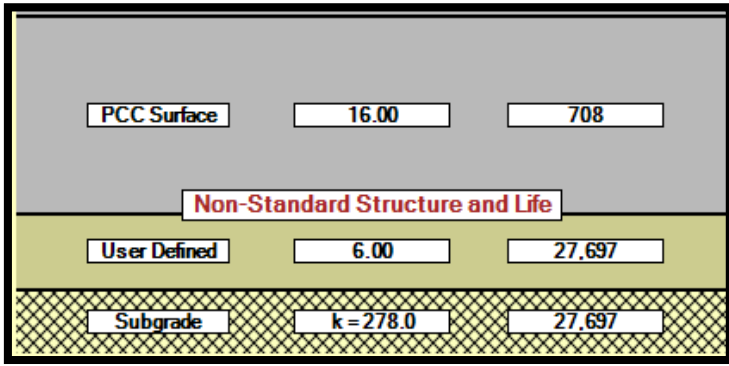
In this section, the pavement layer moduli obtained by the lab test results and the two back-calculation methods-the AREA method and NUS-BACK were applied to the design of overlay in FAARFIELD. The influences of the backcalculated moduli from different pavement evaluation methods on the designed overlay thickness were analyzed in this part.

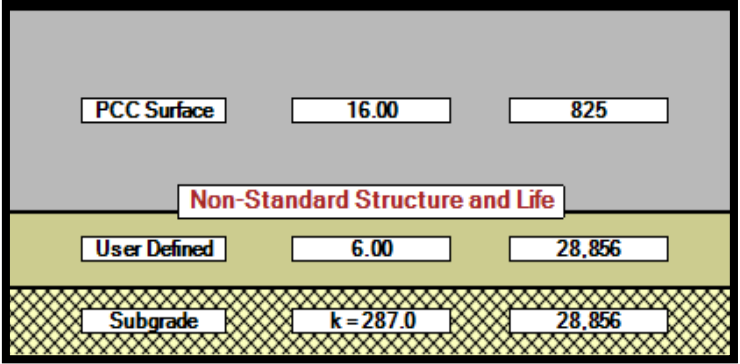
In the analysis, the conditions of the existing pavement were assigned with the SCI and CDFU that varied from 70 to 100 percent while the design life of the pavement was ranged from 15 to 30 years. The traffic departure of the JFK international airport was selected as the traffic input of this analysis as shown in Table 3.22. The thicknesses and moduli or flexural strength of existing layers used in FAARFIELD on the different cases-lab test, the AREA method, and the NUS-BACK- were shown in Table 3.23.

**TABLE 3.22 Traffic input used in FAARFIELD**

Airplane Name	Annual Departures
A380	4302
B777-300ER	4038
A320-200	44942
A300-600	3708
A340-300	2779
A330-200	1780
A340-500	1082
B767-300ER	20650
B747-400	6874
B737-800	2451
B787-9	350
B737-900ER	136

**Table 3.23 Inputs of layers used in FAARFIELD.**

Evaluation Method	Layer type / Layer thickness (in.) / Modulus or Fr, (psi)
Lab Test	
AREA Method	

<b>NUS-BACK</b>	
-----------------	--

### 3.5.2 Overlay Design Results

The overlays in this analysis included HMA overlay on the rigid pavement and fully unbonded PCC overlay on the rigid pavement. The comparisons of the HMA overlay and the unbonded PCC overlay from different back-calculation methods were illustrated from Figure 3.19 to 3.22, which some apparent relationship between the inputs and the outputs of FAARFIELD could be recognized as follows.

First, the HMA overlay thickness calculated by the layer moduli from lab test method was the greatest followed by AREA method and NUS-BACK. Moreover, in most cases, the HMA overlay thickness for the input of NUS-BACK data was the minimum thickness allowed by the FAARFIELD while the HMA overlay thickness was in the middle between the lab test and the NUS-BACK.

Second, it seemed to me that the pavement structure provided by the NUS-BACK method was significantly stronger than the others, which the layer moduli might be overestimated compared to the actual properties. Moreover, the expected structural life of the NUS-BACK was noticeably greater than the design life and increased as the structural condition of the existing pavement increased, while the expected structural life of the lab test and the AREA method were fitted well with the design life.



Third, the HMA overlay thickness from all cases gradually decreased when the structural condition index (SCI) increased or when the cumulative damage factor used (CDFU) decreased as shown from Figure 3.19 to 3.20

Fourth, from SCI ranging from 70 to 80 percent, the PCC overlay thicknesses of the AREA method and NUS-BACK were almost identical, but as the structural condition index of the pavement became greater than 90 percent, the overlay thicknesses of the AREA method and NUS-BACK were then separated (Figure 3.21).

Fifth, the minimum overlay thicknesses for the HMA overlay and PCC overlay were 2 inches and 5 inches, respectively. Which this condition mostly occurred when the calculated life was greater than the required design life as shown in Figure 3.23.

Sixth, in some case of the unbonded concrete overlay, the design output could not be archived because the design output could not converge under several iterations as shown in Figure 3.24.

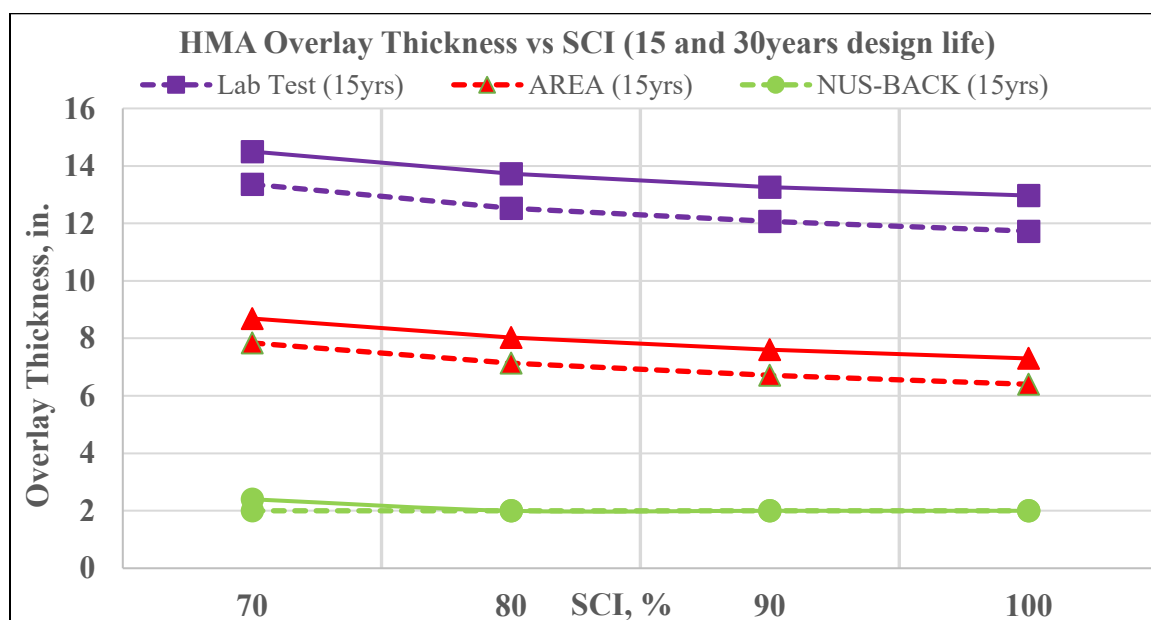


Figure 3.19 Relationship between HMA overlay thickness and SCI.

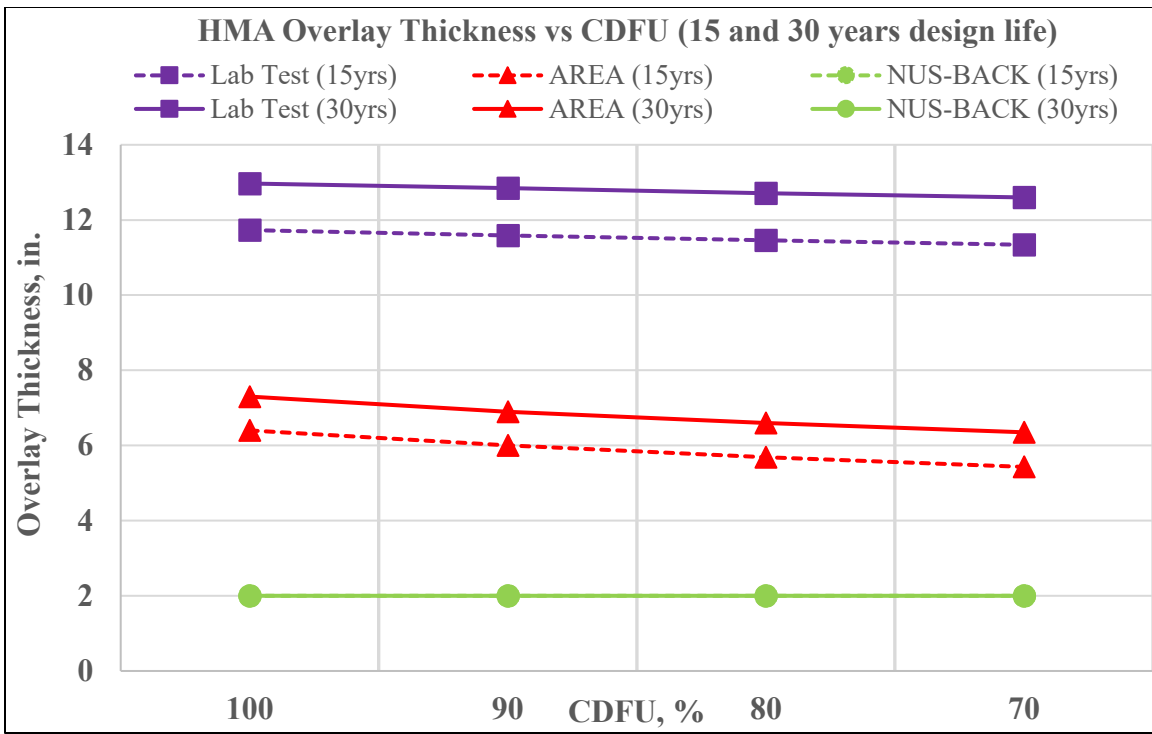


Figure 3.20 Relationship between HMA overlay thickness and CDFU.

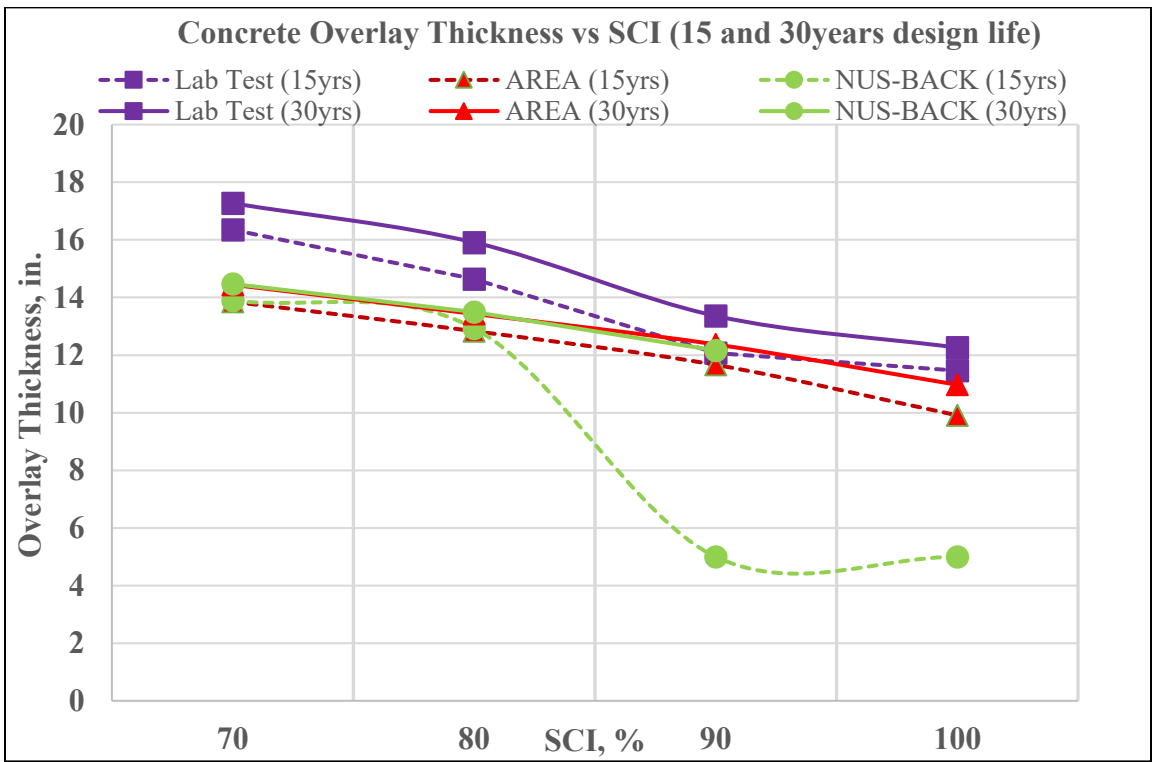


Figure 3.21 Relationship between PCC overlay output and SCI.

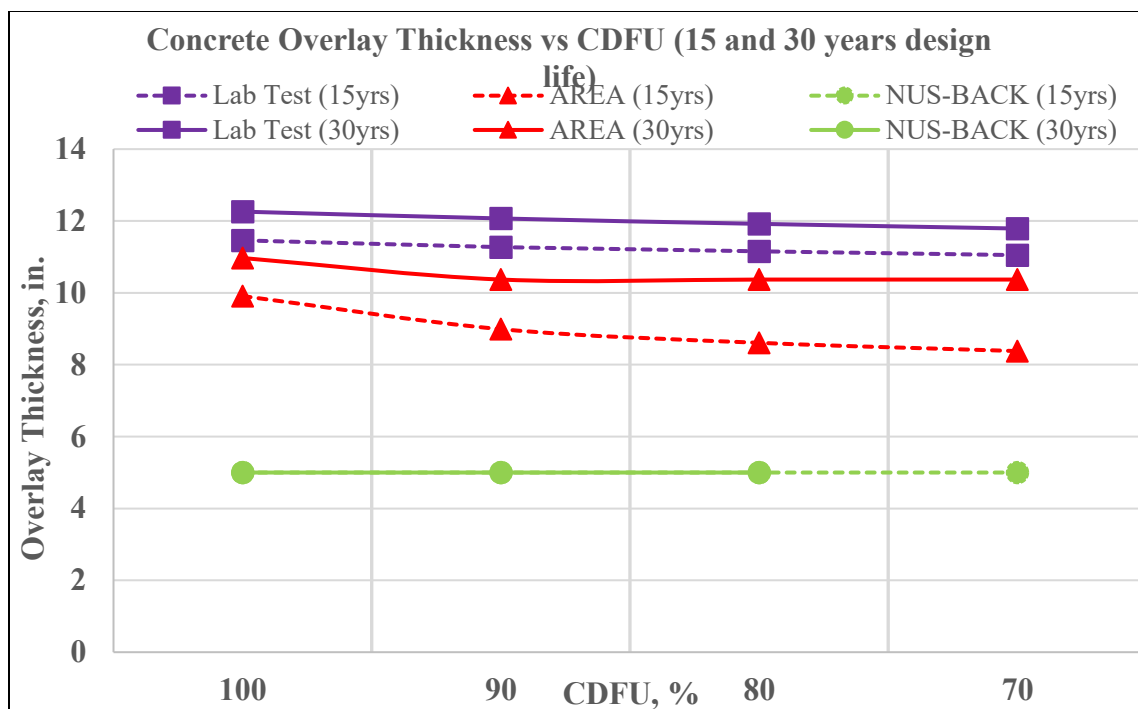


Figure 3.22 Relationship between PCC overlay output and CDFU.

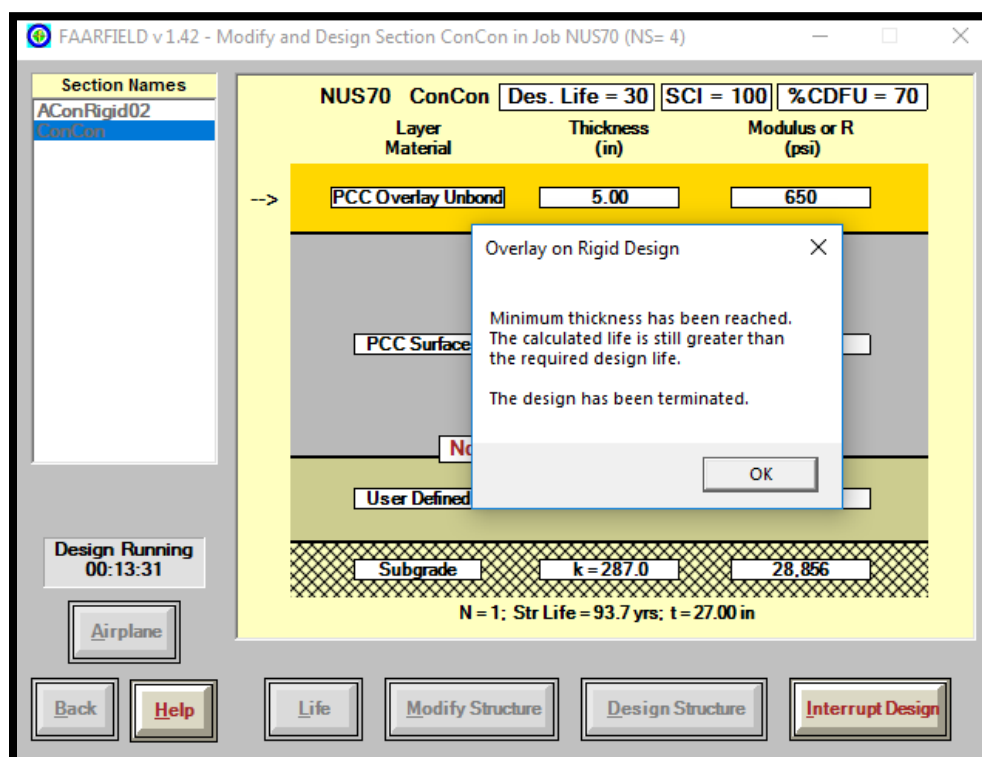


Figure 3.23 FAARFIELD output when minimum thickness has been reached.

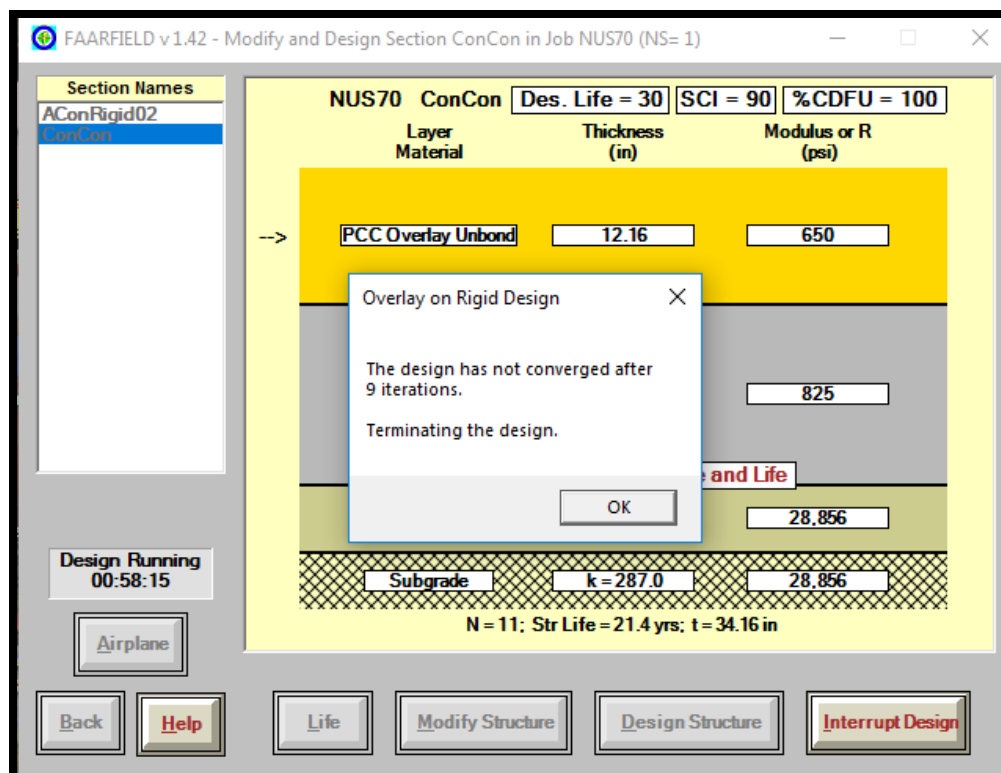


Figure 3.24 FAARFIELD output when design was terminated.

## **CHAPTER 4**

### **JOINT LOAD TRANSFER ANALYSIS OF AIRFIELD RIGID PAVEMENT**

#### **4.1 Finite Element Modeling of Joint Load Transfer Efficiency**

##### **4.1.1 Finite Element Model Details**

In this section, the researcher evaluated the stress-based LTE calculated by the critical tensile stresses obtained from the FEAFAA software using the following parameters as the input to the FEAFAA software.

- The back-calculated elastic modulus of concrete slab from the FAA's HWD database by the AREA method.
- Slab thickness ranging from 8 to 16 inches.
- 6 inches of Econocrete (P306) was used as the subbase1.
- 56 inches of Dupont clay with 5.65 mean CBR was used as the subbase2.
- A high strength subgrade modulus was assumed to 50 ksi.
- Temperature gradient ranging from -4 to 2 °F per inch.
- Different types of landing gears include dual wheel and dual tandem.
- Wheel configurations and dimensions of the input aircraft follow the library airplanes in FEAFAA.
  - Dual Whl-200
  - Dual Tan-200
- 200 kips as the gross weight of 95% gross weight on main gears
- Slab size of 15 ft. x 15 ft.
- Two moving directions, X-X and Y-Y.
- 58000 psi (400MPa) for the equivalent joint stiffness.
- 1.25 in. of dowel bar diameter at 15 in. spacing and 0.625 in. joint opening.

- Dimensions of the landing gear and the evaluated critical locations of the dual wheel and dual tandem were shown from Figure 4.1 to 4.2.
- Landing gear layouts on the single slab and multiple slab analysis of edge and corner loading were shown from Figure 4.3 to 4.6.

Equivalent joint stiffness is the effectiveness of a joint in transferring the applied wheel load depends on joint properties such as modulus of dowel support, embedded length of dowel, spacing of dowel, joint opening, etc., which could be expressed as shown in equation 4.1 (Wadkar, 2010). Khazanovich and Gotlif (2003) have recommended a range of doweled joint stiffness from 400 MPa to 1000 Mpa.

$$k_q = \frac{1}{s \left( \frac{w}{0.9G_d A_d} + \frac{w^3}{12E_d I_d} + \frac{2+\beta w}{2\beta^3 E_d I_d} \right)} \dots\dots\dots \text{Eq. 4.1}$$

$$\text{Where, } \beta = \sqrt[4]{Kd/(4E_d I_d)}$$

w	=	joint opening in inches
G <sub>d</sub>	=	dowel bar shear modulus in psi
A <sub>d</sub>	=	cross-sectional area of dowel bar in inch <sup>2</sup>
E <sub>d</sub>	=	Young's modulus in psi
I <sub>d</sub>	=	moment of inertia in inch <sup>4</sup>
K	=	modulus of dowel bar support for the concrete matrix in pci
D	=	diameter of dowel in inches

Four screenshots of FEAFAA have illustrated the procedure of using FEAFAA including Airplane Selection Window, Pavement Structure Window, Joint Modeling Window, and Mesh Generation Window as seen in Figure 4.7 to 4.10.

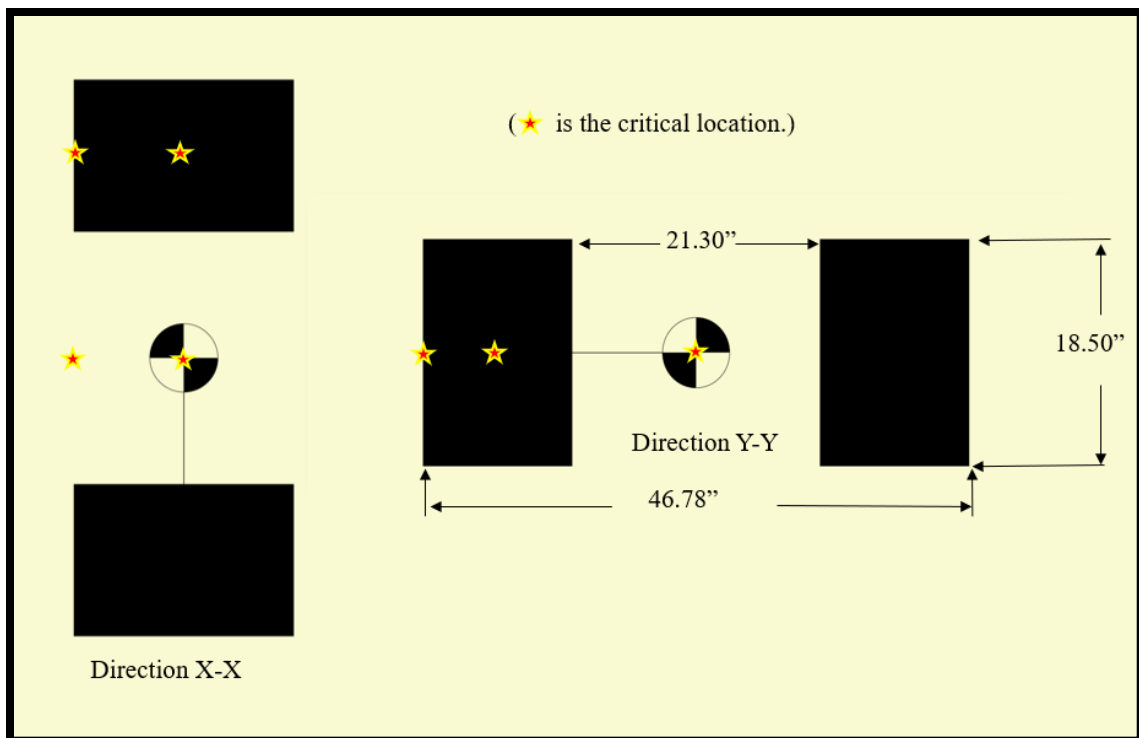


**FIGURE 4.1 Dimensions of dual wheel landing gear and evaluated critical locations.**

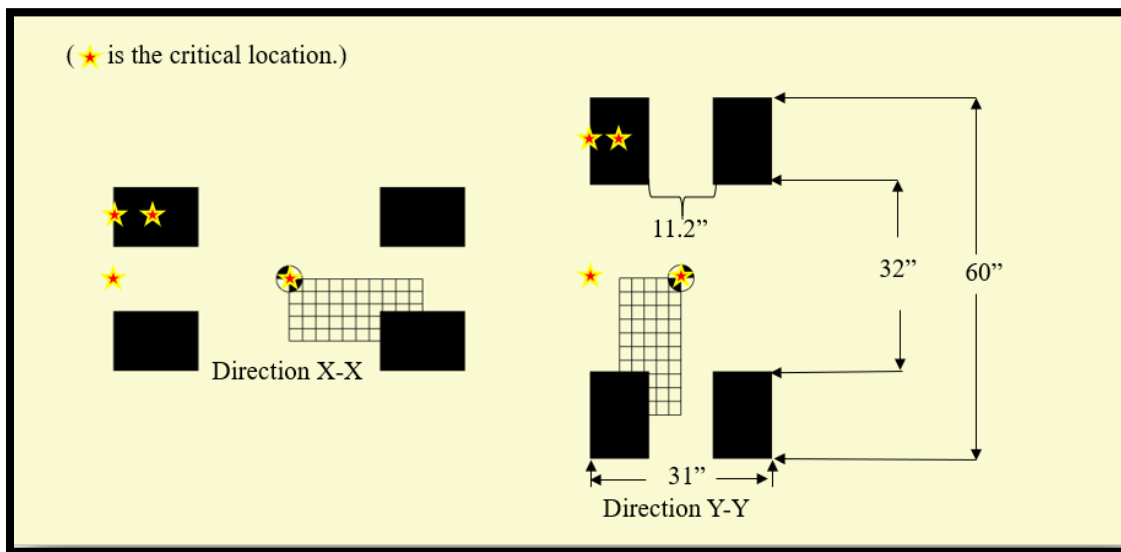


**FIGURE 4.2 Dimensions of dual tandem wheel landing gear and evaluated critical locations.**

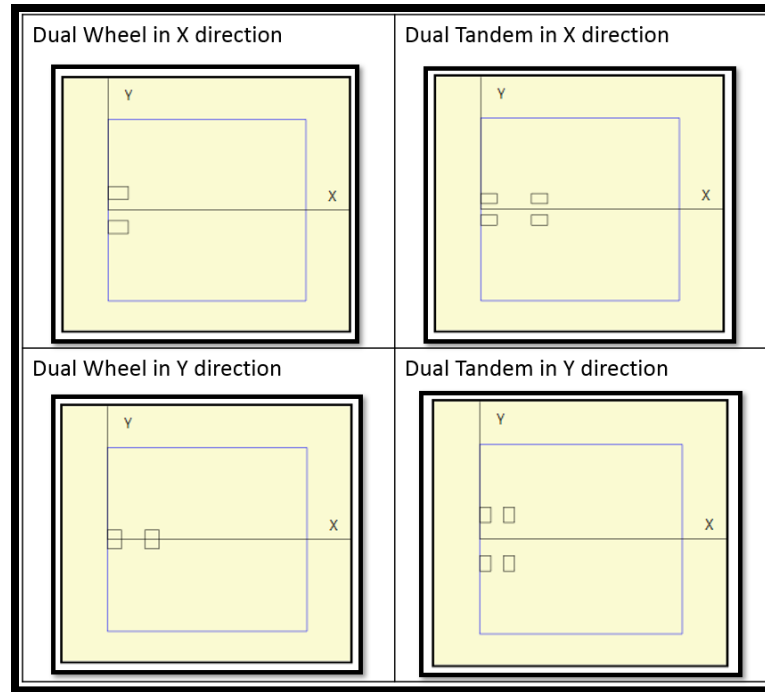


**FIGURE 4.3** Landing gear layouts of edge loading in single slab analysis.

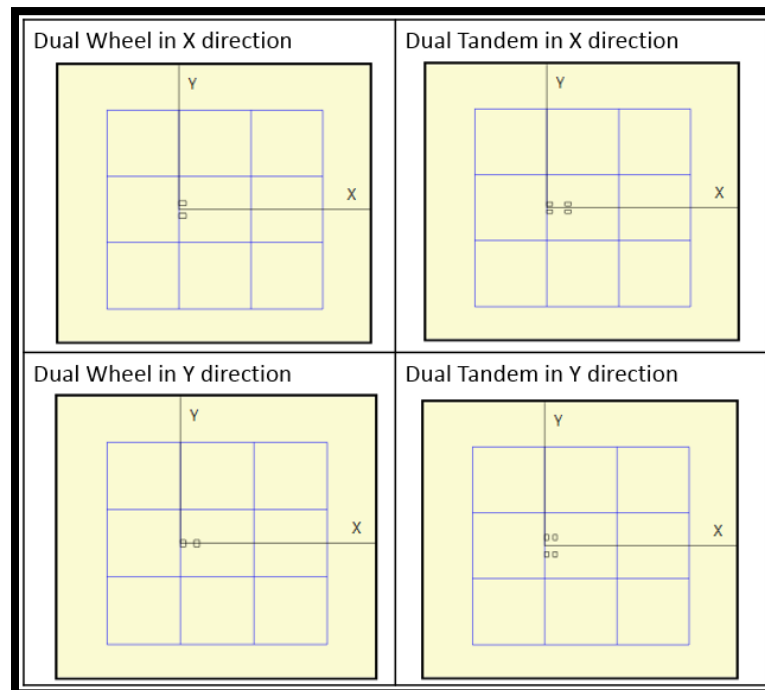


**FIGURE 4.4** Landing gear layouts of edge loading in multiple slabs analysis.



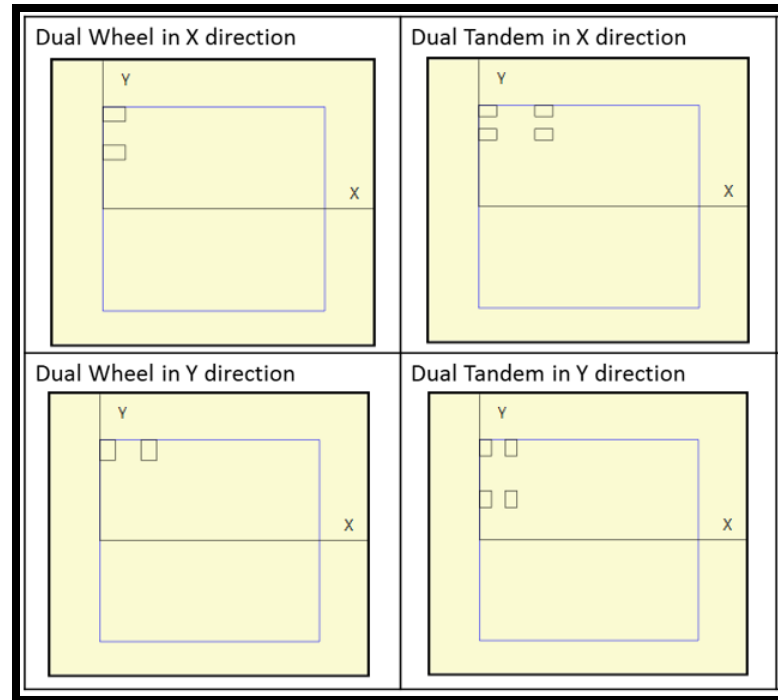


**FIGURE 4.5 Landing gear layouts of corner loading in single slab analysis.**

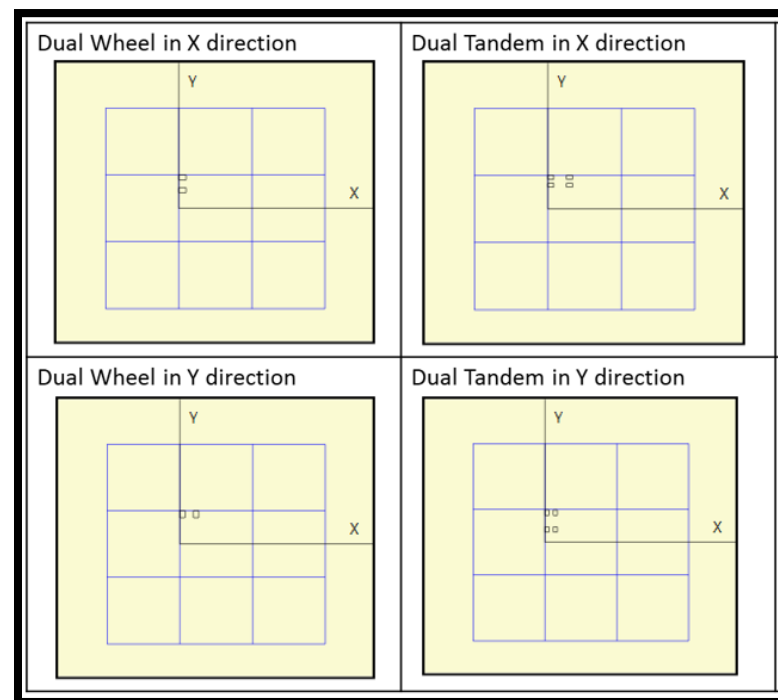


**FIGURE 4.6 Landing gear layouts of corner loading in multiple slabs analysis.**

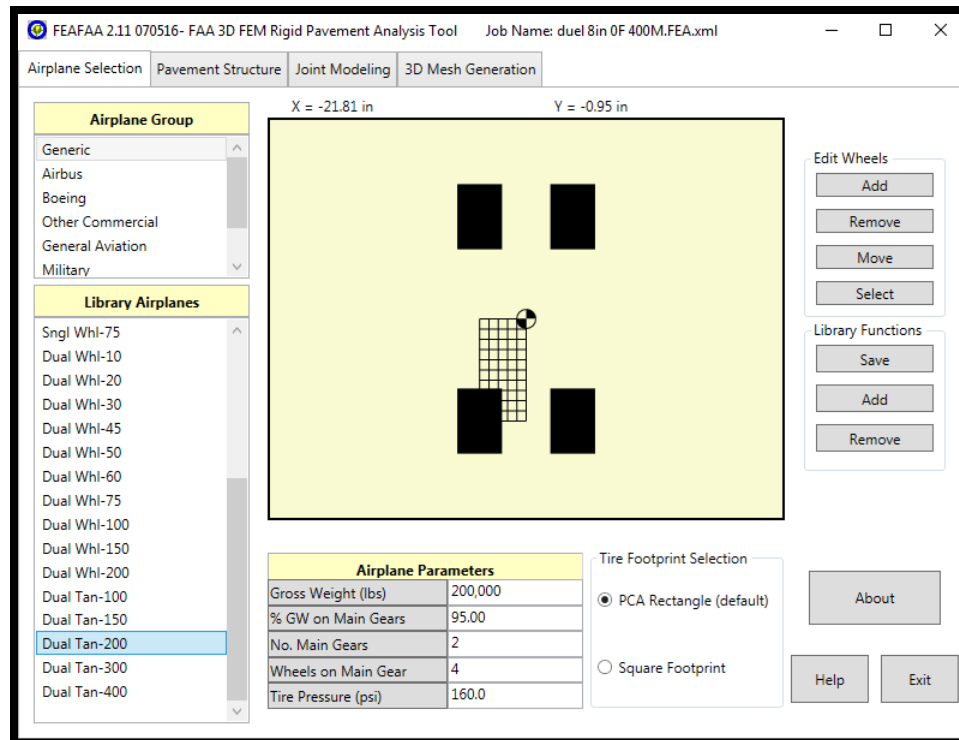


FIGURE 4.7 Airplane selection window interface of FEAFaa.

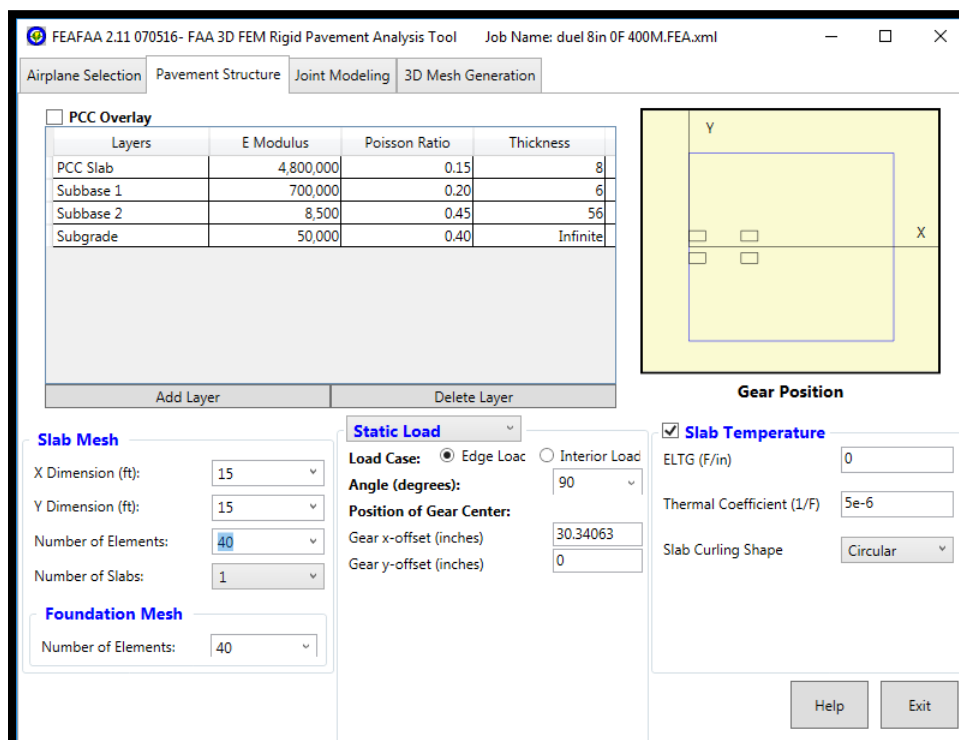


FIGURE 4.8 Pavement structure window interface of FEAFaa.

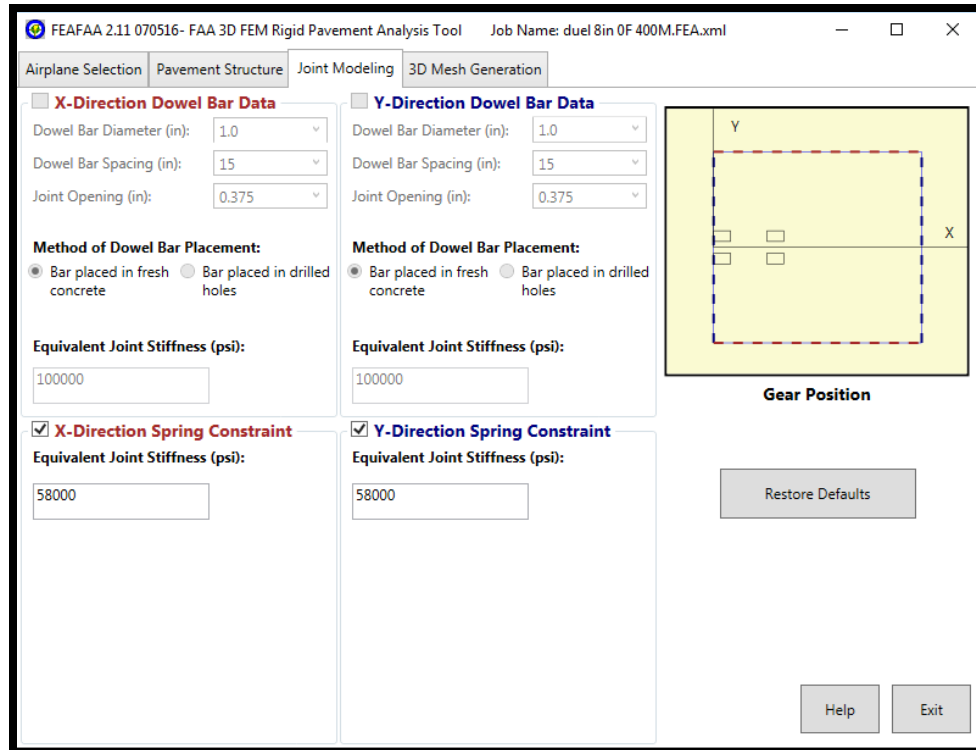


FIGURE 4.9 Joint modeling window interface of FEAFAA.

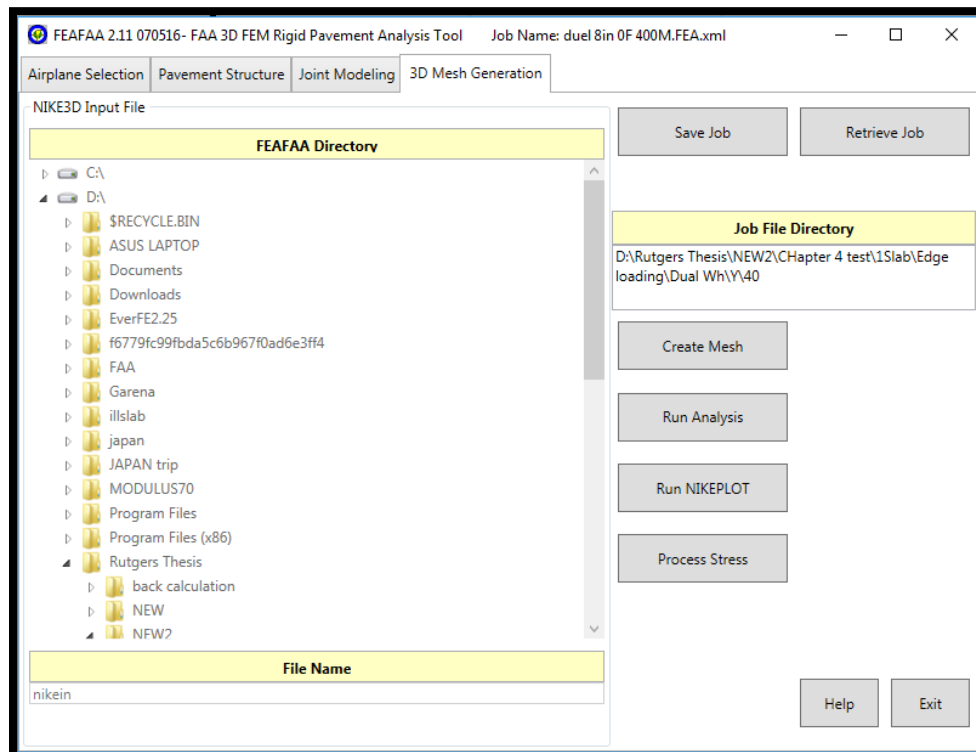


FIGURE 4.10 3D Mesh Generation window interface of FEAFAA.

## 4.2 Mesh Sensitivity Analysis and Critical Stress Locations

Under this topic mesh analysis was aimed so as to determine the applicable number of meshes for the finite element models used in FEAFAA. The 8-inch slab without temperature gradient was used in the mesh analysis regarding the tensile stress at the bottom and surface of the slab. Three different meshes (30, 40, and 50) were used in each side of the slab. The results of mesh analysis at four different stress locations of the tensile stress at the bottom of the slab under various loading conditions were obviously presented in Table 4.1. In the code designation of Dx-x-x, the numbers “x” following by “D” meant the slab thickness-, the temperature gradient, and the number of slabs in the system respectively. In relation to dual and dual tandem wheels loaded at slab edges, the critical tensile stresses at the bottom of the slab were located under the center area of the tire nearest to the joint.

Under each aircraft loading condition, the tensile stress outputs converged to stable values as the number of meshes inferred that the input of 40 meshes per one direction of the analysis closely matched to the higher input of meshes per one direction of the analysis in FEAFAA. Moreover, it was found that the 40-meshes analysis practically consumed just about half of analysis time for which the 50-meshes analysis required.

Furthermore, as shown in Table 4.2, the relationships between the tensile stress along the diagonal path on the surface of slab due to corner loading and the number of analyzed meshes under various types of landing gear configuration were provided. The results revealed that the output stresses were close to the results from the higher input of meshes per one direction when the analyzed meshes were greater than 40 meshes. As a result, the number of 40 meshes was relatively valid for further analysis in this study.

#### **4.2.1 Effect of Wheel Configuration**

The types of wheel configuration significantly influenced the critical tensile stresses below the concrete slab. The results appeared in Table 4.1 clearly showed that as the number of wheels in the landing gear increased, critical tensile stress decreased. Moreover, the moving directions had a significant effect on the evaluated stress since the landing gear layouts were asymmetric between moving in X and Y directions. The asymmetry of the landing gear layout led to the change of center point of loading. Therefore, the tensile stresses at the slab became noticeably different when the moving directions were changed.

#### **4.2.2 Critical Location for Tensile Stress at Bottom of Slab**

Critical tensile stresses from edge loading were observed as shown in Table 4.1. For the dual wheel landing gear, the critical tensile stress occurred at the center of the tire nearest to the center of the joint when the evaluated stress direction and the moving direction of the landing gear were the same.

With regard to the dual tandem configuration, the critical tensile stress occurred at the center of the tire placed closest to the joint center, when the moving direction was perpendicular to the evaluated stress direction. However, it also depended on the transverse and longitudinal lengths between each tire of the landing gear. In this case, the transverse length was smaller than the longitudinal length, but if it was higher, the relationship between the moving direction and the evaluated stress direction would be similar to the results from the dual wheel case as mentioned earlier.

#### 4.2.3 Critical Locations for Tensile Stress on Slab Surface

The procedure to obtain the critical location of tensile stress on the slab surface was more complex than the way to evaluate the critical tensile stress at the bottom. The principal tensile stress was expected to occur on the diagonal line from the loaded corner to the opposite corner since the slab dimension was the symmetrical shape. The principal tensile stresses on slab surface along the mentioned diagonal line were provided in Table 4.2. It could be noticed that the critical locations of principal tensile stress were likely to be located between the first and the second quartile of the full length of the diagonal line starting from the loaded point. For instance, the length of the diagonal line was about 250 inches. The coordination of critical location of dual wheel gear loading on a single slab was around 45 inches in x-coordinate and 45 inches in y-coordinate. This meant the distance from the loaded corner to the critical location was around 64 inches accounted for 25.6 percent of the diagonal line's full length. Another example, when the critical location of dual tandem wheel was loading on multiple slabs, their critical location was found being around 75 inches and 15 inches in x and y-coordination respectively. As a result, the distance between the loaded point and the critical location of about 106 inches was actually found. This meant that the critical location was located about 42 percent of diagonal length away from the loaded corner. Therefore, it could be summarized that the critical location varied between the first and the second quartiles of the diagonal length from a loaded corner.

**TABLE 4.1 Mesh analysis for tensile stress at bottom of slab.**

Landing Gear	Moving Direction	Slab System	No. of Mesh	Tensile Stress			
				Edge center	Load Center	Tyre Edge	Tyre Center
				Y-Y	Y-Y	Y-Y	Y-Y
Dual wheel	Y-Y	D8-0-1	<b>30</b>	1051	1020	1051	1062
Dual wheel	Y-Y	D8-0-1	<b>40</b>	1111	1065	1111	1126
Dual wheel	Y-Y	D8-0-1	<b>50</b>	1084	833	1084	1122
Dual wheel	X-X	D8-0-1	<b>30</b>	374.6	417.3	737.1	771.7
Dual wheel	X-X	D8-0-1	<b>40</b>	388.1	434.5	789.5	791.5
Dual wheel	X-X	D8-0-1	<b>50</b>	333	411.6	784.2	828.8
Dual Tandem	Y-Y	D8-0-1	<b>30</b>	97.18	179.2	544.8	554
Dual Tandem	Y-Y	D8-0-1	<b>40</b>	93.52	169.9	576.4	581.3
Dual Tandem	Y-Y	D8-0-1	<b>50</b>	72.76	169.9	568.6	618
Dual Tandem	X-X	D8-0-1	<b>30</b>	582	493.9	637	664.3
Dual Tandem	X-X	D8-0-1	<b>40</b>	615.7	507	669.7	686.7
Dual Tandem	X-X	D8-0-1	<b>50</b>	523.6	503	654	685.6
Dual wheel	Y-Y	D8-0-9	<b>30</b>	826.6	670.6	826.6	843.4
Dual wheel	Y-Y	D8-0-9	<b>40</b>	842.3	683.9	842.3	861.2
Dual wheel	Y-Y	D8-0-9	<b>50</b>	837.1	704.9	837.1	893.8
Dual wheel	X-X	D8-0-9	<b>30</b>	312.9	307.4	405.7	519.2
Dual wheel	X-X	D8-0-9	<b>40</b>	277	305.8	649.6	668.6
Dual wheel	X-X	D8-0-9	<b>50</b>	236.7	296	601.2	659.2
Dual Tandem	Y-Y	D8-0-9	<b>30</b>	138.9	145	442.4	433.1
Dual Tandem	Y-Y	D8-0-9	<b>40</b>	89.82	147.6	363.8	394.8
Dual Tandem	Y-Y	D8-0-9	<b>50</b>	86.77	146.6	390	419.2
Dual Tandem	X-X	D8-0-9	<b>30</b>	439.5	424.1	391.9	437.6
Dual Tandem	X-X	D8-0-9	<b>40</b>	417	435.3	425.6	450.4
Dual Tandem	X-X	D8-0-9	<b>50</b>	397.9	427	408.1	447.9

**TABLE 4.2 Mesh analysis of tensile stress on surface of concrete slab along diagonal path**

<b>Principal Tensile Stress</b>									
<b>Landing Gear</b>	<b>Moving Direction</b>	<b>Slab System</b>	<b>No. of Mesh</b>	<b>Principal Tensile Stress</b>					
				<b>(x,y)</b>					
				<b>(15,75)</b>	<b>(30,60)</b>	<b>(45,45)</b>	<b>(60,30)</b>	<b>(75,15)</b>	<b>(90,0)</b>
Dual wheel	Y-Y	D8-0-1	30	-316	-29	234	214	136	68
Dual wheel	Y-Y	D8-0-1	40	-279	41	262	230	143	69
Dual wheel	Y-Y	D8-0-1	50	-264	44	267	231	143	69
Dual wheel	X-X	D8-0-1	30	-316	-29	234	214	136	62
Dual wheel	X-X	D8-0-1	40	-279	42	262	230	143	69
Dual wheel	X-X	D8-0-1	50	-264	44	267	231	143	69
Dual Tandem	Y-Y	D8-0-1	30	-244	-63	23	153	138	86
Dual Tandem	Y-Y	D8-0-1	40	-222	-32	45	167	145	88
Dual Tandem	Y-Y	D8-0-1	50	-208	-29	48	169	145	88
Dual Tandem	X-X	D8-0-1	30	-242	-63	24	153	138	86
Dual Tandem	X-X	D8-0-1	40	-220	-32	45	167	145	88
Dual Tandem	X-X	D8-0-1	50	-206	-28	48	170	145	88
Dual wheel	Y-Y	D8-0-9	30	-289	-143	136	163	114	67
Dual wheel	Y-Y	D8-0-9	40	-233	-68	174	178	121	65
Dual wheel	Y-Y	D8-0-9	50	-214	-41	170	173	120	65
Dual wheel	X-X	D8-0-9	30	-294	-154	138	163	113	67
Dual wheel	X-X	D8-0-9	40	-233	-67	174	178	121	65
Dual wheel	X-X	D8-0-9	50	-214	-41	170	173	120	65
Dual Tandem	Y-Y	D8-0-9	30	-218	-139	-29	105	113	83
Dual Tandem	Y-Y	D8-0-9	40	-170	-86	5	126	124	83
Dual Tandem	Y-Y	D8-0-9	50	-204	-71	2	123	122	82
Dual Tandem	X-X	D8-0-9	30	-219	-139	-27	105	113	83
Dual Tandem	X-X	D8-0-9	40	-171	-86	5	126	124	83
Dual Tandem	X-X	D8-0-9	50	-205	-71	3	123	122	82

#### 4.3 Critical Tensile Stress at Bottom of Slab and Stress-based LTE

The LTE calculated by critical tensile stress could be computed using Equation 2.3 as mentioned in the literature review. The unloaded and loaded stresses were obtained from the analysis of 9-slab pavement system, while the free edge stresses were gathered from the analysis of single-slab pavement system.



The comparison between critical tensile stress outputs at the free edge of single slab and the loaded and unloaded slab of the 9-slab analysis were illustrated in Table 4.3. Discussions on the variations of the assigned conditions were as follows;

#### **4.3.1 Effect of Temperature Gradient and Slab Thickness on Critical Stress**

In Table 4.3, the critical tensile stresses below the slab decreased as temperature gradient became negative. This could be described by the existence of a base layer below the slab in which the negative temperature stress caused the curled-up slab. On the other hand, the critical tensile stress under slab increased as the temperature gradient of the slab became positive. The main reason was that while the positive temperature stress caused a slab to curl down, it also introduced the additional tensile stress at the bottom of slab. Moreover, it appeared that the critical tensile stress at the bottom of slab increased as the thickness decreased.

#### **4.3.2 Comparison of Critical Stresses Between Single Slab and Multiple Slabs**

The comparison between the critical stress at the free edge of single slab and the critical stress at the loaded slab of multiple slabs should be investigated to validate the assumption in FAARFIELD. The ratio of stress at the loaded slab of multiple slabs and the stress at the free edge of single slab was assumed as 75 percent in FAARFIELD to consider multi-slab effect.

In this study, the ratio of the stress on the loaded slab of 9-slab and the stress on the free edge of the single slab was provided in Table 4.4. From the analyzed data, the combinations of temperature gradient and slab thickness had noticeable influence on the

ratio between the critical stress of 9-slab and the 1-slab pavement system ( $S_9/S_1$ ). The  $S_9/S_1$  were ranging between 68 and 81 percent as the temperature gradients ranged from 0 to 2 °F/in (Figure 4.11). However, the high variation occurred when the slab thickness became rising at a negative temperature gradient. Specifically, as the temperature gradient changed from 0 to -2 °F/inch, the  $S_9/S_1$  values of the 16-inch slab thickness with dual wheel and with dual tandem loading jumped from 79 percent to 99 percent, and 68 to 106 percent, respectively, while the  $S_9/S_1$  values of the 8-inch with dual wheel and dual tandem loading slightly changed from 78 to 76 percent, and 68 to 66 percent respectively.

As appeared in Figure 4.12, the results also showed that as the slab thickness increased, the  $S_9/S_1$  ratios were relatively constant when the temperature gradients ranged between 0° to 2° F /inch. But, when the temperature gradients became negative, the  $S_9/S_1$  ratios noticeably increased as the slab thickness increased.

### 4.3.3 Stress-based Load Transfer Efficiency

The stress-based LTEs were calculated and listed in Table 4.4 by using Equation 2.3. Additionally, their relationship with the temperature gradients and the slab thicknesses were plotted in Figure 4.13 and 4.14 respectively. The chart in Figure 4.13 showed that the LTE increased remarkably as the temperature gradient of the slab increased. Moreover, in zero and positive slab's temperature gradient conditions, the LTE gradually declined as the slab thickness increased as appeared in Figure 4.14. However, when the slab temperature gradient was negative, the LTE dropped significantly as the slab became thicker.

As mentioned by Guo (2003), the free edge stress should be equal to the summation of loaded and unloaded stresses for the flat slab with no curling condition. In other words, the ratio of the free edge stress and the summation of loaded and unloaded stresses should be equal to 1. In this analysis, the ratio of the edge stress and the summation of the loaded and unloaded stresses (FE/LU) were also provided in Figure 4.15 and 4.16. Concerning the flat slab and the curling-down slab, the results showed that the FE/LU values of the flat slab and the curling down slab were approximately 90 and 82 percent, respectively. However, the FE/LU values of the curling up slab diverged in a wide range from 77 to 110 percent and the FE/LU values of the curling up slab also did decrease as the thickness increased.

**TABLE 4.3 Critical tensile stresses below slab from edge loading of single slab and 9-slab system.**

<b>Analysis Case</b>	<b>Temp. Gradient</b>	<b>Thickness</b>	<b>Moving Direction</b>	<b>Stress Direction</b>	<b>Location of Critical Stress (x,y,z)</b>	<b>Critical Stress 1-Slab, psi</b>	<b>Stress at loaded Slab, psi</b>	<b>% S9/S1</b>
Dual Wh 8in/-2F/400	-2	8	Y-Y	Y-Y	6.4,0,0	950	725	76%
Dual Wh 8in/0F/400	0	8	Y-Y	Y-Y	6.4,0,0	1101	856	78%
Dual Wh 8in/2F/400	2	8	Y-Y	Y-Y	6.4,0,0	1308	1060	81%
Dual Wh 12in/-2F/400	-2	12	Y-Y	Y-Y	6.4,0,0	556	477	86%
Dual Wh 12in/0F/400	0	12	Y-Y	Y-Y	6.4,0,0	727	574	79%
Dual Wh 12in/2F/400	2	12	Y-Y	Y-Y	6.4,0,0	995	784	79%
Dual Wh 16in/-2F/400	-2	16	Y-Y	Y-Y	6.4,0,0	348	344	99%
Dual Wh 16in/0F/400	0	16	Y-Y	Y-Y	6.4,0,0	514	405	79%
Dual Wh 16in/2F/400	2	16	Y-Y	Y-Y	6.4,0,0	754	580	77%
Dual Tan. 8in/-2F/400	-2	8	X-X	Y-Y	7,9.55,0	522	344	66%
Dual Tan. 8in/0F/400	0	8	X-X	Y-Y	7,9.55,0	658	451	69%
Dual Tan. 8in/2F/400	2	8	X-X	Y-Y	7,9.55,0	871	666	76%
Dual Tan. 12in/-2F/400	-2	12	X-X	Y-Y	7,9.55,0	315	277	88%
Dual Tan. 12in/0F/400	0	12	X-X	Y-Y	7,9.55,0	479	353	74%
Dual Tan. 12in/2F/400	2	12	X-X	Y-Y	7,9.55,0	742	570	77%
Dual Tan. 16in/-2F/400	-2	16	X-X	Y-Y	7,9.55,0	199	211	106%
Dual Tan. 16in/0F/400	0	16	X-X	Y-Y	7,9.55,0	359	245	68%
Dual Tan. 16in/2F/400	2	16	X-X	Y-Y	7,9.55,0	596	442	74%

**TABLE 4.4 Comparison of stresses on unloaded slab and loaded slab on 9-slab system.**

Analysis Case	Temp. Gradient	Thickness	Moving Direction	Stress Direction	Location of Critical Stress (x,y,z)	(1)	(2)	(2)/(1)	(3)	(1)/((2)+(3))	(3)/((2)+(3))	(3)/(1)	(3)/(2)
						Critical Stress 1-Slab	Critical Stress 9-Slab	S9/S1, %	Stress at unloaded slab	Free edge/(loaded+unloaded stresses), %	Stress-based LTE, %	Unloaded/Free edge, %	Unloaded/Loaded, %
Dual Wh 8in/-2F/400	-2	8	Y-Y	Y-Y	6.4,0,0	950	725	76%	258	97%	26%	27%	36%
Dual Wh 8in/0F/400	0	8	Y-Y	Y-Y	6.4,0,0	1101	856	78%	374	90%	30%	34%	44%
Dual Wh 8in/2F/400	2	8	Y-Y	Y-Y	6.4,0,0	1308	1060	81%	566	80%	35%	43%	53%
Dual Wh 12in/-2F/400	-2	12	Y-Y	Y-Y	6.4,0,0	556	477	86%	134	91%	22%	24%	28%
Dual Wh 12in/0F/400	0	12	Y-Y	Y-Y	6.4,0,0	727	574	79%	229	90%	29%	32%	40%
Dual Wh 12in/2F/400	2	12	Y-Y	Y-Y	6.4,0,0	995	784	79%	432	82%	36%	43%	55%
Dual Wh 16in/-2F/400	-2	16	Y-Y	Y-Y	6.4,0,0	348	344	99%	70	84%	17%	20%	20%
Dual Wh 16in/0F/400	0	16	Y-Y	Y-Y	6.4,0,0	514	405	79%	156	91%	28%	30%	38%
Dual Wh 16in/2F/400	2	16	Y-Y	Y-Y	6.4,0,0	754	580	77%	306	85%	34%	41%	53%
Dual Tan. 8in/-2F/400	-2	8	X-X	Y-Y	7,9.55,0	522	344	66%	133	110%	28%	25%	39%
Dual Tan. 8in/0F/400	0	8	X-X	Y-Y	7,9.55,0	658	451	69%	248	94%	35%	38%	55%
Dual Tan. 8in/2F/400	2	8	X-X	Y-Y	7,9.55,0	871	666	76%	438	79%	40%	50%	66%
Dual Tan. 12in/-2F/400	-2	12	X-X	Y-Y	7,9.55,0	315	277	88%	81	88%	23%	26%	29%
Dual Tan. 12in/0F/400	0	12	X-X	Y-Y	7,9.55,0	479	353	74%	173	91%	33%	36%	49%
Dual Tan. 12in/2F/400	2	12	X-X	Y-Y	7,9.55,0	742	570	77%	367	79%	39%	50%	64%
Dual Tan. 16in/-2F/400	-2	16	X-X	Y-Y	7,9.55,0	199	211	106%	47	77%	18%	23%	22%
Dual Tan. 16in/0F/400	0	16	X-X	Y-Y	7,9.55,0	359	245	68%	153	90%	38%	43%	62%
Dual Tan. 16in/2F/400	2	16	X-X	Y-Y	7,9.55,0	596	442	74%	278	83%	39%	47%	63%

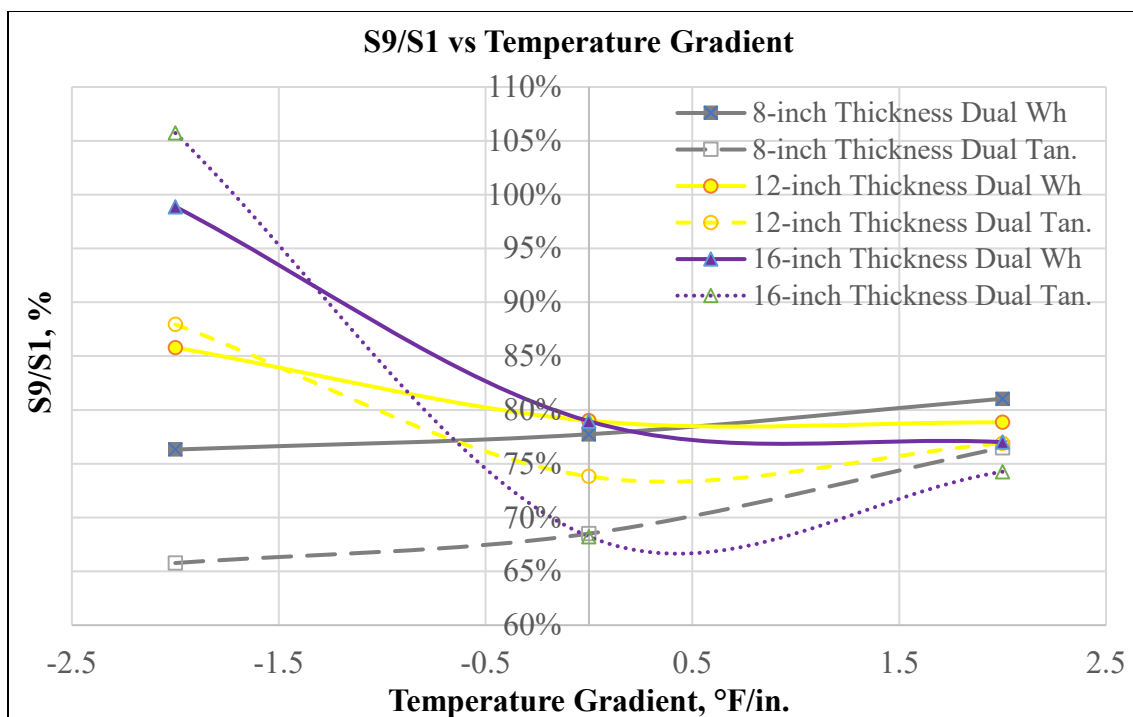


**FIGURE 4.11 Relationship between S9/S1 and temperature gradient.**

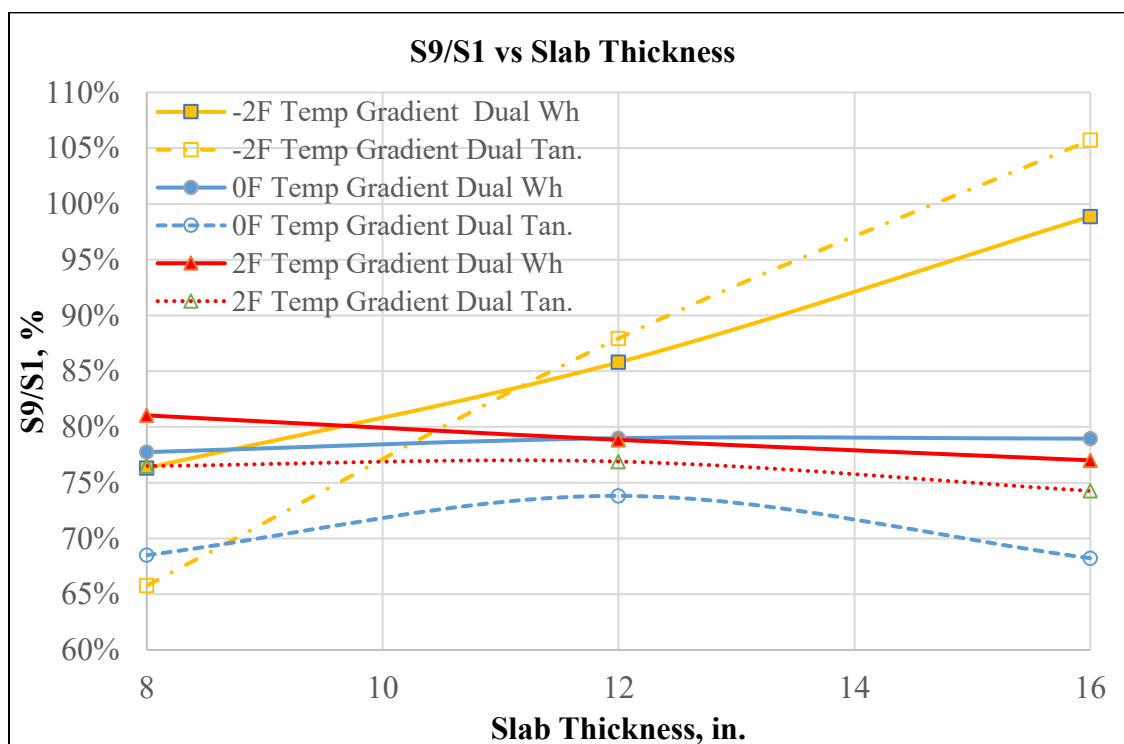


**FIGURE 4.12 Relationship between S9/S1 and slab thickness.**

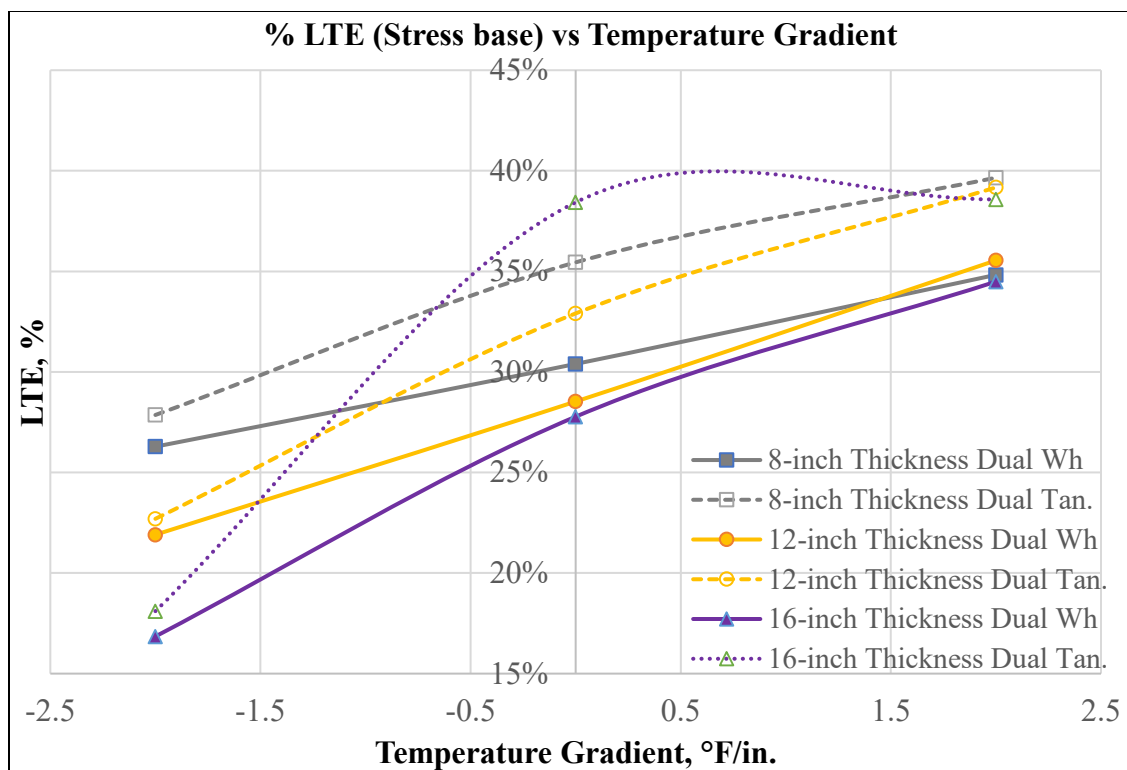


**FIGURE 4.13 Relationship between stress-based LTE and temperature gradient of slab.**

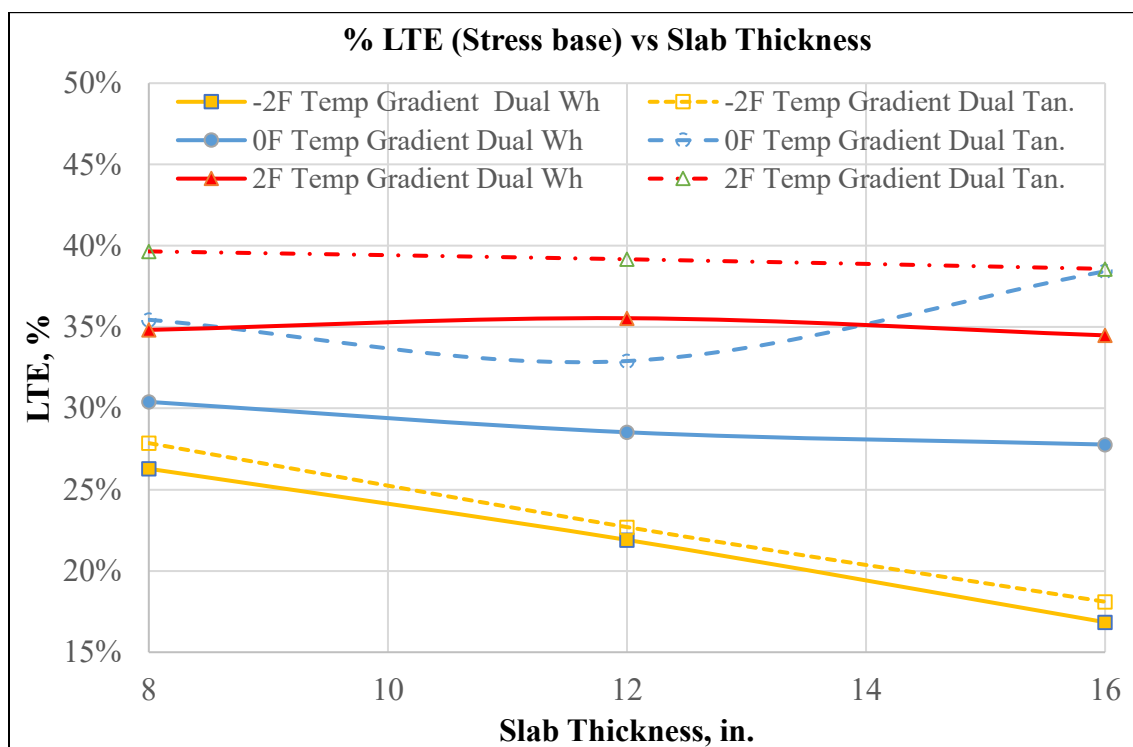


**FIGURE 4.14 Relationship between stress-based LTE and slab thickness.**

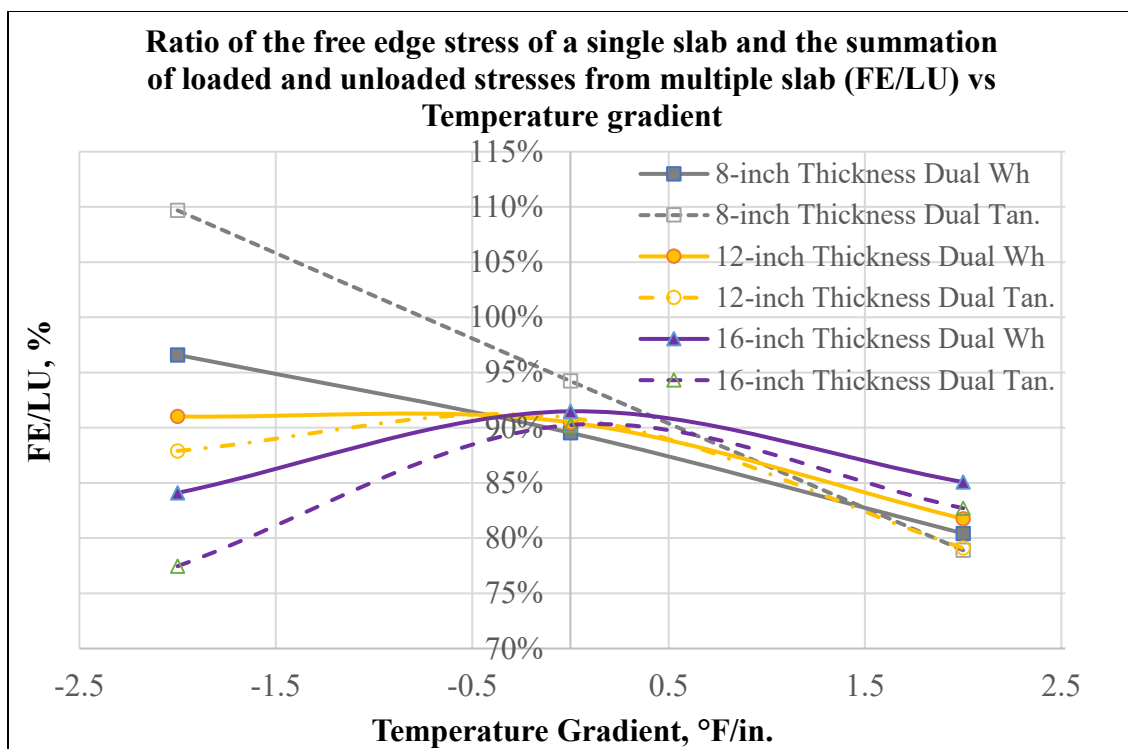


**FIGURE 4.15 Relationship between ratio of free edge and summation of loaded and unloaded stress and temperature gradient of slab.**

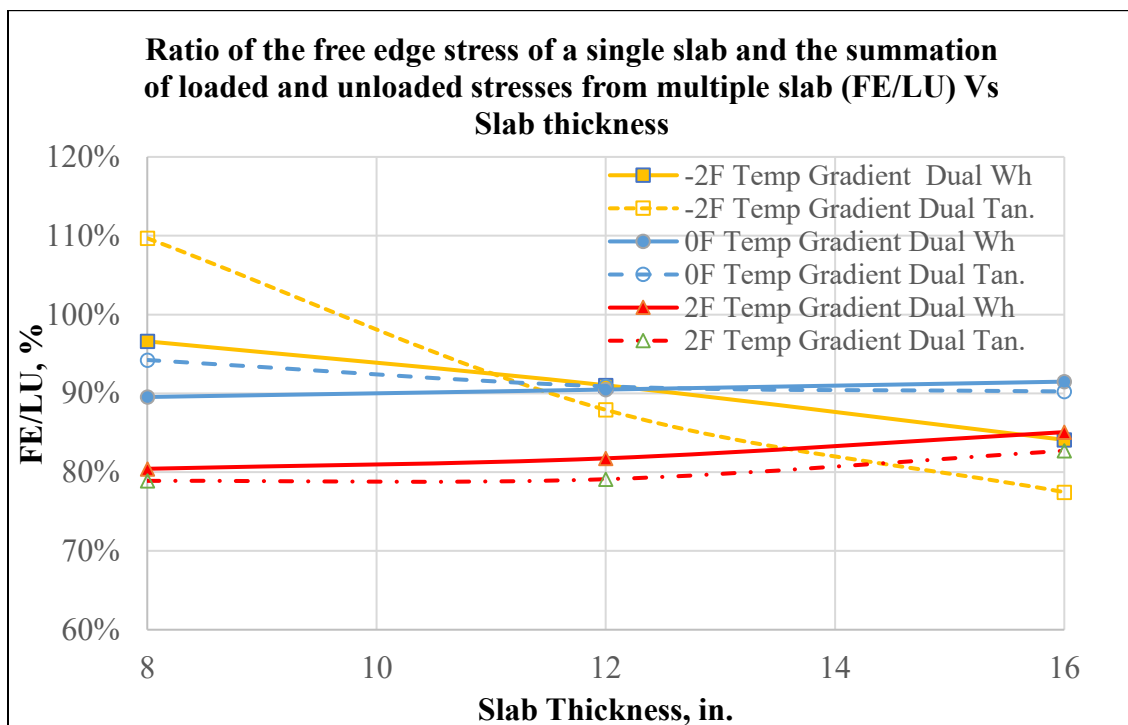


**FIGURE 4.16 Relationship between ratio of free edge and summation of loaded and unloaded stress and slab thickness.**



#### **4.4 Critical Tensile Stress on Slab Surface**

As described in the literature review, the failure mode of rigid pavement possibly occurred at the top surface due to the fact that the corner loading generally introduced the top-down cracks. In conjunction with that, the corner loading of dual wheel and dual tandem on the rigid slab were employed in this analysis to monitor critical tensile stress on slab surface.

##### **4.4.1 Illustration of Stress Contour on Slab Surface**

The outputs from FEAFAA could not show the principal stress contour, and some visualized outputs could be illustrated only the stresses in either X or Y directions. So, the output stresses in Y directions of the PCC slab were plotted by the Techplot360 so as to explain stress on the slab surface at different conditions as shown in Figure 4.17 to 4.20.

For the loading on single slab, the results appeared in Figure 4.17 and 4.18 illustrated that the critical tensile stresses of both dual wheel and dual tandem landing gears occurred on the slab surface when the temperature gradient became negative. Moreover, in multiple slab pavements, the results in Figure 4.19 and 4.20 illustrated that there were significant amounts of tensile stress occurring on the adjacent slab which should not be neglected.

Since the slab was squared shape, critical tensile stress on the slab surface was likely to occur on one point along the diagonal line from the loaded corner to the opposite unloaded corner. Moreover, the evaluated stress was monitored in the principal direction in order to obtain the highest tensile stress. The results were shown in Table 4.5.

#### **4.4.2 Effect of Temperature Gradient and Slab Thickness**

Dissimilar to the trends of the critical tensile stress locating at the bottom of slab, the critical tensile stress on the top surface increased as the temperature gradient of the slab turned into negative value. The main reason behind this pattern was the tensile stress generated on the slab surface by the negative temperature gradient. Nevertheless, when the temperature gradient turned into a positive value, the critical tensile stress on the slab surface was considerably reduced.

For the effect of slab thickness, it can be seen that the critical tensile stress on slab surface reduced accordingly as the slab thickness increased.

The critical locations of tensile stress for loading on the slab corner were different from the ones for loading on the slab edge. For loading on the slab edge, the critical locations were less sensitive to the inclination of the slab thickness and temperature gradient. In contrast, the critical locations for loading on the slab corner were influenced by the slab thickness. The results derived from Table 4.5 obviously showed that the critical stress locations of single slab noticeably moved toward the loaded position as the slab thickness increased.

#### **4.4.3 Comparison of Critical Stresses Between Single Slab and Multiple Slabs**

In Table 4.5 with regard to the flat slabs, the ratio of stress on loaded slab corner of multiple slab system and single slab system ( $S_9/S_1$ ) was ranging from 51 to 83 percent with a mean value of 65 percent. Moreover, it was found that the  $S_9/S_1$  was affected by temperature gradient and slab thickness.

As the slab curled up, the S9/S1 increased significantly ranging from 79 to 92 percent with average value of 85 percent. The inclination of this S9/S1 was interfered by the addition of tensile stress on the slab surface caused by the negative temperature gradient. The S9/S1 greatly increased as the temperature gradient changed from 0 °F/in. to -2 °F/in., however, it was likely to be unchanged when the temperature gradient changed from -2 °F/in. to -4 °F/in. as shown in Figure 4.21. Unfortunately, as the temperature gradient became positive, the S9/S1 could not be identified. In some cases, there was no tensile stress on the slab surface since they were eliminated by the compressive stress introduced by the positive temperature gradient. This implied that the S9/S1 should be considered with more attention on the flat slab since it was not affected by temperature stresses.

Furthermore, the S9/S1 of flat slab decreased as the slab thickness increased as illustrated in Figure 4.22. However, this behavior was only for flat slab with zero-temperature gradient. The plotted curves in Figure 4.22 also showed that the increase of slab thickness from 8 to 16 in. did not affect the S9/S1 of the slab with negative temperature gradient.

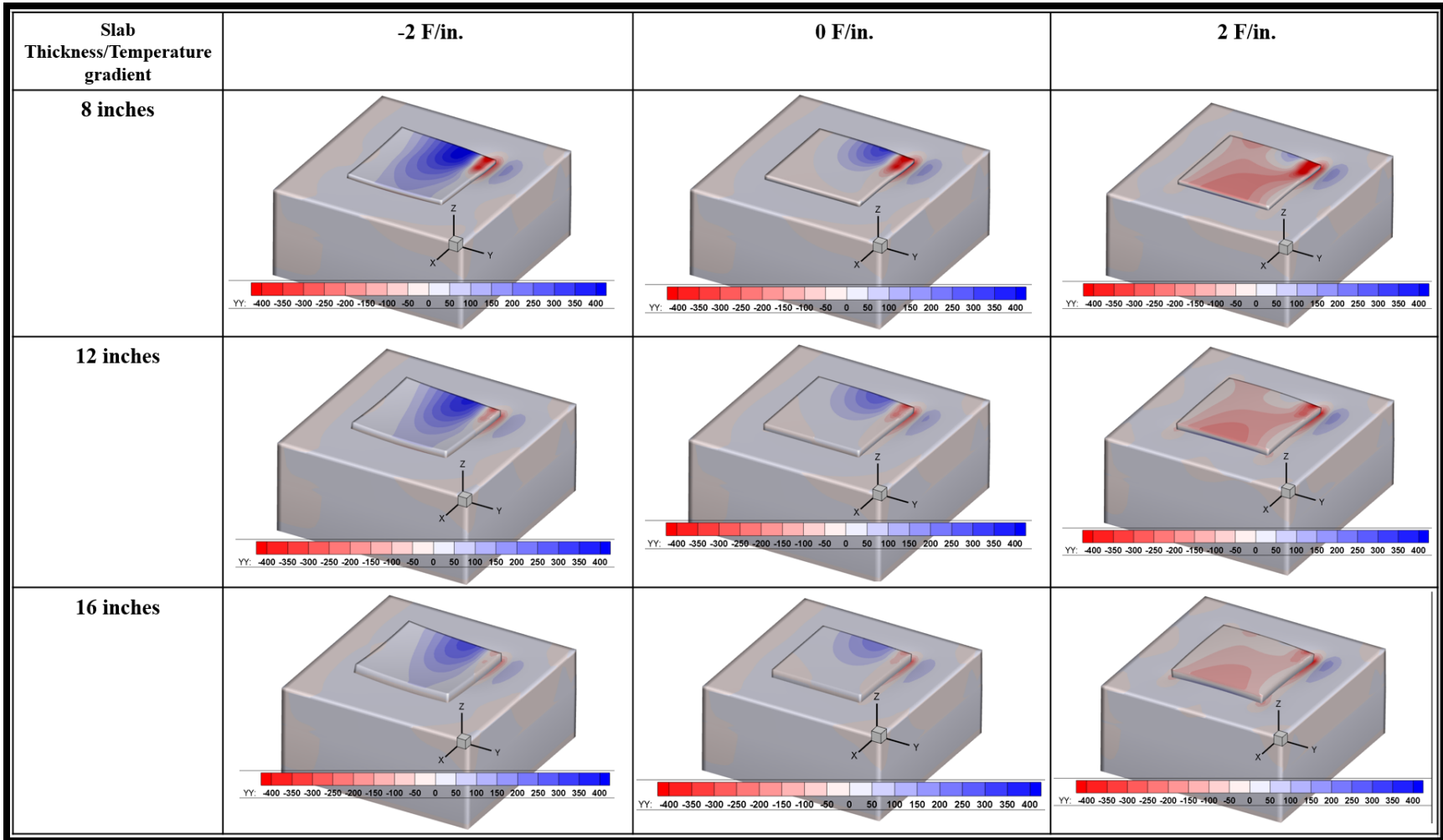


FIGURE 4.17 Surface stress in Y-direction under dual wheel moving in Y-direction loaded on single slab at corner.

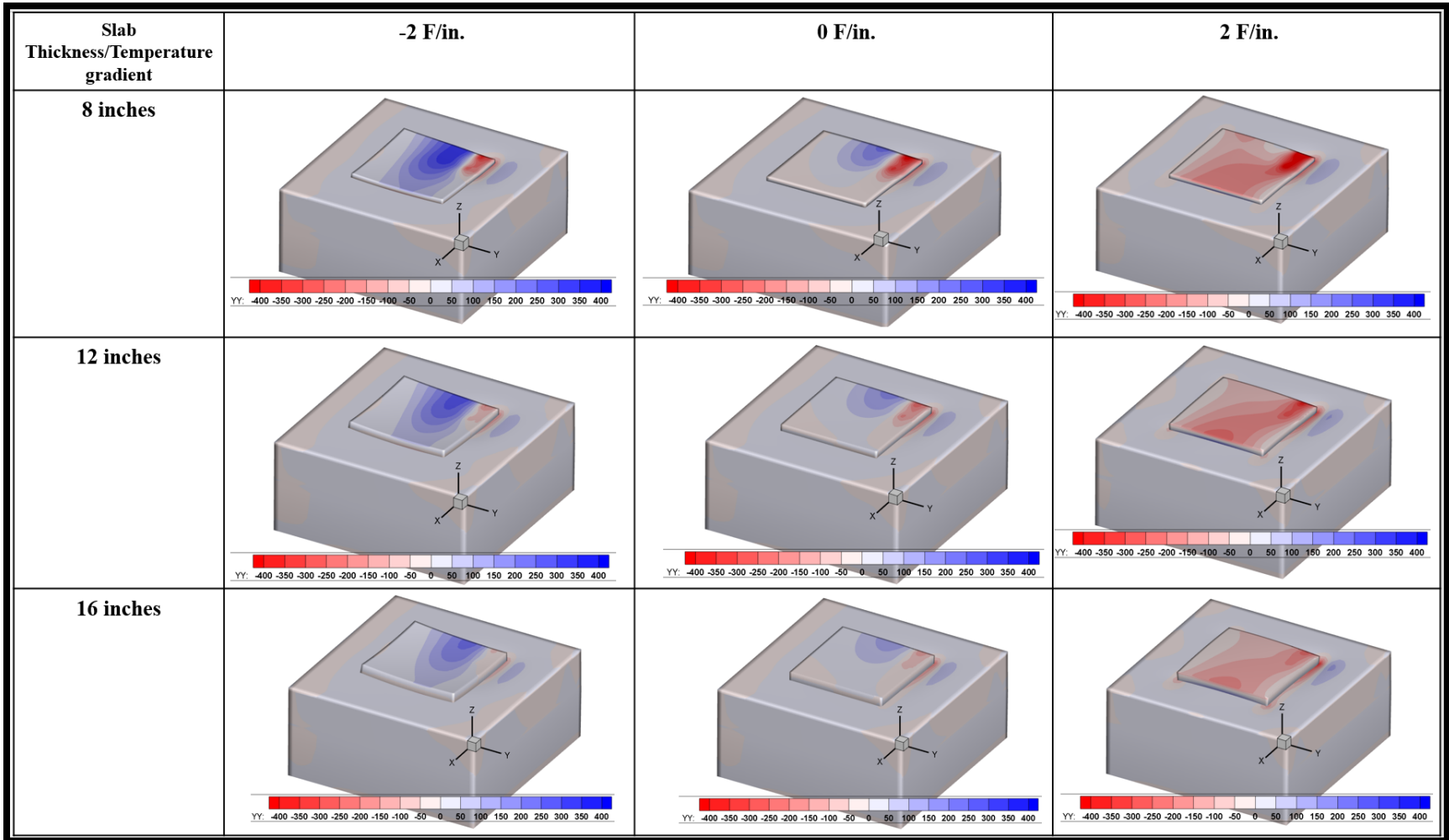


FIGURE 4.18 Surface stress in Y-direction under dual tandem moving in X-direction loaded on single slab at corner.

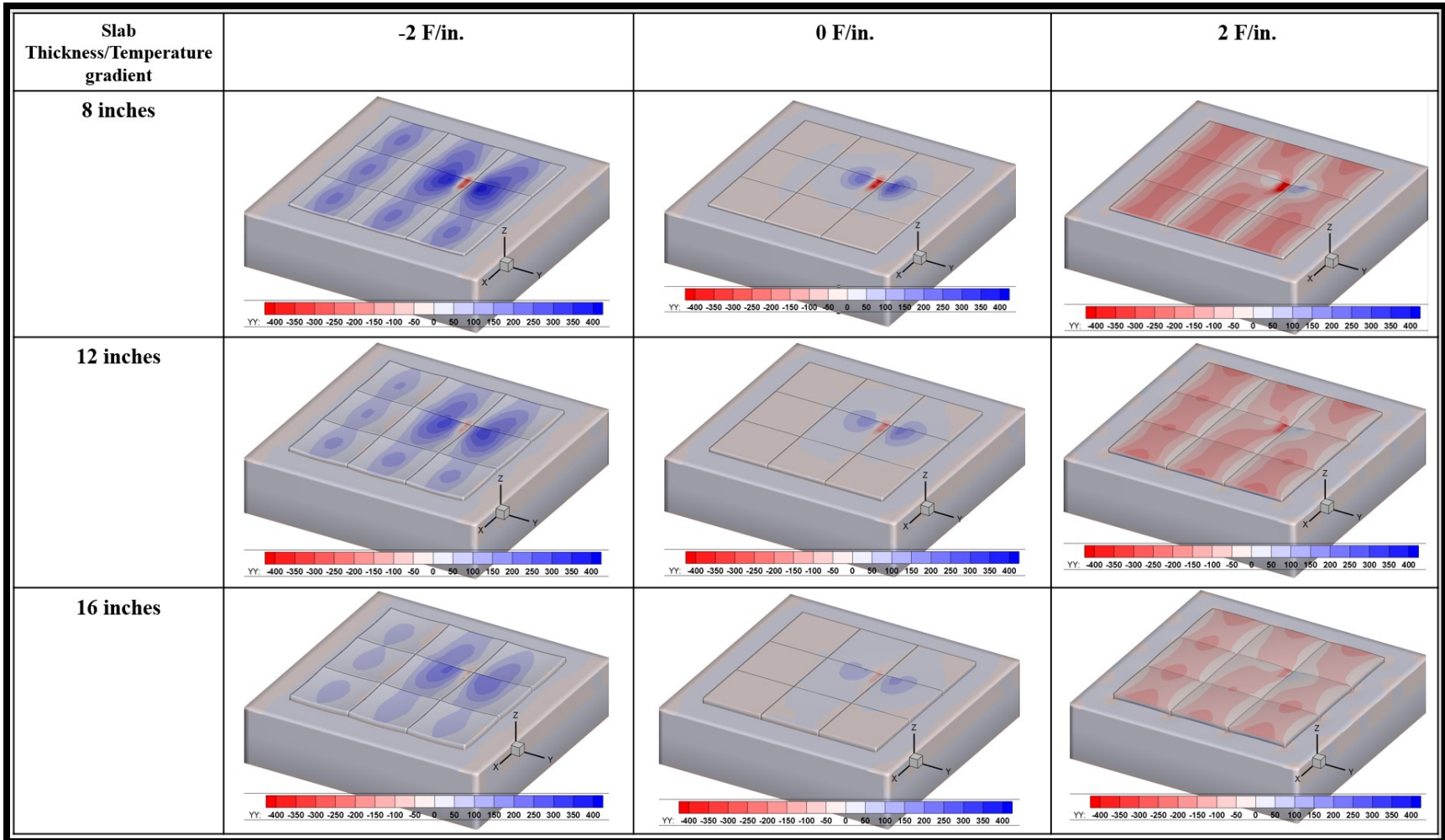


FIGURE 4.19 Surface stress in Y-direction under dual wheel moving in Y-direction loaded at corner of 9-slab system.

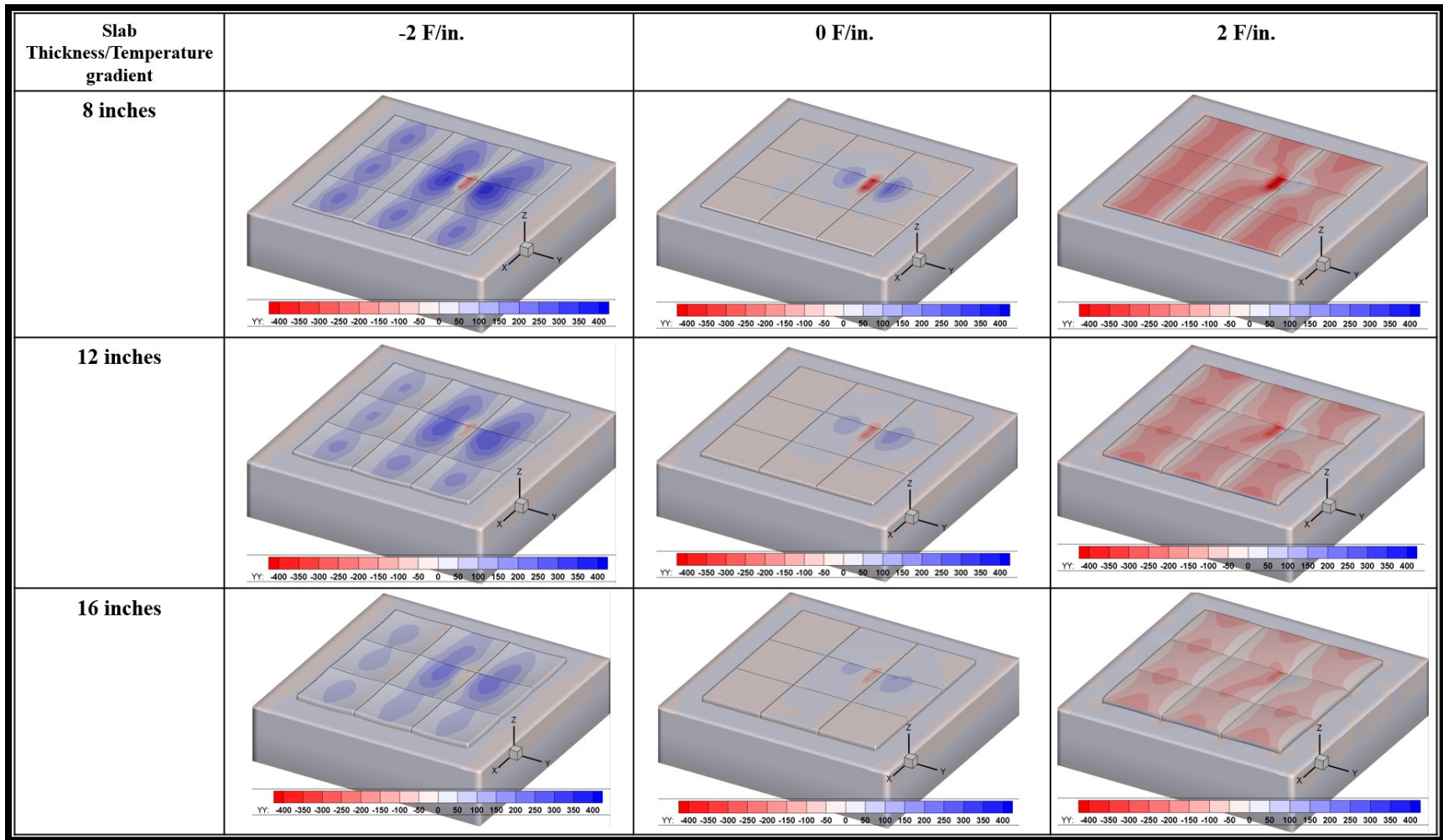
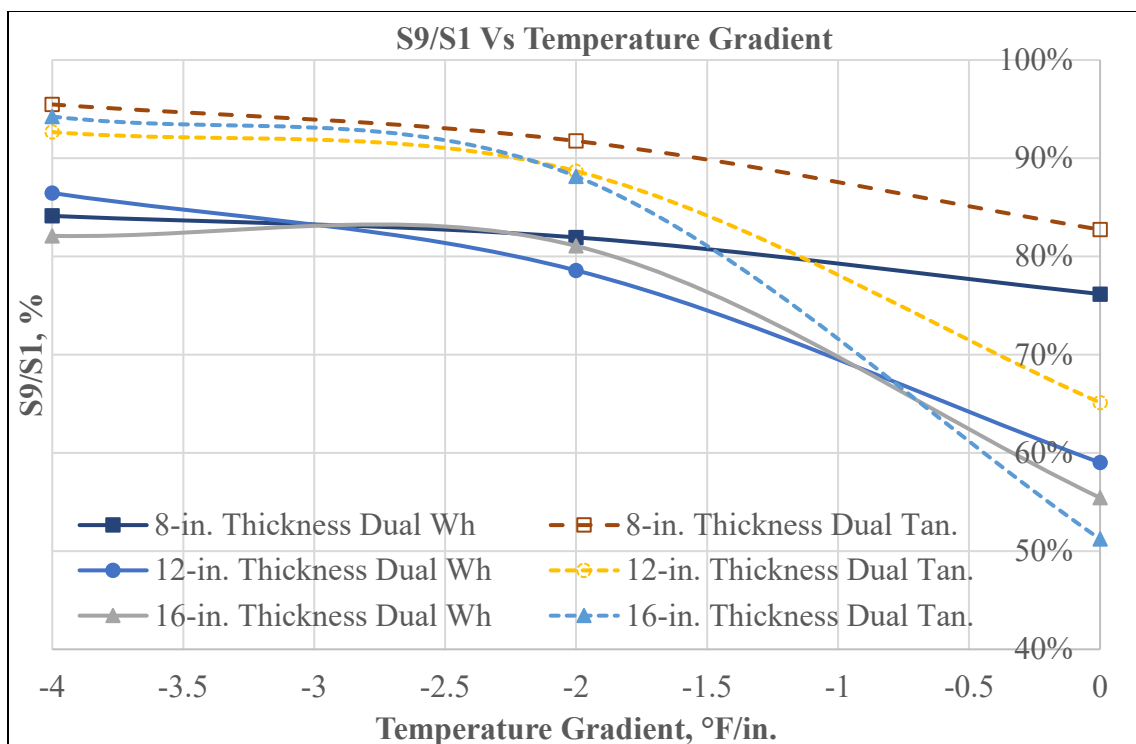


FIGURE 4.20 Surface stress in Y-direction under dual tandem moving in X-direction loaded at corner of 9-slab system.

**TABLE 4.5 Critical tensile stresses on surface of slab from corner loading of single slab system analysis and 9-slab system analysis from different input criteria.**

Analysis Case	Temp. Gradient, F/in.	Thickness, in.	Moving Direction	Stress Direction	Single Slab		Multiple Slab		% S9/S1
					Location of Critical Stress (x,y,z)	Critical Tensile Stress, psi	Location of Critical Stress (x,y,z)	Critical Tensile Stress, psi	
Dual Wh 8in/-4F/400	-4	8	Y-Y	Principal Stress	50,40,8	614	50,40,8	516	84%
Dual Wh 8in/-2F/400	-2				50.4,39.6,8	459	50,40,8	376	82%
Dual Wh 8in/0F/400	0				50.4,39.6,8	269	50,40,8	205	76%
Dual Wh 8in/2F/400	2				47.5,42.5,8	85	50,40,8	N/A	N/A
Dual Wh 12in/-4F/400	-4	12	Y-Y		46,44,12	475	60,30,12	410	86%
Dual Wh 12in/-2F/400	-2				46,44,12	384	60,30,12	302	79%
Dual Wh 12in/0F/400	0				46,44,12	232	50,40,12	137	59%
Dual Wh 12in/2F/400	2				46,44,12	2	50,40,12	N/A	N/A
Dual Wh 16in/-4F/400	-4	16	Y-Y		42,48,16	361	60,30,16	296	82%
Dual Wh 16in/-2F/400	-2				42,48,16	290	60,30,16	235	81%
Dual Wh 16in/0F/400	0				42,48,16	186	50,40,16	103	55%
Dual Wh 16in/2F/400	2				46,44,16	3	50,40,16	N/A	N/A
Dual Tan. 8in/-4F/400	-4	8	X-X		64,26,8	502	64,26,8	479	95%
Dual Tan. 8in/-2F/400	-2				66,24,8	361	68,22,8	332	92%
Dual Tan. 8in/0F/400	0				66,24,8	167	68,22,8	138	83%
Dual Tan. 8in/2F/400	2				60,30,8	-61	55,35,8	N/A	N/A
Dual Tan. 12in/-4F/400	-4	12	X-X		60,30,12	395	68,22,12	366	93%
Dual Tan. 12in/-2F/400	-2				64,26,12	299	68,22,12	265	89%
Dual Tan. 12in/0F/400	0				64,26,12	142	68,22,12	92	65%
Dual Tan. 12in/2F/400	2				64,26,12	-92	68,22,12	N/A	N/A
Dual Tan. 16in/-4F/400	-4	16	X-X		60,30,16	284	74,16,16	268	94%
Dual Tan. 16in/-2F/400	-2				64,26,16	229	72,18,16	202	88%
Dual Tan. 16in/0F/400	0				65,25,16	131	74,16,16	67	51%
Dual Tan. 16in/2F/400	2				68,22,16	-58	74,16,16	N/A	N/A





**FIGURE 4.21 Relationship between S9/S1 and slab thickness.**

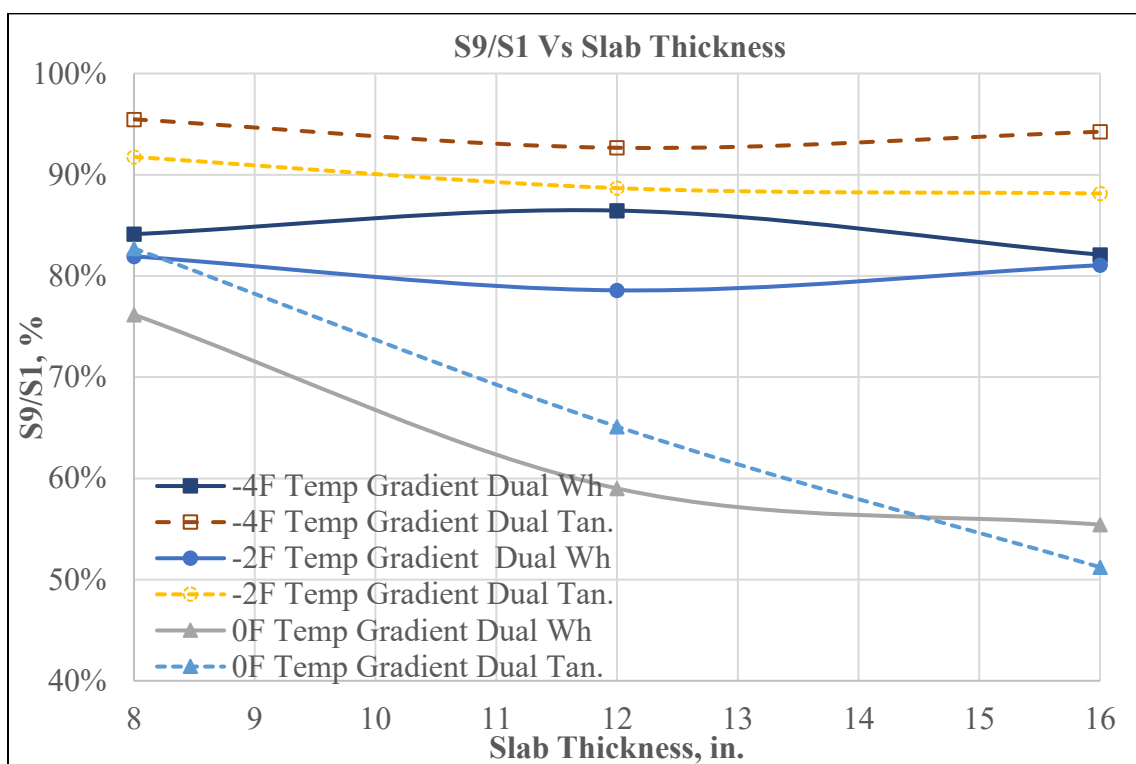


**FIGURE 4.22 Relationship between S9/S1 and temperature gradient.**

#### 4.5 Comparison of critical tensile stresses at bottom and surface of slab

The comparison of the critical tensile stress at the bottom and the surface of slab were illustrated in Table 4.6. The results from all scenarios showed that the critical tensile stresses at the bottom of slab were greater than the critical tensile stresses at the slab surface. Therefore, the top-down cracking was less likely to occur in the assigned scenarios.

**TABLE 4.6 Critical tensile stress at bottom and surface of slab**

Analysis Case	Temp. Gradient	Thickness	Bottom		Surface	
			Critical Stress 1-Slab	Critical Stress 9-Slab	Critical Stress 1-Slab	Critical Stress 9-Slab
Dual Wh 8in/-2F/400	-2	8	950	725	459	376
Dual Wh 8in/0F/400	0	8	1101	856	269	205
Dual Wh 8in/2F/400	2	8	1308	1060	85	N/A
Dual Wh 12in/-2F/400	-2	12	556	477	384	302
Dual Wh 12in/0F/400	0	12	727	574	232	137
Dual Wh 12in/2F/400	2	12	995	784	2	N/A
Dual Wh 16in/-2F/400	-2	16	348	344	290	235
Dual Wh 16in/0F/400	0	16	514	405	186	103
Dual Wh 16in/2F/400	2	16	754	580	3	N/A
Dual Tan. 8in/-2F/400	-2	8	522	344	361	332
Dual Tan. 8in/0F/400	0	8	658	451	167	138
Dual Tan. 8in/2F/400	2	8	871	666	-61	N/A
Dual Tan. 12in/-2F/400	-2	12	315	277	299	265
Dual Tan. 12in/0F/400	0	12	479	353	142	92
Dual Tan. 12in/2F/400	2	12	742	570	-92	N/A
Dual Tan. 16in/-2F/400	-2	16	199	211	229	202
Dual Tan. 16in/0F/400	0	16	359	245	131	67
Dual Tan. 16in/2F/400	2	16	596	442	-58	N/A

## **CHAPTER 5**

### **CONCLUSIONS AND RECOMMENDATIONS**

#### **5.1 Conclusions**

This research focused separately into two main parts. In the first part, field deflection analysis and modulus backcalculation were performed well by the AREA method and the NUS-BACK solution. The results could be summarized as follows.

1. The deflection-based Load Transfer Efficiency (LTE) was lowest on the free edge corner of the concrete slab followed by the free edge center, the jointed edge corner and the jointed edge center of the concrete slab, respectively. Moreover, it was sensitive to the assessed position, the amount of load level, test direction, and the type adjacent support of the evaluated slab.
2. The deflection-based Load Transfer Efficiency (LTE) and the sum of deflection (SD) slightly increased as the load level rose up.
3. The radius of relative stiffness was substantially influenced by the type of adjacent support of the evaluated pavement.
4. The test-direction and the sensor configuration of the F/HWD test machine could significantly affect the test results including the backcalculated moduli.

5. The elastic modulus of concrete slab obtained by the AREA method was closely matched to the results tested in the laboratory, while the results obtained by the NUS-BACK seemed to be overestimated.
6. The modulus of subgrade reaction calculated by the AREA method and the NUS-BACK was noticeably greater than a lab test data because those methods assumed the pavement as the two-layered system. Therefore, the modulus of subgrade reaction obtained from those two methods displayed the properties of the composite layers of the base and subgrade.
7. The overlays calculated by the input of lab test data was more conservative than the AREA method and NUS-BACK. Moreover, the overlay thickness calculated by the input moduli of the NUS-BACK mostly resulted in the minimum value required by the FAARFIELD because the layered moduli provided by NUS-BACK seemed to be overestimated.

In the second part, the joint load transfer analysis of the airfield rigid pavement was comprehensively analyzed by the processing of three-dimensional finite element modeling analysis software. Based on the results of the analysis taken by the FEAFAA, the key findings can be summarized as follows:

1. Critical tensile stress

- 1.1) In contrast to the critical location for the tensile stress at the bottom of the slab, the critical location for the tensile stress on the slab surface

considerably influenced by the slab thickness, the landing gear configuration and the temperature gradient of the slab.

- 1.2) The temperature gradient and the slab thickness greatly influenced the critical tensile stress on both at the bottom of the slab and the surface.

## 2. S9/S1 and stress-based LTE

- 2.1) For the center edge loading, the variation of a ratio of stress in multiple slab and stress in the single slab ( $S9/S1$ ) occurred when the slab temperature gradient became negative as well as the slab thickness increased. However, for the corner loading, the variation of the  $S9/S1$  existed when the temperature gradient ranged between  $-2$  to  $0$  °F/in and the slab thickness increased.
- 2.2) The stress-based LTE remarkably increased as the temperature gradient of slab rose up and decreased as the slab thickness increased.
- 2.3) Although the results of  $S9/S1$  were closely tied to the assumption of 25 percent load transfer through the joint, it can be seen that the joint load transfer between the slabs was noticeably influenced by the temperature gradient of the slab and the slab thickness. Thus, it should not be specified as a constant value.

## 5.2 Recommendations for Future Research

Numerous recommendations for future research were listed as follows:

1. The type of adjacent support highly affected the backcalculated moduli. It should be considered in future work.
2. The implication of slab size correction factor for the backcalculation of slab moduli marginally affected the elastic modulus of the concrete slab, but it was significantly dominated the modulus of subgrade reaction.
3. It should be noted that the pavement structure of the round-up project was in nearly no traffic conditions. Obviously, their back calculated moduli were relatively high when compared to the actual pavement with traffic. Therefore, it could be inappropriate to use it for the input of overlay design since their layer moduli might be too high for the analysis.
4. The backcalculated results computed by the AREA method and the graphical NUS-BACK solution were provided in the two-layer system (concrete slab and subgrade). They were quite limited to apply as the inputs of the overlay design in the FAARFIELD because the software required to apply the properties of the existing layers with a minimum of three layers. To deal with the FAARFIELD requirement, the backcalculated modulus of subgrade reaction taken in this research was duplicated and applied to both as the base and the subgrade. Therefore, the consequences of this assumption should be considered in future works.
5. When the slab was curling, it might be inappropriate to evaluate the relationship between the critical tensile stress of single slab pavement and the critical tensile stress of multiple slab pavement in the ratio of stresses because they were greatly affected by the portion of curling stress. For example, the results in Table 4.3 showed that when the temperature gradient was  $-2^{\circ}\text{F}/\text{in.}$ , the  $S_9/S_1$  in some cases

were equal to and exceed 100%. It should be noticed that in the same loading conditions, the critical stress of multiple slabs pavement was less likely to exceed the critical stress of single slab pavement. Thus, the parameter to illustrate the relationship between the critical stress of multiple slabs pavement and the critical stress of single slab pavement should be considered in future work.

## REFERENCES

1. AASHTO. (1993). *AASHTO guide for design of pavement structures, 1993*. Washington, D.C.: The Association.
2. AASHTO. (2017). AASHTO LRFD Bridge Design Specifications (8 ed.).
3. American Concrete Institute. (2010). Report on High-Strength Concrete. (ACI-363R-10).
4. Armaghani, J. M., Larsen, T. J., & Smith, L. L. (1987). *Temperature Response of Concrete Pavements*. Paper presented at the 66th Annual Meeting of the Transportation Board, Washington D.C.
5. Bianchini, A. (2013). Evaluation of Temperature-Induced Curling in Concrete Slabs Using Deflection Difference Analysis. *Journal of Transportation Engineering-ASCE*, 139(2), 130-137. doi:10.1061/(ASCE)Te.1943-5436.0000490
6. Briggs, R. C., & Nazarian, S. (1989). Effects of Unknown Rigid Subgrade Layers on Backcalculation of Pavement Moduli and Projections of Pavement Performance. *Transportation Research Record: Journal of the Transportation Research Board*, 1227, 183-193.
7. Brill, D. R., & Kawa, I. (2017, August 27–30, 2017). *Advances in FAA Pavement Thickness Design Software: FAARFIELD 1.41*. Paper presented at the International Conference on Highway Pavements and Airfield Technology 2017, Philadelphia, PA.
8. Burningham, S., & Stankevich, N. (2005). Why road maintenance is important and how to get it done. *Transport notes series*, 4.



9. Byrum, C. R. (2011). Jointed Load Transfer in Concrete Airfield Pavements. (IRPF-01-G-002-05-2). Innovative Pavement Research Foundation. Rosemont, IL.
10. Chou, Y. J., & Lytton, R. L. (1991). Accuracy and Consistency of Backcalculated Pavement Layer Moduli. *Transportation Research Record: Journal of the Transportation Research Board*, 1293, 72-85.
11. Crovetto, J. (2006). Cost Effective Concrete Pavement Cross Sections-Final Report. Marquette University, The Wisconsin Department of Transportation.
12. Davids, W. G., Turkiyyah, G. M., & Mahoney, J. P. (1998). EverFE - Rigid pavement three-dimensional finite element analysis tool. *Design and Rehabilitation of Pavements*, 1629(1629), 41-49. doi:10.3141/1629-06
13. Douglas, S. C., Roesler, J. R., & White, J. D. (2009, August 2009). *Construction QA/QC Testing versus Selection of Design Values for PCC Pavement Foundation Layers*. Paper presented at the 2009 Mid-Continent Transportation Research Symposium, Ames, IA.
14. Ellis, T. B. (2008). *A Comparison of Nondestructive Testing Backcalculation Techniques for Rigid and Flexible Pavements*. (Undergraduate Undergraduate Honors Theses), University of Arkansas, Fayetteville, AR.
15. ERES Consultants, I. (1987). *Pavement Design Principles and Practices, A Training Course* (Vol. Module 3-4). Washington D.C.: National Highway Institute
16. Evangelista, F., & Roesler, J. (2009). *Top-Down Cracking Predictions for Airfield Rigid Pavements* (Vol. 2095).
17. Federal Aviation Administration (2009). *Airport Pavement Design and Evaluation* (DOT/FAA/AC-150/5320-6E).

18. Federal Aviation Administration (2011). *Use of Nondestructive Testing in the Evaluation of Airport Pavements* (AC 150/5370-11B).
19. Federal Aviation Administration (2016). *Airport Pavement Design and Evaluation* (DOT/FAA/AC-150/5320-6F).
20. Foxworthy, P. T., & Darter, M. I. (1986). Preliminary Concepts for FWD Testing and Evaluation of Rigid Airfield Pavements. *Transportation Research Record: Journal of the Transportation Research Board*, 1070, 77-88.
21. Fwa, T. F., & Setiadji, B. H. (2006). Evaluation of Backcalculation Methods for Nondestructive Determination of Concrete Pavement Properties. *Transportation Research Record: Journal of the Transportation Research Board*, 1949, 83-97.
22. Guo Edward, H. (2000). Effects of Slab Size on Airport Pavement Performance. (DOT/FAA/AR-99/83). U.S. Department of Transportation/Federal Aviation Administration.
23. Guo Edward, H. (2003). Proof and Comments on Extensively Used Assumption in PCC Pavement Analysis and Evaluation. *Journal of Transportation Engineering*, 129(2), 219-220. doi:10.1061/(ASCE)0733-947X(2003)129:2(219)
24. Guo Edward, H., & Marsey, W. (2012). *Verification Of Curling In PCC Slabs At FAA National Airport Pavement Test Facility*. Paper presented at the 27th International Air Transportation Conference, Chicago, IL.
25. Hall, K. T., Darter, M. I., & Kuo, C. M. (1995). Improved Methods for Selection of k Value for Concrete Pavement Design. *Transportation Research Record: Journal of the Transportation Research Board*, 1505, 128-136.

26. Hammons, M. I., Pittman, D. W., & Mathews, D. D. (1995). Effectiveness of Load Transfer Devices. (DOT/FAA/AR-95/80). U.S. Department of Transportation/Federal Aviation Administration.
27. Huang, Y. H. (1993). Pavement Analysis and Design: Prentice Hall.
28. Ioannides, A. M., Thompson, M. R., & Barenberg, E. J. (1985, April 23-25). *Finite Element Analysis of Slabs-On-Grade Using a Variety of Support Models*. Paper presented at the Third International Conference on Concrete Pavement Design and Rehabilitation, Purdue University, West Lafayette, IN.
29. Ioannides, A. M. (1990). Dimensional Analysis in NDT Rigid Pavement Evaluation. *Journal of Transportation Engineering*, 116. doi:10.1061/(ASCE)0733-947X(1990)116:1(23)
30. Kapiri, M., Tutumluer, E., & Barenberg, E. J. (2000, Jun 18-21). *Analysis of Temperature Effects on Pavement Response at Denver International Airport*. Paper presented at the 26th International Air Transportation Conference, San Francisco, CA.
31. Kaya, O., Ceylan, H., Gopalakrishnan, K., Kim, S., Rezaei-Tarahomi, A., & Brill, D. R. (In Press). *Evaluation of Rigid Airfield Pavement Cracking Failure Models*. Transportation Research Record: Journal of the Transportation Research Board, (19-03998).
32. Khazanovich, L., & Gotlif, A. (2003). Evaluation of Joint and Crack Load Transfer Final Report. (FHWA-RD-02-088). U.S Department of Transportation/Federal Highway Administration.

33. Khazanovich, L., McPeak, T. J., & Tayabji, S. (2000). LTPP rigid pavement FWD deflection analysis and backcalculation procedure. In *Nondestructive Testing of Pavements and Backcalculation of Moduli* (Vol. Third Volume, pp. 246-266). West Conshohocken, PA: American Society for Testing and Materials.
34. Kim, Y. R., & Park, H. (2002). Use of Falling Weight Deflectometer Multi-Load Data for Pavement Strength Estimation. (FHWA/NC/2002-006). North Carolina State University. Raleigh, NC.
35. Limouee, M. (2009). *Verification of NYSLAB A Software for the Analysis of Kointed Pavements*. (Master of Science), The University of Texas at El Paso, El Paso, TX.
36. Liu, S., Ling, J., Yang, W., Yuan, J., & Zhang, J. (2017, Jan 11-12). *Closed-Form Backcalculation of Rigid-Pavement Parameters Using Barycentric Horizontal Distance of Deflection Basin*. Paper presented at the Transportation Research Board 96th Annual Meeting, Washington DC, United States.
37. Maina, J. W., Yokota, H., & Matsui, K. (1998). Effect of Errors in Layer Thickness on Backcalculated Layer Moduli. *Japan Society of Civil Engineers (JSCE)*, 3.
38. Mikolaj, J., Remek, L., & Macula, M. (2017). Asphalt Concrete Overlay Optimization Based on Pavement Performance Models. *Advances in Materials Science and Engineering*, 1-10. doi:10.1155/2017/6063508
39. NAPTF. (2010). NAPTF F/HWD Round-Up. U.S. Department of Transportation/Federal Aviation Administration.
40. Rezaei-Tarahomi, A., Kaya, O., Ceylan, H., Gopalakrishnan, K., Kim, S., & Brill, D. R. (2017). Sensitivity quantification of airport concrete pavement stress responses

- associated with top-down and bottom-up cracking. *International Journal of Pavement Research and Technology*, 10(5), 410-420. doi:10.1016/j.ijprt.2017.07.001
41. Rollings, R. S. (1988). Design of Overlays for Rigid Airport Pavements. (DOT/FAA/PM-87/19). U.S. Department of Transportation/Federal Aviation Administration.
  42. Rufino, D., Roesler, J., & Barenberg, E. (2004). *Effect of Pavement Temperature on Concrete Pavement Joint Responses*. Paper presented at the 2004 FAA Worldwide Airport Technology Transfer Conference, Atlantic City, NJ.
  43. Sadeghi, V., & Hesami, S. (2018). Investigation of load transfer efficiency in jointed plain concrete pavements (JPCP) using FEM. *International Journal of Pavement Research and Technology*, 11(3), 245-252.  
doi:<https://doi.org/10.1016/j.ijprt.2017.10.001>
  44. Shoukry, S. N., William, G. W., & Martinelli, D. R. (1999, March). *Assessment of the performance of rigid pavement back-calculation through finite element modeling*. Paper presented at the SPIE Conference on Nondestructive Evaluation of Bridges and Highways III, Newport Beach, CA.
  45. Smith, K. D., Peshkin, D. G., Darter, M. I., & Mueller, A. L. (1990).  
PERFORMANCE OF JOINTED CONCRETE PAVEMENTS. VOLUME III -  
SUMMARY OF RESEARCH FINDINGS. FINAL REPORT. (FHWA-RD-89-138).  
U.S. Department of Transportation/Federal Highway Administration.
  46. Stubstad, R. N., Jiang, Y. J., & Lukanen, E. O. (2006). Guideline for Review and Evaluation of Backcalculation Results. (FHWA-RD-05-152). U.S. Department of Transportation/Federal Highway Administration.

47. Tabatabaie, A. M., & Barenberg, E. J. (1978). Finite-Element Analysis of Jointed or Cracked Concrete Pavements. *Transportation Research Record: Journal of the Transportation Research Board*, 671, 11-19.
48. Thottempudi, A. K. (2010). *Backcalculation of Layer Moduli of Granular Layers for Both Rigid and Flexible Pavements*. (Master of Science), Michigan State University, East Lansing, MI.
49. Wadkar, A. (2010). *Study of Load Transfer Efficiency of Airfield Rigid Pavement Joints Based on Stresses and Deflection*. (Master of Science in Engineering Degree), Rowan University, Glassboro, NJ.
50. Westergaard, H. M. (1926). Stresses in Concrete Pavements Computed by Theoretical Analysis. *Public Roads*, 7.
51. Zhao, H., Ma, L., & Zhang, J. (2018). Effects of temperature variations on the deflections of airfield jointed plain concrete pavements. *International Journal of Transportation Science and Technology*, 7(3), 179-188.  
doi:10.1016/j.ijtst.2018.06.003